DESIGN AND DEVELOPMENT OF AN EFFICIENT METAHEURISTIC BASED DESMOGGING TECHNIQUE FOR COLOR IMAGES

A Thesis

Submitted in partial fulfillment of the requirements for the award of the degree of

DOCTOR OF PHILOSOPHY

in

COMPUTER SCIENCE ENGINEERING

By

Jeevan Bala

(41600151)

Supervised By

Dr. Kamlesh Lakhwani

Transforming Education Transforming India

LOVELY PROFESSIONAL UNIVERSITY

PUNJAB

2020

Certificate

I, Jeevan Bala, Regn. No. 41600151, hereby declare that the thesis entitled "**Design and Development of an Efficient Metaheuristic based Desmogging Technique for Color Images** " submitted to the Computer Science and Engineering Department at Lovely Professional University, Phagwara, Punjab, India is an authenticated record of my own work for the award of the degree of "Doctor of Philosophy" under the supervision of Dr. Kamlesh Lakhwani. This report has not been submitted to any other institution for award of any other degree.

Jeevan Bala
Regn. No. 41600151

Place: Phagwara
Date: 04.12.2020

This is to certify that the above statement made by the candidate is correct to the best of my knowledge.

Verified by:

Dr. Kamlesh Lakhwani
Associate Professor
Computer Science and Engineering Department
Lovely Professional University,
Phagwara, Punjab, India.

Abstract

Smog is defined as an intense air pollution. It is a combination of smoke and fog and it degrades the visibility of outdoor image to a great extent. Therefore, existing imaging systems are unable to obtain the potential information from these weather degraded images. Many visibility restoration models have been designed to restore smog from still images. But, removing the smog from images is defined as an ill-posed problem.

The quality of the restored image depends upon the accurate estimation of the transmission map. However, the transmission map obtained using various desmogging models is not accurate in the case of images with large smog gradient, and fail while image desmogging. As a result, the restored images suffer from numerous issues such as halo and gradient reversal artifacts, edge and texture distortion, color distortion, etc.

To overcome these issues, various desmogging models are proposed in this research work. Initially, a novel illumination channel prior (NICP) is proposed to restore smoggy images in a significant way. A gradient magnitude based filter is also utilized to refine the transmission map. Finally, the smog-free images are obtained by using the computed depth information of smoggy images and the smog restoration model.

The subjective and quantitative analysis are drawn to evaluate the performance of the proposed NICP based desmogging approach. It is found that the proposed NICP based desmogging approach outperforms competitive models in terms of some well-known performance metrics. These metrics are as: perceptual smog gradient, contrast gain, percentage of saturated pixels, new visible edges, edge gradients, execution time, peak signal to noise ratio, and structural similarity index metric.

Although NICP outperforms the existing desmogging approaches in the case of smoggy images, but, for images with complex background and having large smog gradient, it may not be so effective. Therefore, a novel gradient channel prior (NGCP) and information gain based filter desmogging approach are designed. Initially, the gradient channel prior is used to estimate the optical information of smoggy images. Thereafter, an information gain based filter is designed to improve the transmission map. The smog-free

image is then computed using an improved restoration model. Finally, the performance of the proposed NGCP based desmogging model is compared with seven competitive desmogging models on some well-known benchmark and real-life desmogging images. From comparative analyses, it is found that the proposed model outperforms the competitive models in terms of various performance metrics.

Although, NICP and NGCP provide promising desmogging results as compared to the competitive desmogging models. However, it suffers from sky-regions and color distortion, especially in the case of images affected by large smog gradients. Also, the effect of the hyper-parameters tuning issue is ignored. Therefore, weighted integrated transmission maps and integrated variational regularized model with hybrid constraints (WIVC) based desmogging model is proposed. The transmission map estimation is obtained from the weighted integrated transmission maps by considering foreground and sky regions. The computed transmission map is further refined using an integrated variational regularized model with hybrid constraints.

However, the proposed WIVC approach suffers from the hyper-parameters tuning issue. Therefore, in this chapter, a Non-dominated sorting genetic algorithm (NSGA) is also used to tune the hyper-parameters of the proposed WIVC approach. Extensive comparative results reveal that the WIVC performs effectively across a wide range of smog degradation levels without causing any visible artifacts. It is found that the proposed model outperforms seven competitive desmogging models in terms of various performance metrics on benchmark and real-life smoggy images. The main benefits of WIVC over the competitive desmogging models are: WIVC can efficiently overcome the sky region issue. Also, WIVC can preserve texture details of the restored smoggy images more efficiently.

Thorough extensive comparative analyses, it is found that the proposed models i.e., NICP, NGCP, and WIVC can significantly suppress visual artifacts for smoggy images and obtain significantly better restored images as compared to the existing desmogging models both quantitatively and qualitatively. Moreover, the proposed models take significantly lesser time, therefore, the proposed models will facilitate various real-life imaging systems.

Acknowledgments

All the years spent researching and pursuing the Ph.D. degree feels like an entire journey in itself. A journey that has taught how to face and cross some of the hardest barriers possible. This was no less than an adventure. I'm grateful for all the amazing opportunities I have had to learn from some of the smartest colleagues and mentors. I cannot express my gratitude enough for the knowledge I have gained over the past years while working on this. I'll always put this experience and wisdom into good practices to help other students to learn just like I was helped by my mentors. With a profound sense of gratitude and heartiest regard,

I express my sincere feelings of indebtedness to my supervisor Dr. Kamlesh Lakhwani, Assistant Professor, Computer Science and Engineering Department, Lovely Professional University, Phagwara, Punjab, India for his valuable guidance, motivation, encouragement, moral support, and invaluable cooperation. The generous and encouraging attitude with which he resolved all my problems will always have a shadow on my character. It has been a great pleasure and experience to work under his guidance.

I am grateful to the Head of Department, who made my study a knowledgeable experience during my stay in the department. I am thankful to my doctoral committee members for their beneficial suggestions and ensuring the accurate pace of the progress of my thesis. I sincerely thank the faculty and support staff of the Computer Science and Engineering department for their constant motivation.

I would like to shower hearty gratitude, feeling of indebtedness and endless love to my parents for their unconditional love, moral support and sacrifices which helped me to achieve this target. I pay regard to one and everyone who knowingly or unknowingly supported me during this journey of knowledge.

Jeevan Bala

Contents

List of Figures

List of Tables

List of important abbreviations

Acronym	Meaning
ACO	Ant colony optimization
BA	Blocking artifacts
BCP	Bright channel prior
BHE	Bi-histogram equalization
CAP	Color attenuation prior
Cg	Contrast gain per pixel
CL	Color-lines
COD	Change of detail prior
DCP	Dark channel prior
DE	Depth estimation
ECBD	Effective contrast based restoration
EP	Edge preservation
ET	Execution time
FADE	Fog aware density evaluator
FHRT	Fast smog removal model
FPDE.T.F	Fourth-order partial differential equations based trilateral filter
FRIDA	Foggy road image database
FRIDA2	Foggy road image database 2
GA	Genetic algorithm
GF	Guided filter
GITF	Gain intervention based trilateral filter
GPP	Gradient profile prior
GRA	Gradient reversal artifacts
Gt	Ground truth images
HA	Halo artifacts
HST.S	Hybrid subjective testing set
I	Weather degraded image
I_r	Restored/clear image
ITS	Indoor training set
IVRM	Integrated desmogging model

KD .... Known depth
L1 .... L_1 norm regularization based restoration model
LHG........ Large smog gradient
LTQ .... Linear transform and quadtree
WHD.R........ Weighted the least square and high dynamic range
MDF........ Multi-scale depth fusion
MI .... Multiple images
MRM .... Modified restoration model
MS .... Multiple scattering
MSE........ Mean squared error
OGP.P........ Oblique gradient profile prior
OTS........ Outdoor training set
Pdf .... Perceptual smog density
PF .... Polarizing filter
PSNR .... Peak signal to noise ratio
PSO........ Particle swarm optimization
RESIDE .... Realistic single image restoration
RSD........ Remote sensing desmogging
RSWHE .... Recursively separated weighted histogram equalization
RTTS........ Real- world task-driven testing set
SI .... Single image
SOTS........ Synthetic objective testing set
S_p .... Speed
SSIM........ Structural similarity index metric
WGIF........ Weighted guided image filter
WHDR .... Weighted least square and high dynamic range

Chapter 1

Introduction

1.1 Smoggy images

The recent advances in computer vision applications have led the attention of researchers toward desmogging models [13]. The visibility of captured images is degraded incredibly because of the occurrence of components like smog, haze, mist, *etc.* The phenomenon concerning fog, haze, or smog happens with the worsening environment. The observed luminous intensity of the scene is immersed and scattered due to the substantial presence of aerosols and particles dangling in the ambient air [5]. The objects captured in such an environment have poor visibility, thus having poor intensity and low contrast [14]. The performance of several computer vision applications is highly degraded due to bad environmental conditions. The computer vision applications like surveillance systems, intelligent transportation systems, object tracking systems, *etc.* fail due to the low visibility of the images. Several desmogging models have been developed to solve this issue. These models play an important part in computer vision applications used in poor weather conditions. Due to this, the researchers are attracted to the desmogging models. For instance, visibility restoration models are extensively used for target detection in civil and military area [15], remote sensing [16], traffic surveillance [17], *etc.* Therefore, the evolution of desmogging models is considered a research of great significance and interest.

Figure 1.1 (a) shows natural image captured in clear day. The fog affected image is shown in Figure 1.1 (b). The haze affected image is represented in Figure 1.1 (c). It clearly shows that hazy image has poorer visibility than clear day and foggy images. The smoggy image is represented in Figure 1.1 (d). It is shown that the smoggy image is more affected by weather degradation as compared to the foggy and hazy image.

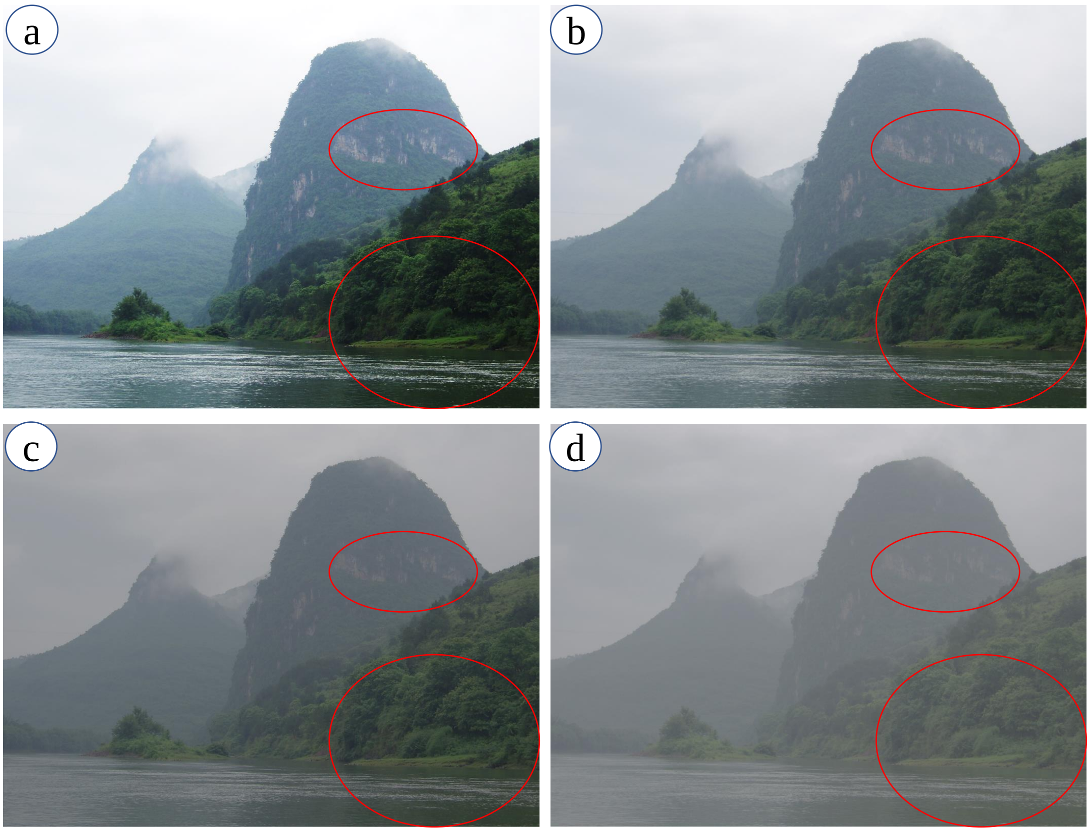

Figure 1.1: Weather degraded images (a) Natural, (b) Foggy, (c) Hazy, and (d) Smoggy image

The restoration of the weather degraded image requires information about the physical features of the particular scene. The depth of the scene is one of such features [18]. With the known depth value, the process of desmogging becomes more straightforward [19]. The depth map, however, is priorly unknown in the case of applications deployed in the real-world [20].

Therefore, the major problem of desmogging models is the precise depth map evaluation. The problem of estimation of the depth map demands prior knowledge about weather degraded images like atmospheric scattering or depth cues [21]. The theory of depth map evaluation seems new, but this has been largely utilized by artists while expressing scene depth in their portraits since the early renaissance [22, 23, 24].

Visibility restoration is a difficult task due to the reason that the transmission depends upon the unknown depth that changes with changing atmospheric situations [25]. Tan *et al.* [24] and Kawakami *et al.* [26] utilized local contrast values to restore weather degraded images. The proposed models proved to be successful in image sections having notable weather degradation. Nevertheless, the reconstructed images are frequently found to be possessing over saturation problem. [27]. maximizing contrast thus causes over-saturation. This over-saturation problem can be overcome by using physics-based restoration models [28, 29]. He *et al.* [27] proposed a simplistic and efficient desmogging model using DCP. Nevertheless, it too experiences problems like halo artifacts and color distortion [30].

Visibility restoration models have recently made significant advances because of the consideration of effective priors and suppositions. Wang *et al.* [31] proposed a patch-based DCP model to solve the issue. However, the model is ineffective when the objects in the image are intrinsically similar to the airlight and negligible shadow is cast. The existing literature includes the definitions of DCP. However, the model may produce the annoying gradient reversal and halo artifacts [32]. Handling such issues involved the development of several image filters utilizing a guided filter for the refinement of the transmission map. These models require higher computational time [33]. To handle the discussed issues, the researchers propose a filter by the use of gain intervention [5]. However, it experiences color distortion problems and gradient reversal artifact.

1.2 Desmogging

Digital images captured in poor weather mostly lose illumination and fidelity, resulting from the idea that illuminates is intercepted and disseminated by a dirty medium like droplets of water in the atmospheric veil or other particles throughout the method of transmission [1]. Also, the majority of automatic mechanism, that originally centered on the input objects in the scene becomes unsuccessful to run because of the degradation of images [3]. Therefore, the desmogging techniques play a vital role in various image processing applications like object tracking, intelligent transportation system, airplane landing-takeoff, etc. [4].

The illuminate perceived from a scene on a smoggy day is spattered and absorbed due to the appearance of molecules and aerosols present in the atmosphere [5]. The worsening of environment eminence causes the regular occurrence of smog [34]. The intense smog leads to the poor visibility of digital images, this reduces the performance of several computer vision-based applications [35, 27]. Therefore, in a smoggy environment, the perceptibility of the objects reduce [14] and such images are oftentimes identified as degraded images [36].

1.3 Imaging under smoggy environment

Figure 1.2 shows the imaging model under smoggy and smog-free environment. It has been observed that the imaging under smog free environment has good visibility when it is going to be digitized (Figure 1.2 (a)). However, in case of smoggy environment, smog effects the digitizing process of image. Therefore, captured image is infected from the smog (as in Figure 1.2 (b)) [1].

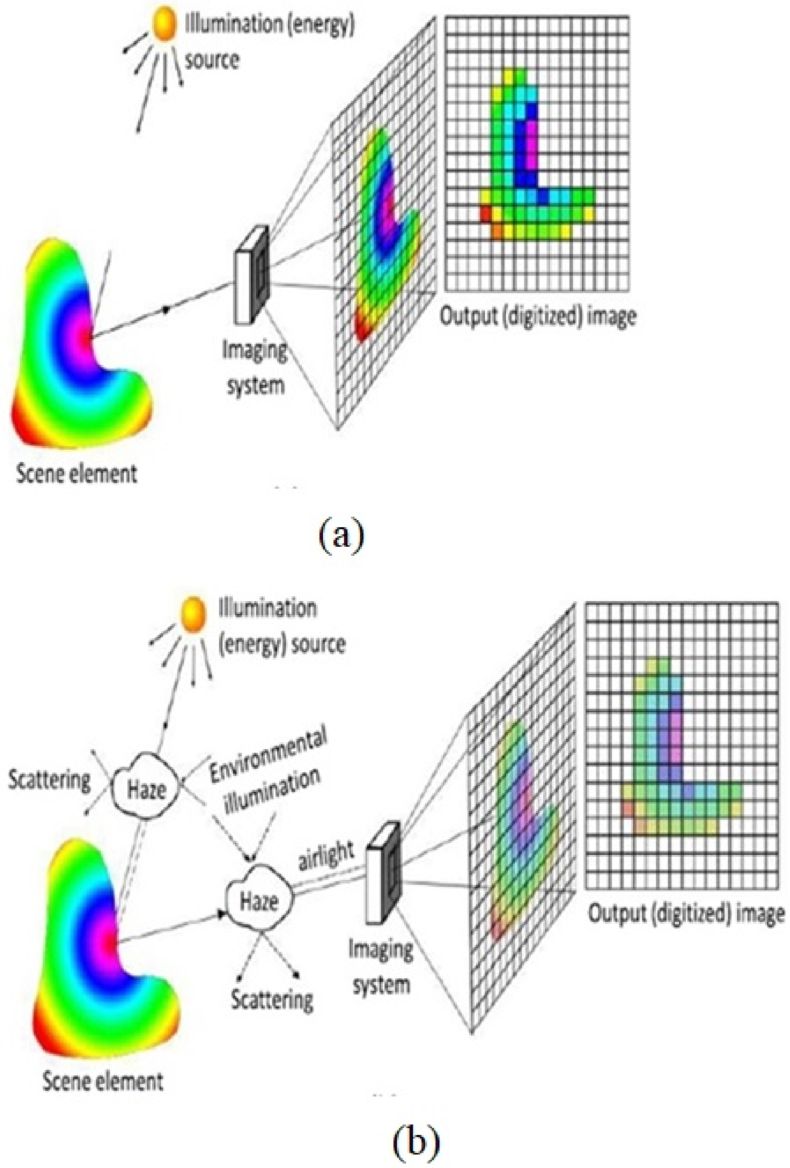

Figure 1.2: Imaging under (a) In sunny weather, (b) In smoggy environment [1].

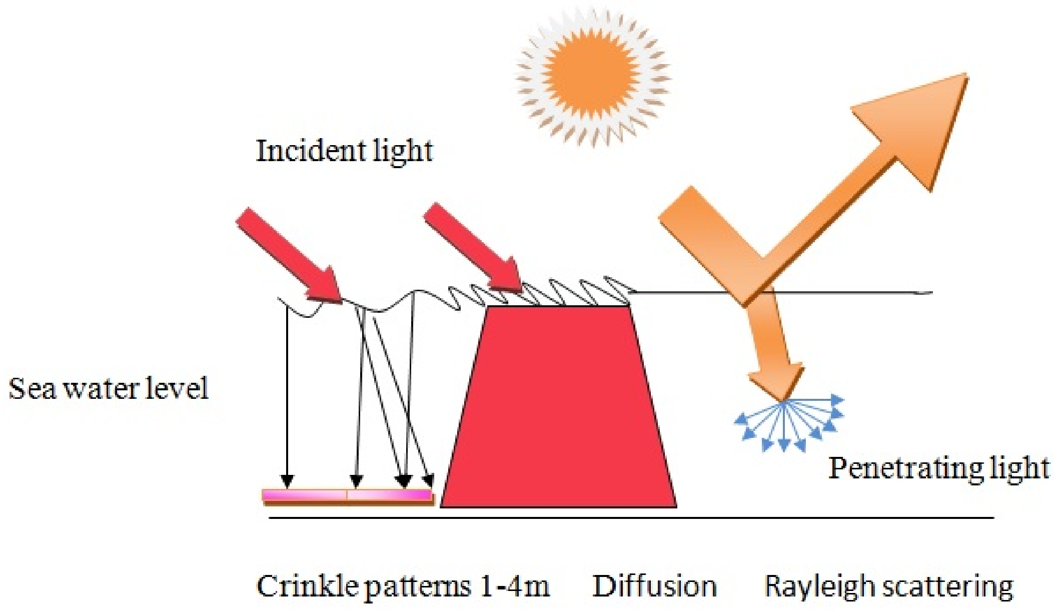

Figure 1.3: Effect of haze/smog on underwater imaging

Figure 1.3 illustrates the impact of light on underwater images. It can be observed that the influence of haze/smog on underwater images turnout to be more as the depth of the scene becomes deeper [37].

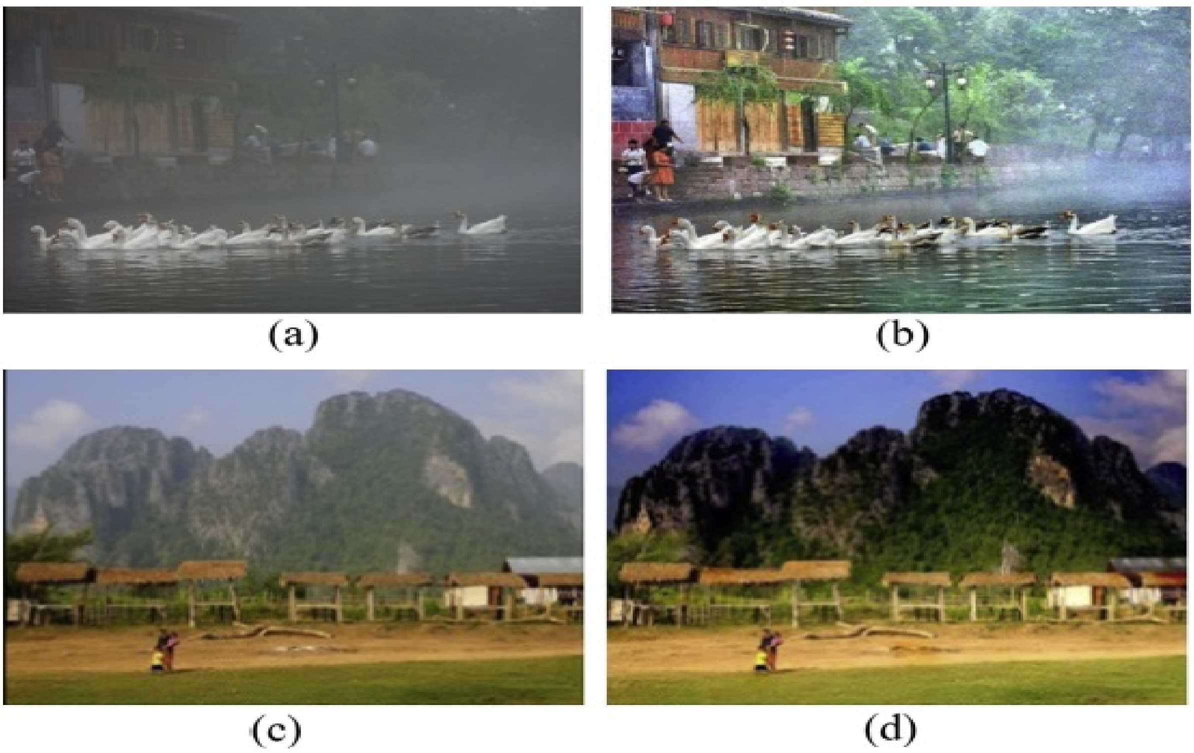

Figure 1.4: Smoggy images and smog-free images [2]

Figure 1.4 depicts the effect of smog on given objects and the effect of desmogging techniques. It clearly shows that the smoggy images have poor visibility and the smog free images have considerably improved visibility [38].

1.4 Smog removal techniques

Following are various desmogging techniques which can be used to remove smog from images.

1.4.1 Smog imaging model

Fattal et al. [28, 39] proposed the smog formation model. The mathematical representation of a smoggy image is illustrated below:

$$S_{mg}(j) = O_{mg}(j)T_{mp}(j) + \mathscr{G}_{\infty}(1 - T_{mp}(j)) \tag{1.1}$$

Here, $S_{mg}(j)$ and $O_{mg}(j)$ represents a smoggy and an actual image respectively. The transmission map is represented as $T_{mp}(j) \in [0,1]$, $\mathscr{G}_{\infty}$ denotes global atmospheric veil and j represents the pixel coordinate. The main focus of the desmogging approach is the estimation of $O_{mg}(j)$, $T_{mp}(j)$, and $\mathscr{G}_{\infty}$ from $S_{mg}(j)$. The $O_{mg}(j)T_{mp}(j)$ demonstrate direct attenuation, which depends upon the transmission media [40].

The $\mathscr{G}_{\infty}(1 - T_{mp}(j))$ indicates airlight map. The direct attenuation illustrates the actual scene radiance, and the decrease with respect to $T_{mp}(j)$. The decrease in $T_{mp}(j)$ leads to increase in the airlight map. The prime cause behind the reducing airlight map is the depletion of actual image radiance (O_{mg}) by smog and far-away objects. The $T_{mp}(j)$ for homogeneous smoggy conditions can be computed as follows:

$$T_{mp}(j) = e^{-\gamma d(j)} \tag{1.2}$$

Here, $d(j)$ denotes the depth of the image O_{mg}, and γ is the extinction factor of the medium.

He et al. [27] demonstrated the existance of a relation among atmospheric veil ($A_{vl}(j)$) and transmission map ($T_{mp}(j)$). This relation is as represented as follows:

$$A_{vl}(j) = 1 - T_{mp}(j) \tag{1.3}$$

After the estimation of the atmospheric veil, the restoration model for smog removal can be applied. Therefore, the actual image can be derived using Eq. 1.1. The coarse estimated atmospheric veil ($A_{vl}(j)$) is calculated by using the minimum element of object $\frac{S_{mg}(j)}{\mathscr{G}_\infty}$, the dissimilarity between image $\frac{S_{mg}(j)}{\mathscr{G}_\infty}$ and coarse estimated atmospheric veil $A_{vl}(j)$ approaches 0 with maximum probability. Thus, to restrict this variation, a consistent parameter c is involved.

It can be observed from Eq. 1.3 that the actual transmission can be small or close to zero in its minimal value. However, some noise may be involved in the restored image. Hence, it becomes necessary to restrain the transmission map by utilizing a lower bound (x_0). The values of x_0 and c are defined to 0.1 and 0.95, respectively as recorded in the literature [41].

The scene radiance ($O_{mg}(j)$) can be computed as below:

$$O_{mg}(j) = c \times \mathscr{G}_\infty + \frac{S_{mg}(j) - c \times \mathscr{G}_\infty}{max(T_{mp}(j), x_0)} \tag{1.4}$$

1.4.2 Dark channel prior

Dark channel prior states that among majority of non-sky masks, at least one color (R, G or B) has several pixels which have very small or almost near to zero value. In similar masks, the intensity values are almost zero [42]. Small pixel value in dark channel is because of three factors: shadows, color full scenes and dark scenes.

Dark channel is quite dark in most of smog free digital images. Therefore it has the ability to develop depth of input image. After evaluating depth of a smoggy image, one can easily restore the smog free image [43]. Figure 1.5 shows various steps involved in dark channel prior based smog removal method [27].

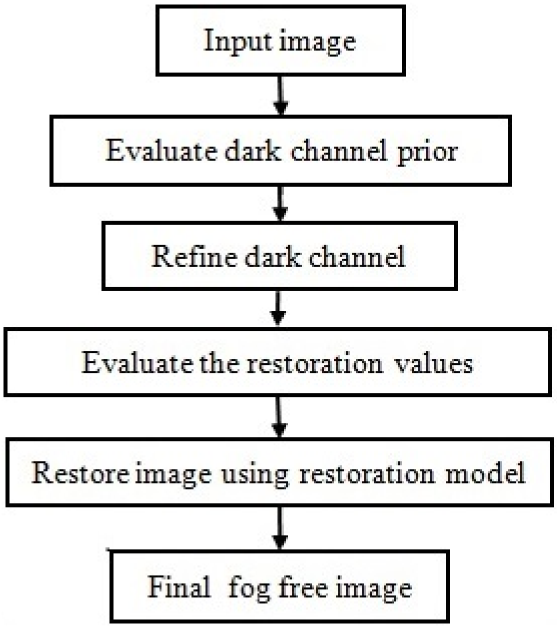

Figure 1.5: Smog removal using dark channel prior

1.4.3 Color attenuation prior

Smog removal has found to be a difficult issue in image processing, because of its ill-posed nature. The color attenuation prior is straightforward but a dominant technique to remove smog from a still image. By developing a linear approach for modeling the smoggy image's depth and learning parameters by utilizing supervised learning, the smoggy image's depth can be easily recovered [44]. By utilizing this depth map, the computation of the transmission map can easily be done and the smoggy image can be restored via atmospheric scattering model. Therefore it can effectively eliminate smog from the given scene. Figure 1.6 shows various steps required to implement smog removal from image using color attenuation prior [1].

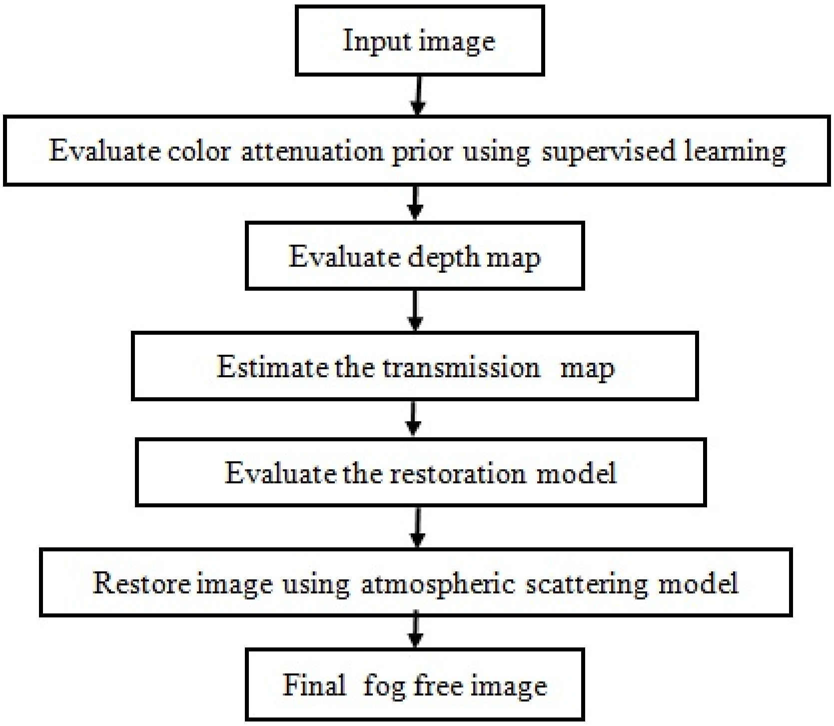

Figure 1.6: Working of color attenuation prior

1.4.4 Bi-histogram modification

Bi-Histogram Modification based technique has the ability to handle this problem. It has merged a smog density estimation with smog formation removal for optimistically estimating the smog density during transmission map estimation [45]. The Bi-Histogram Modification technique has found to be a best algorithm while working on restoring foreground and background smoggy scenarios [3].

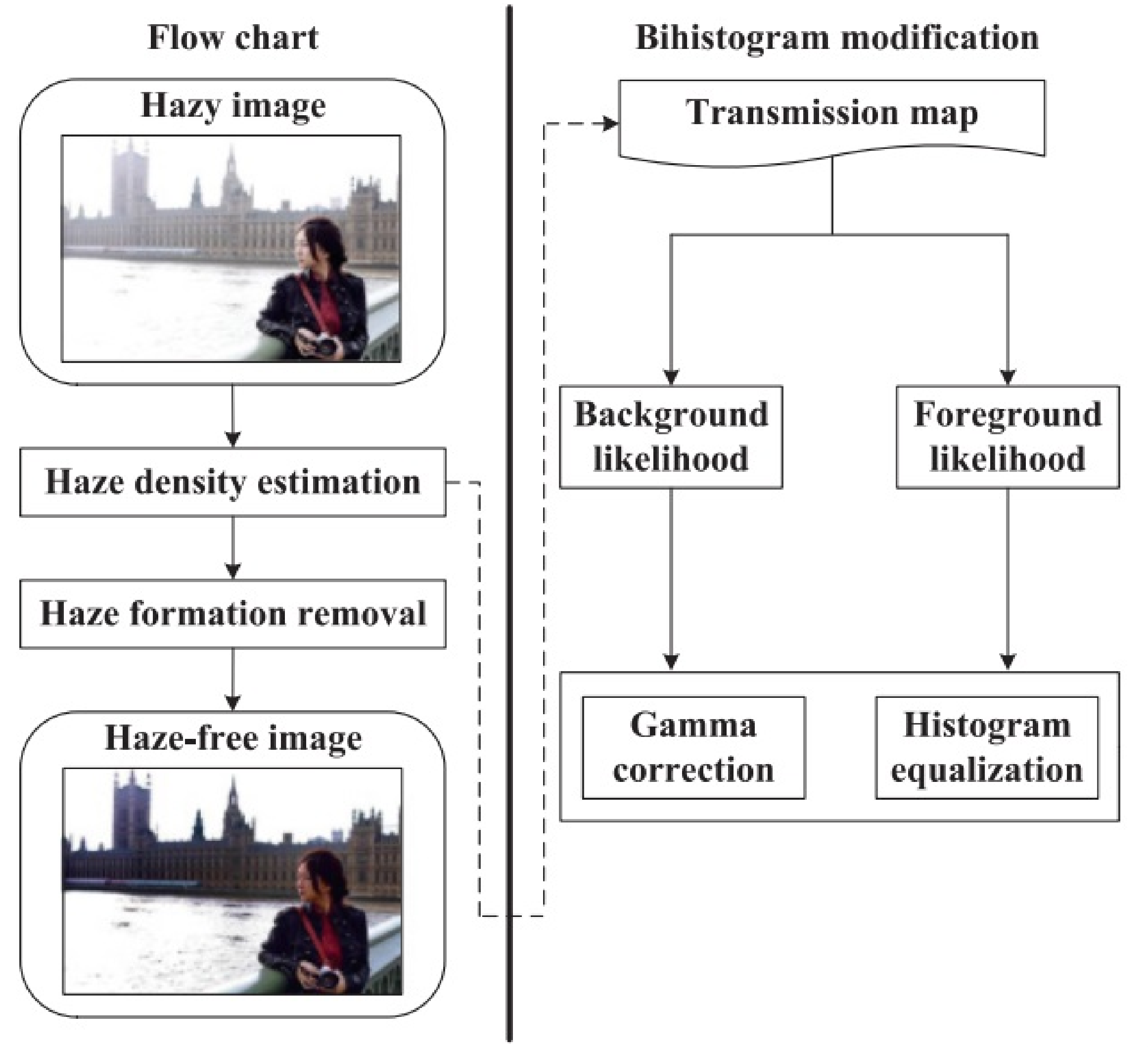

Figure 1.7: Smog removal using bi-histogram modification [3]

Figure 1.7 shows the smog removal working of Bi-Histogram Modification. Estimating the depth of a smoggy scene is critical task. But most of existing smog removal techniques often suffer from certain artifacts or the loss of potential information in their smog free output image because of uneven depth of the scene [46].

1.4.5 Local atmospheric light veil estimation

Figure 1.8 clearly demonstrate the working of Local atmospheric light veil estimation based smog removal technique. It utilizes a systematic technique by using a physical model in which the peak intensity value of each color pixel is considered while evaluating the initial atmospheric veil. Bilateral filter is then utilized to smooth each veil for attaining both edge preservation as well as local smoothness [47]. The reflection component of each color and transmission map are developed by utilizing physical atmospheric scattering model.

The Local atmospheric light veil estimation method avoids adverse effects because of error in developing the global atmospheric map. The local atmospheric light veil estimation has shown better results especially for outdoor smoggy images along with good color fidelity [4].

1.4.6 Two-dimensional canonical correlation analysis

In 2D canonical correlation analysis, image desmogging is modeled as a supervised learning based technique. It is based upon the assumption that in a natural image, masks are smooth and the pixel values in similar masks are estimated to be invariable. The use of linear correlation among smoggy image masks and corresponding transmission masks can evaluate the depth of the input image in more proficient manner [5].

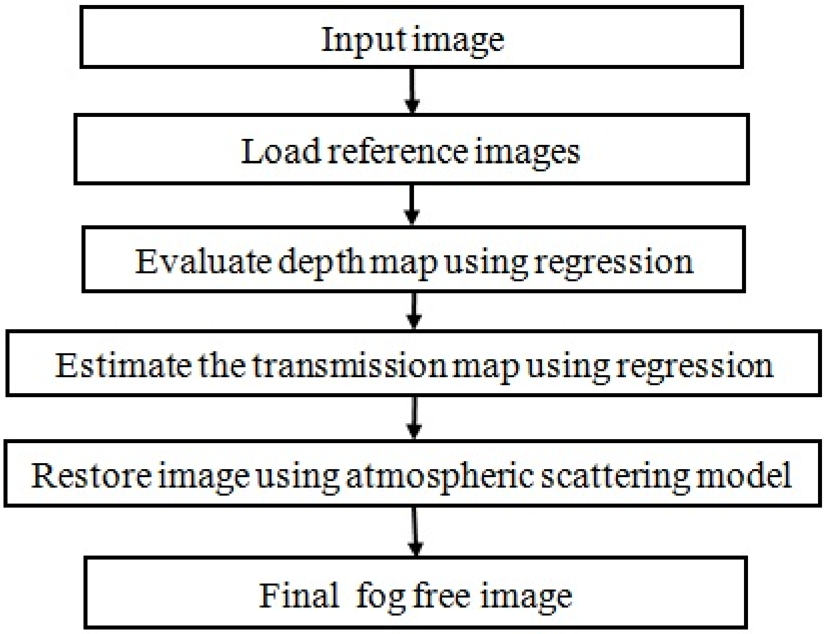

Figure 1.9: Restoration model using regression method

By increasing the correlation among masks, pairs of smoggy image and its transmission map, regression technique has the ability to learn a subspace to evaluate the reliable transmission map. Therefore, given a smoggy image, the transmission map is aggregated using linear regression of masks in the subspace and refine transmission map using given filter. The output smog free image is evaluated by utilizing the dichromatic atmospheric model. Figure 1.9 is showing various steps required to restore the smoggy image using regression model with two dimensional correlation analysis [48].

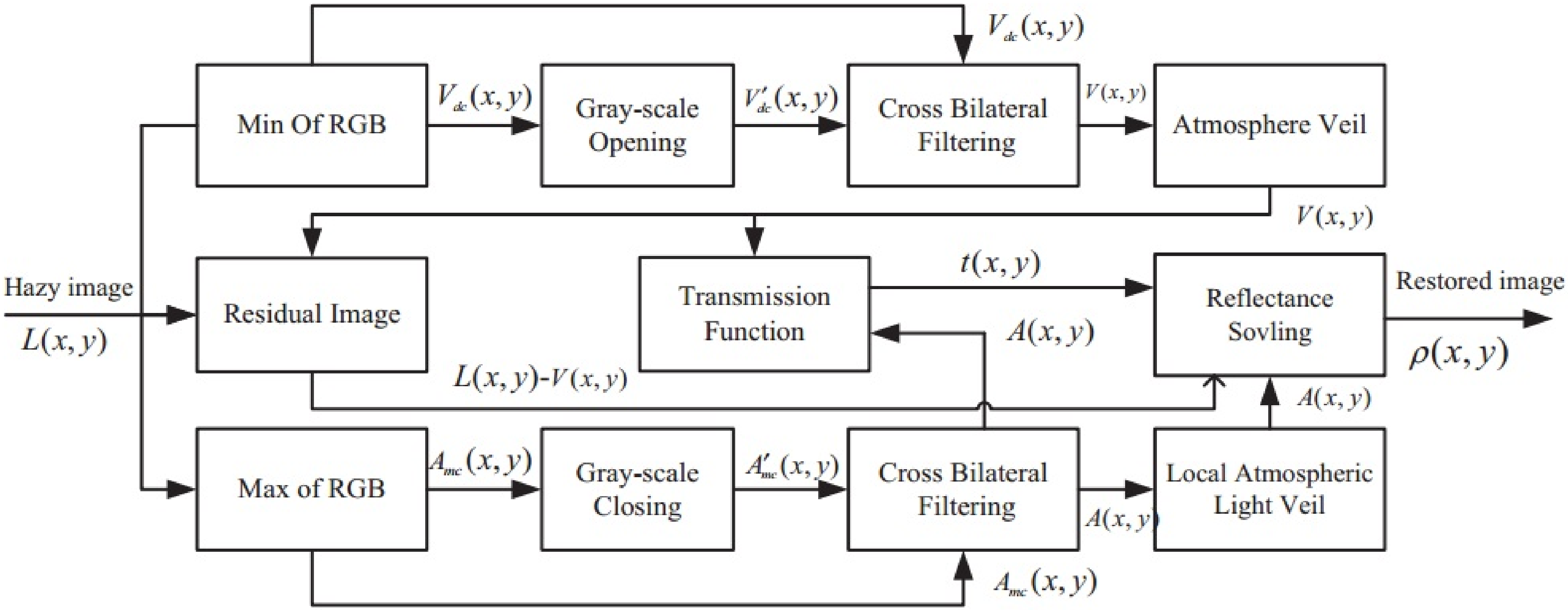

Figure 1.8: Block diagram of local atmospheric light veil estimation [4]

1.4.7 High-speed gain intervention refinement filter

Among the standard smog removal techniques, the dark channel prior is a proficient method in the existing literature. But many reviewers have shown that it results in smog-free image with halo effects. In order to handle this issue, numerous previous image filters are merged with dark channel prior to remove smog from images. But the use of filtering techniques certainly brings massive computational load while the smog-free outcome of integrated filtering and dark channel prior still has an area for enhancement [49].

To handle this issue a time-efficient refinement technique based upon the gain involvement is introduced and merged with dark channel prior to handle above-mentioned issues. The proposed filtering method is merged with dark channel prior to yield not only superior computation time but also for better improvement in smog-free image than standard filtering methods [5]. In Figure 1.10, the working of High-speed gain intervention refinement based smog elimination technique is given.

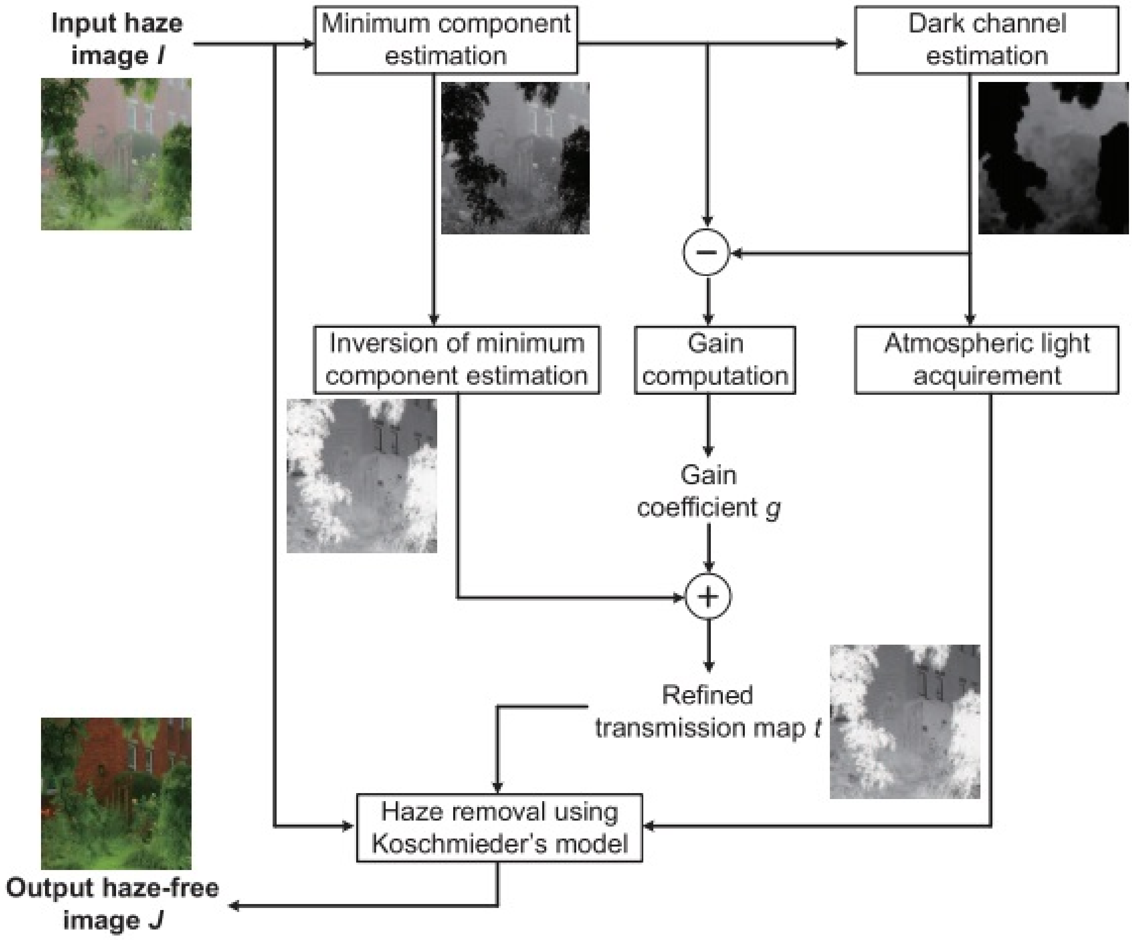

Figure 1.10: High-speed gain intervention refinement filter [5]

1.5 Meta-heuristic techniques

Meta-heuristic techniques have proven to be efficient tools providing solutions to several fields of engineering. Several image processing applications also attract the attention of researchers towards the use of solutions based on Meta-heuristics. These techniques are beneficial in both cases where traditional solutions are either present or are not efficient in solving the problems effectively [50]. Figure 1.11 shows a stepwise illustration of the genetic algorithm.

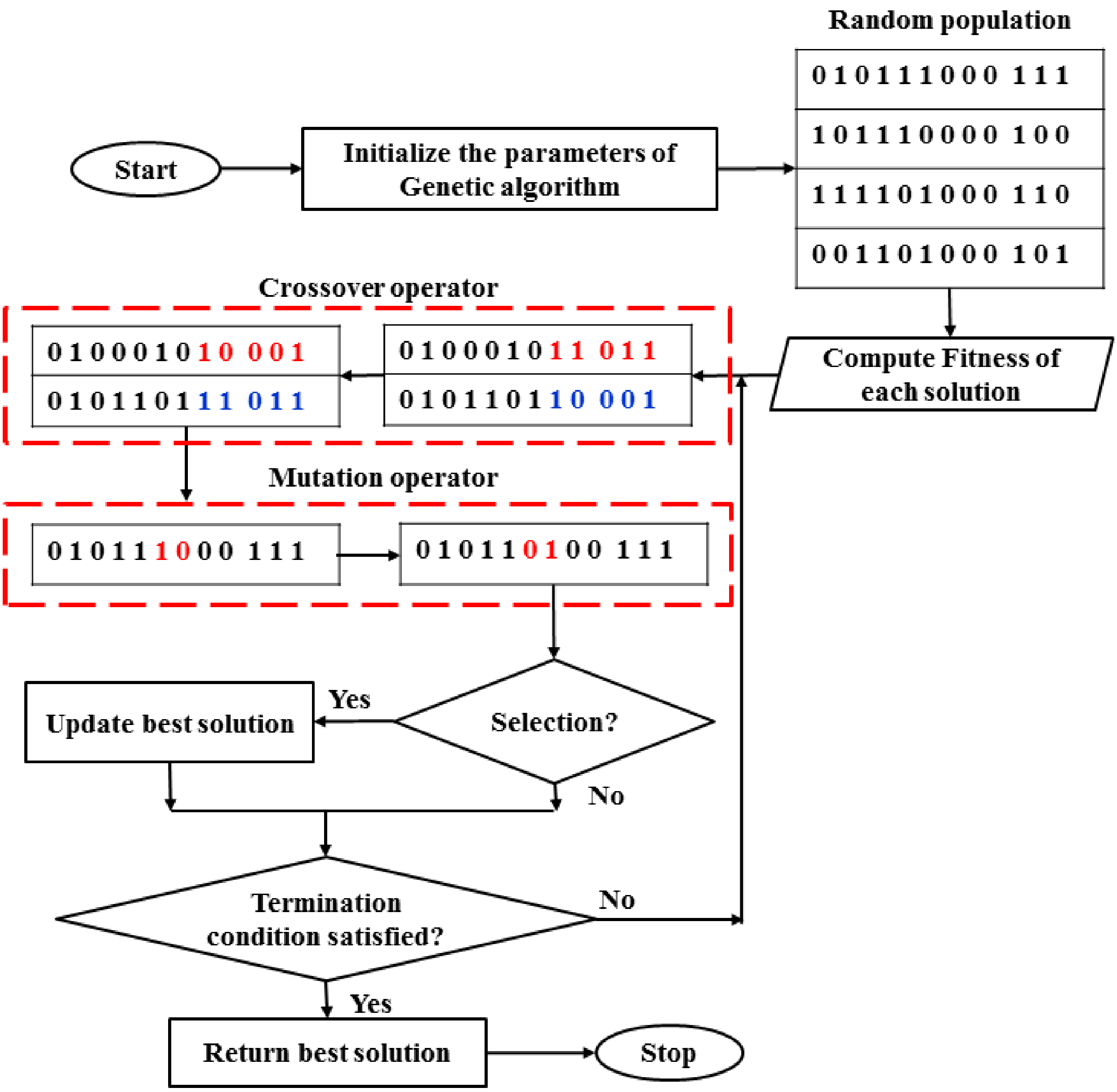

Figure 1.11: A flow of GA process

Whilst the earlier versions of the solutions involving the use of Genetic algorithm, Simulated annealing, Differential evolution, and Particle swarm optimization are developed in the immediate decade, the advancement of evolutionary computation algorithms such as Biogeography Based Optimization, Bacterial foraging optimization, Artificial bee colony, Harmony search, etc. has attracted the researchers from the entire world [51].

The GA represents every possible solution as a chromosome. Initially, a random generator generates a random population. This population is used in the starting point [52]. The suitability of the chromosomes in the initial population is assured using a function called a fitness function [53]. The next population is created by the application of mutation and crossover functions to the selective chromosomes and their offsprings. The repetition of this task is done till the generation of enough offspring [54].

The fitness value linked to the strings provides an efficient estimation of the solution. The random selection of pairs is done by the use of a crossover operator and new pairs are generated. The crossover rate is the measure of the number of crossover operations made [55]. The mutation operator randomly mutates the bits in the string. The count of mutation operations performed represents the mutation rate. Each level in the procedure provides a set of a new generation as the output [56].

1.6 Research motivation

With the worsening air pollution, smog has gradually become a problem in different parts of the world. The attenuation of scene radiance occurs due to the occurrence of the high concentration of aerosols in the ambient atmosphere. The scattered illumination hampers the visibility when added to the actual illumination. Therefore, the smoggy environment attenuates the visibility in the images captured undesirable adding of reflection and scattering effect [57].

Therefore the smoggy environment influences the working of several machine vision applications like remote sensing imaging, intelligent transportation systems, aerial imaging, etc. It has been found through the review of the literature that most of the existing research on image restoration only focus on defogging or dehazing of the images. Therefore, designing an efficient smog removal technique is the major motivation behind this research work.

1.7 Applications of desmogging models

Visibility restoration models play a significant role in several computer vision applications. Figure 1.12 shows the remarkable applications those utilizing desmogging models as pre-processing tools [58].

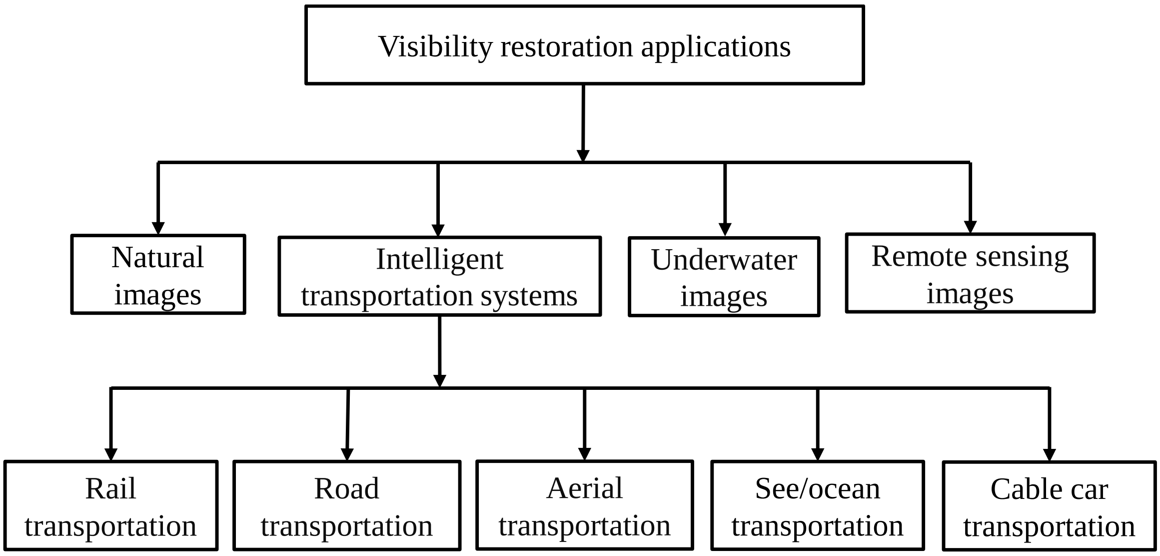

Figure 1.12: Applications of desmogging models

1.7.1 Remote sensing

Remote sensing images have wide applications in diversified areas varying from mineral exploration to agricultural applications [59]. However, the reduced quality of hyperspectral images harms the functioning of these applications [60]. Visibility restoration models have the capability of extracting high quality images from the remote sensing images [61].

1.7.2 Underwater images

It is a tedious task to attain more of the information from the images clicked underwater [62]. The researchers and divers capture the underwater images facing color sprinkles and color cast problems. Color cast occurs because the light attenuates in dissimilar wavelengths, that renders the environments underwater bluish. Thus, distorting the color of images [63]. Therefore, the implementation of restoration models become necessary to eliminate the influence of color cast and color dissemination from the underwater images [64].

1.7.3 Intelligent transport systems

Weather degradation reduces the extent of effective optical surveillance. This phenomenon of degradation is spatially varying and thus making it non-trivial [65]. Visibility restoration is a necessary model in several areas like lane detection, intelligent transportation systems, vehicle detection, *etc.* [66]. The subsequent subsections describe the most widespread employments of desmogging models while designing an intelligent transportation system.

A. Road transportation

Due to reduced vision caused by weather degradation, many accidents occur on roads, chiefly in hilly areas. Therefore, to limit accidents on highways and rugged areas, a desmogging model is expected to present a restored image to the driver on some visual device. Nevertheless, a desmogging model with constant time complexity is required because of the high speed of vehicles [67].

B. Aerial transportation

The weather degradation generally affects the takeoff and landing of airplanes. The poor environment conditions cause delayed or canceled flights. Such issues can be handled by deploying desmogging models to restore the actual scene from the perceived scene.

C. Rail transportation

Even the trains remain trashed of equipment due to bad weather conditions each year. The fool-proof devices have not been yet developed to mitigate this issue [68]. Several trains get delayed or even get canceled because of the weather degraded environment. Handling such issues require the use of image desmogging models to stream a cleared scene for drivers [69].

D. Ocean/sea transportation

Sea fog affects the navigation of ships. It can restrict the movement of a ship onward the ship channel. Thus might even advert to the inland traffic systems. The forecasts of sea fog are important while communicating the implied information to the traffic personnel [70].

E. Cable car transportation

A cable car is a transportation system that depends upon cables for pulling vehicles along or lowering them steadily [71]. Several cable cars get delayed or at times even get canceled because of the presence of heavy fog/smog. For handling this issue, the desmogging models can be used to show the streamed visibly restored scenes for the cable car drivers.

1.8 Performance metrics

The quality of a desmogging model can be well analyzed by considering the performance metrics.

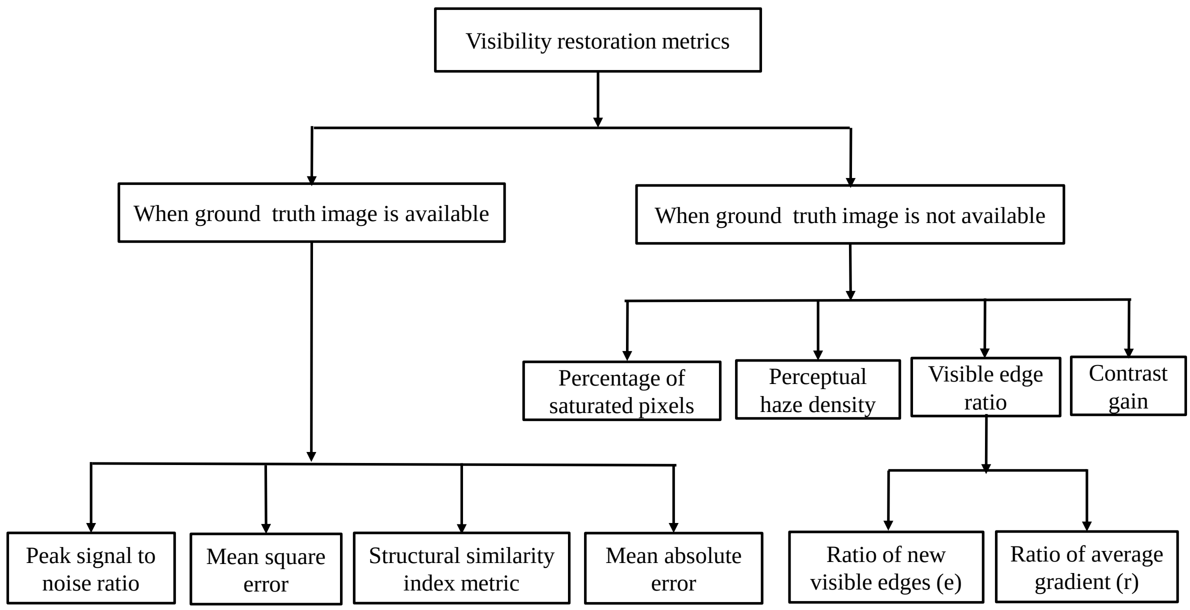

Figure 1.13: Performance metrics for desmogging models

Figure 1.13 shows various performance metrics which can be employed to estimate the usefulness of the present desmogging models [72]. In desmogging models, the performance measure can be required to be performed in two situations, *i.e.,* in the availability of ground truth image and in the unavailability of ground truth image [73].

1.8.1 When a ground truth image is available

This includes performance evaluations that consider a ground truth image (*i.e.,* reference image) in advance. This image is an actual restored image captured in the clear weather. Nevertheless, actual restored images are particularly known when someone wants to validate its desmogging model on standard weather degraded image datasets. When the actual image is already known, several quality meaures including Peak Signal to noise ratio (PSNR), Mean squared error (MSE), and structural similarity index metric (SSIM) are considered while evaluating the performance of desmogging models.

A. Mean square error

Mean square error (MSE) is a method for error calculation that averages the squared difference between the reference image (G_t) and the smog-free image (I_r) generated via the restoration model. The MSE is a positive integer that varies from 0 to ∞. The mathematical representation of MSE can be defined as [74]:

$$MSE = \frac{1}{R \times C} \sum_{j=1}^{R} \sum_{i=1}^{C} [G_t(i,j) - I_r(i,j)]^2 \tag{1.5}$$

$G_t(i,j)$ depicts the pixel value from a ground truth image. Whereas $I_r(I,j)$ represents corresponding pixel intensities from a smog free image. Also, i and j denotes pixel's coordinates. R and C represent rows and columns.

B. Peak signal to noise ratio

Concerning the restored image, Peak signal to noise ratio (PSNR) estimates the mean squared error after implementing the restoration model. Maximum PSNR value signifies that the effect of weather degradation is removed proficiently. PSNR can be computed as follows [74]:

$$PSNR = 10\log_{10}\left(\frac{255^2}{MSE}\right) \tag{1.6}$$

C. Structural similarity index metric

While calculating the PSNR, some edges might get neglected. The structural similarity index metric (SSIM) evaluates the relevance in such cases. The value of SSIM closes to 1 means that the restored image possesses higher structural quality. This is measured as [74]:

$$SSIM(m,n) = \left(\frac{2\mu_m\mu_n + c_1}{\mu_m^2 + \mu_n^2 + c_1}\right)\left(\frac{2\mu_{mj} + c_2}{\sigma_m^2 + \sigma_n^2 + c_2}\right) \tag{1.7}$$

Here, μ_m and μ_n denotes sample means of m and n, and the sample variances of m and n are indicated by σ_m^2 and σ_n^2, respectively. The cross-covariance of m and n is given by σ_{mj}. The values for c_1 and c_2 are set to 0.01 and 0.03.

1.8.2 When a ground truth image is not available

The ground truth images are in several cases not available in real-world applications. Measuring effectiveness thus becomes a challenging task in such cases. The images restored by the models have high contrast in comparison with the degraded images. Percentage of saturated pixels (ρ),Contrast gain (C_g), Perceptual weather degradation density (D_f), and Visible edges ratio are considered for evaluating the desmogging models.

A. Contrast gain

Contrast gain (C_g) is estimated as an average contrast difference between input weather degraded image (I) and a desmoggy image (I_r). C_g is calculated as below [75]:

$$C_g = C_I - C_I^r \tag{1.8}$$

Here, C_I^r and C_I represent average contrast of restored image (I_r) and smoggy image (I), respectively. For an image ($I(i,j)$) with size ($R \times C$). The average contrast ($C_v(i,j)$) is calculated as:

$$C_v(i,j) = \frac{1}{R \times C} \sum_{i=0}^{R-1} \sum_{j=0}^{C-1} C(i,j) \tag{1.9}$$

Here, $C(i,j)$ can be written as:

$$C(i,j) = \frac{s(i,j)}{m(i,j)} \tag{1.10}$$

where

$$m(i,j) = \frac{1}{(2p+1)^2} \sum_{k=-p}^{p} \sum_{l=-p}^{p} I(i+k, y+l) \tag{1.11}$$

$$s(i,j) = \frac{1}{(2p+1)^2} \sum_{k=-p}^{p} \sum_{l=-p}^{p} |I(i+k, y+l) - m(i,j)| \tag{1.12}$$

Tripathi and Mukhopadhyay [76] shown that a restored/actual image has more contrast than the weather degraded image. Hence, C_g should be a positive real number.

B. Percentage of saturated pixels

C_g The increased contrast in the restored image may lead to a saturated pixel problem. Consequently, the computation of the Percentage of saturated pixels (ρ) becomes necessary to evaluate a restoration model [75]. ρ can be defined as:

$$\rho = \frac{S_p}{R \times C} \tag{1.13}$$

Here, S_p denotes the pixels count that were not entirely black or white in the weather degraded image but became saturated on the application of the desmogging model to the image. The desmogging model with a lower value of ρ is considered more effective.

C. Visible edges ratio

Another measure for the performance of the proposed model is analyzing the ratio of new visible edges (e) and the ratio of average gradient ($\bar{r}$). The e describes the rate of visible edges that is improved for the restored images and is computed as below [77]:

$$e = \frac{n_k - n_l}{n_l} \tag{1.14}$$

Here, n_l and n_k represent the count of the edges visible in the restored image (I_r) and weather degraded image (I_s), respectively.

The desmogging model with a lower value of e is considered less effective as the edges of the restored image are weak, conversely, more e represents stronger edges.

The restoration degree $\bar{r}$ uses the gradients of visible edges from the smog free image for depicting the restoration degree of the image texture details and edges. $\bar{r}$ can be defined as:

$$\bar{r} = e^{\left[\frac{1}{n_k} \sum_{i \in \phi_k} log\, r_i\right]} \tag{1.15}$$

Here, r_i is set to $\frac{\Delta k}{\Delta l}$. The gradients of an image are represented using Δk and Δl, respectively. r_i represents the set of visible edges of I_r. A maximum value of $\bar{r}$ states that the specified desmogging model has more capacity of preserving edges in comparison with other models.

D. Perceptual weather degradation density

An efficient model predicting weather degradation density is considered in [78]. The model divides the degraded image into $N \times N$ sections and then computes the aggregate average values. These $N \times N$ sections are also used for the evaluation of different factors including image entropy, DCP, sharpness, variance, color saturation, contrast energy, colorfulness, *etc.* Multivariate Gaussian (MVG) fit is estimated in n dimensions for the features by the implementation of Mahalanobis measure [79]. This MVG is computed as follows:

$$P(s) = \frac{1}{\sqrt{(2\pi)^n |D|}} exp\left(-0.5 * (s-\mu)^t C^{-1} (s-\mu)\right) \tag{1.16}$$

Here, μ indicates the mean, s represents the weather degradation aware statistical features, and $n \times n$ shows the covariance matrix of weather degraded features. Additionally, C^{-1} and D depict covariance matrix inverse for MVG and determinant, respectively. The determinant and matrix inverse can be obtained by applying the maximum likelihood (ML) estimation [80]. The Mahalanobis-like distance is calculated as follows:

$$D = \sqrt{(m_1 - m_2)^t \left(\frac{C_1 + C_2}{2}\right)^{-1} (v_1 - v_2)} \tag{1.17}$$

Here, m_1 and m_2 represent the mean vectors and C_1 and C_2 denotes the covariance matrix for MVG model of the restored image and matrix for MVG fit of the weather degraded image.

Moreover, L_f can be calculated for the judgment of the restoration level. L_f represents the distance norm of MVG versus weather degraded aware statistical features. The data is obtained of a weather degraded test image and normal MVG model from a group of 500 weather degraded images [78]. Afterward, weather degradation density (D_h) can be calculated as:

$$D_h = \frac{D}{1+L_f} \tag{1.18}$$

Values of D_h are proportional to the corresponding weather degraded density.

1.9 Thesis organization

This thesis is devoted to design and development of desmogging models for weather degraded images. The extensive review of the existing desmogging techniques is included in Chapter 2. Design and implementation of the proposed desmogging models are discussed in Chapters 3 to 6. The concluding remarks and future directions are discussed in Chapter 7. The chapter-wise organization of thesis work is given below:

Chapter 2: Related work

In Chapter 2, a comprehensive and illustrative literature review in the domain of desmogging models is provided. The details of the existing desmogging models along with their strengths and weaknesses are also presented. The existing models are compared with respect to different features.

Chapter 3: Desmogging of smog affected images using illumination channel prior

The existing researches majorly are designed for the restoration of images affected by rain, dust, fog, haze, etc. Thus, the designed models do not provide appropriate performance for the smog affected images. This chapter proposes a novel illumination channel prior for the significant restoration in the case of smoggy images. The filter for efficient refinement of transmission map, namely gradient magnitude based filter is also proposed. Finally, subjective and quantitative analyses are drawn for evaluating the performance of the proposed desmogging approach.

Chapter 4: Image desmogging using information gain based bilateral filter

Many visibility restoration models approaches have been designed to restore smog from still images. But, removing the smog from images is defined as an ill-posed problem. Therefore, a novel desmogging approach is designed. Initially, gradient channel prior is used to estimate the optical information of smog affected images. Thereafter, a information gain based filter is proposed to improve the transmission map. The smog-free image is then computed using an improved restoration model.

Chapter 5: Desmogging using oblique gradient profile prior and variational minimization

In this chapter, a novel transmission map estimation is developed by deploying weighted integrated transmission maps obtained from foreground and sky regions. Additionally, the further refinement of the transmission map is done by using an integrated variational regularized model with hybrid constraints. However, the suggested approach undergoes the hyper-parameters tuning issue. To resolve this issue, the chapter includes a Non-dominated sorting genetic algorithm (NSGA) for tuning the hyper-parameters of the proposed approach.

Chapter 6 Conclusions and future work

The thesis is hereby concluded in this chapter, emphasizing the contributions made towards the proposed research domain and presenting future directions in this research area.

Chapter 2

Related work

Outline

This chapter incorporates a comprehensive review of desmogging models. The desmogging models are broadly categorized into six categories. These are variational, filtering, enhancement, meta-heuristic, fusion, and depth estimation based models. Finally, the comparisons have been done on the existing models while considering certain characteristics. The major objective of this chapter is to evaluate the shortcomings present in the present image desmogging models.

2.1 Review of literature

This section includes a comprehensive review of existing well-known smog removal techniques. Also, a comparative analysis of different models is given.

2.1.1 Review on smog removal techniques

Xiao et al. have utilized DCP with segmentation and gamma correction to remove the color distortion and halo artifacts issues with desmogging techniques. Initially, well-known guided image filter has been utilized to improve the segmentation of brighter segments. Median filter has been utilized to evaluate the edge information. Therefore, an efficient transmission map has been evaluated. In the end, gamma correction has been implemented to remove the smog from images. This technique has shown lesser color distortion and halo artifacts with desmogged images [81].

Ma et al. proposed a fusion based desmogging model for removing the smog from smoggy images. A well-known guided image filter has also been used to reduce the edge degradation issue with existing desmogging techniques. In the end, the white balancing has also been utilized [49]. But, this technique may introduce halo artifacts in the restored images.

Zhu et al. proved that an efficient transmission map estimation technique has an ability to restore the weather degraded images in a significant way. However, it is an under-constraint issue. It has been observed that the DCP is an efficient technique to estimate the transmission map. It has been found that the energy minimization has ability to further improve the transmission map obtained from DCP. The energy function integrated DCP with piecewise smoothness. However, it suffers from poor computational speed issue [82].

Want et al. used a superpixel technique to resolve the issue of halo artifacts and color distortion in the sky area. Therefore, the proposed restoration model can handle the sky region issue with existing desmogging techniques [83].

Zhao et al. designed a multi-scale tone model for efficiently estimating the transmission map in a more significant way. Therefore, it can restore the image with multiple scales [84]. However, it provides poor results for large smog gradients.

Zhu et al. designed a supervised learning based desmogging approach for estimation of the depth map in a more efficient way. Therefore, it provides more efficient results than DCP based desmogging techniques [1]. However, it require synthetic images for training. But, in real time applications it is difficult to obtain such a huge data number of images for different kinds of applications [85].

Kumari et al. designed a look-up table with the help of gamma correction and median filter. It has an ability to provide restored images with a lesser number of halo artifacts and good edge preservation [86].

Ding et al. considered an L2-norm for the evaluation of transmission map in a more effective way. Then, a guided image filter has been considered for the refinement of the transmission map. Therefore, it has the ability to preserve the edges in a more efficient way [87].

Li et al. developed a weighted guided filter for the refinement of the transmission map in a more effective manner. It takes lesser computational time without losing the illumination of restored images [88].

Li et al. implemented change of detail prior that evaluate the thickness of smog. The prior is stable for the local regions of the smoggy image containing objects in different depths [89]. But, the model proved incapable of preserving the edges of a haze free image.

Li et al. integrated weighted guided filter with Koschmiedars law to estimate atmospheric viel in more efficient way. The model has the capability of restoring images with lesser gradient reversal artifacts and halo artifacts. [90].

Su et al. used well-known bilateral filter to achieve local smoothness and to preserve edges in an more significant way. It minimizes the adverse effects that occurs due to the dissimilarity between in global atmospheric light [4]. However, the restored image in this case may contain halo and gradient reversal artifacts.

Guo et al. proved that the efficient tuning of the restoration model can provide more efficient desmogging results. The genetic algorithm has been used to tune the desmogging parameters. It achieves optimistic desmogging parameters subject to ensuring the quality of restored images [91]. However, the genetic algorithm suffers from poor convergence speed issues.

Golts et al. [6] designed an image desmogging approach using Dark channel prior (DCP). In this model, regularization is achieved using learning process. Li et al. [7] proposed a semi-supervised learning based desmogging approach. The approach applied deep Convolutional Neural Network (CNN) for supervised and unsupervised learning. Gradient priors and dark channel are implemented to explore the details of clear images.

Liu et al. [92] proposed a unified variational model that involved total variation regularization for image desmogging. The model uses $l1-$norm regularization for repressing the inverted scene radiance and scene transmission. The desmogging model is then optimized by using the direction minimization approach.

Hodges et al. [93] applied deep neural networks for removing the weather impacts from the degraded image. The authors then applied Siamese network architecture in order to train the proposed model for unmatched images.

Ancuti et al. [8] proposed a Color channel transfer (CCT) for desmogging of images. CCT utilize a color transfer scheme for compensating for the chromatic loss in the color channel. Gu et al. [9] introduced another desmogging algorithm built on total generalized variation (TGV) regularizations. The proposed model makes use of two TGVs for improving the transmission map and image intensity.

Ju et al. [94] executed another model using gamma correction prior (GCP) to clear the smog from weather degraded images. The scene albedo is obtained using a visual indicator and a global-wise strategy, thus the smoggy image is restored. Zhu et al. [95] implemented a generative adversarial network (GAN) to desmog the image. This model utilizes a compositional generator and a deeply supervised discriminator. The discriminator's role is to make sure that the output by the generator should look like a clear image.

Ren et al. [96] made use of multi-scale deep neural network for image restoration from a degraded image. The transmission map is obtained by using a coarse-scale net. This transmission map is then used in refining the edges. Khan et al. [10] introduced the use of Wavelet transform (WT) to recover the image. The atmospheric light is calculated from the given smoggy images by dividing and restoring the high-frequency sub-bands.

2.1.2 Comparative analysis of existing smog removal techniques

Table 1 illustrates the comparative analyses of some well-known visibility restoration approaches based upon some necessary characteristics of desmogging techniques. It has been observed that each desmogging method has certain pros and cons. Therefore, no technique performs efficiently in every case. Therefore, designing an efficient visibility restoration technique is still an open area for researchers.

Table 2.1: Comparative analyses of the existing smog removal techniques

Ref. No.	Year	Technique	Edge preservation	Speed	Color distortion	Halo artifacts	Large smog gradients
[27]	2011	DCP	✗	Average	✓	✗	✗
[36]	2012	Improved DCP	✗	Average	✓	✗	✗
[47]	2013	Bilateral filter	✓	Average	✗	✗	✗
[35]	2013	Physical model	✗	Average	✓	✗	✗
[97]	2014	Trilateral filter	✓	Good	✗	✗	✗
[48]	2015	Canonical correlation	✗	Good	✗	✓	✓
[3]	2015	Histogram Modification	✗	Good	✗	✗	✓
[88]	2015	Weighted guided filter	✓	Good	✗	✓	✗
[98]	2015	Deformed model	✓	Average	✗	✓	✗
[90]	2015	Edge preserving	✓	Average	✗	✓	✓
[89]	2015	Change of detail	✓	Average	✗	✗	✓
[99]	2015	Hierarchical model	✓	Average	✗	✗	✓
[86]	2015	Regression	✗	Good	✗	✓	✓
[91]	2016	Genetic algorithm	✗	Average	✗	✓	✓
[83]	2016	Scattering model	✗	Average	✗	✓	✓
[49]	2016	Image fusion	✗	Average	✗	✓	✓
[5]	2016	Gain filter	✗	Average	✗	✓	✓
[43]	2017	Gain intervention	✓	Good	✗	✓	✗
[2]	2017	Improved restoration	✓	Average	✗	✓	✓
[100]	2017	Fusion	✓	Good	✗	✗	✓
[101]	2017	Optical depth	✗	Good	✗	✓	✓
[102]	2018	Notch Gradient	✓	Good	✗	✓	✓
[103]	2018	Controlled Gaussian	✓	Good	✗	✗	✓
[104]	2018	Linear transmission	✗	Good	✗	✓	✓
[105]	2018	Segmentation	✗	Good	✗	✓	✓
[106]	2018	Improved DCP	✗	Good	✗	✓	✓
[107]	2019	Dual fusion	✗	Good	✗	✓	✓
[108]	2019	Fusion	✗	Good	✗	✓	✓
[93]	2019	Deep neural networks	✓	Average	✓	✓	✓
[109]	2019	Alternating model	✓	Good	✓	✗	✓
[110]	2020	Pyramidal residual	✗	Good	✗	✓	✓
[10]	2020	Radiance transformation	✗	Good	✗	✓	✓
[94]	2020	Gamma correction prior	✗	Good	✓	✓	✓
[7]	2020	Semi-supervised model	✗	Slow	✗	✓	✓
[6]	2020	Unsupervised DCP	✓	Average	✓	✓	✓

2.2 Research gaps

After the detailed analyses of the existing desmogging models, the following research gaps are identified.

i. The related work has shown that the majority of existing desmogging techniques perform pooly for images with large smog gradients.

ii. Majority of existing researchers have neglected the use of parameter tuning to efficiently restore the weather degraded images.

iii. It has been observed from the literature that the meta-heuristic techniques have ability to tune the desmogging parameters for efficient desmogging of smoggy images. However, majority of existing researchers have neglected the use of meta-heuristic techniques.

iv. Majority of existing researchers have either focused on hazy or on foggy images. No much work has been done for smoggy images.

2.3 Problem Formulation

Imaging under smoggy environment suffers from poor visibility issue. These images are often categorized as degraded images. These images reduce the performance of many computer vision applications. Therefore, the main necessity is to design an efficient image restoration technique. From related work, it has been observed that existing techniques suffer from color distortion, edge degradation, gradient reversal and halo artifacts.

In order to overcome the different problems with existing technique, a novel meta-heuristic techniques based smog removal algorithms will be proposed in this research work. The depth map can automatically extract the global atmospheric light and roughly eliminate the atmospheric veil. To make depth map more effective, meta-heuristic optimization techniques will be utilized to optimistically find various static variables used by the existing smog removal techniques.

The atmospheric veil will be refined by using fast image filters. To reduce the color distortion and to preserve the edges of the restored images, the transmission map will be recomputed. By utilizing the global atmospheric light and transmission, the model developed will be able to produce a smog free image in more optimistic manner. The use of improved filters have the ability to improve the coarse estimated atmospheric veil in order to reduce halo artifacts. The transmission map is also refined with objective to prevent the color distortion and preserve edges of restored image. The proposed technique will be tested on remote sensing, underwater images and road side images.

2.4 Objectives

To overcome the aforementioned issues, the following objectives are formulated:

i. To propose a novel desmogging model by modifying the well-known dark channel prior based desmogging model.

ii. To propose meta-heuristic approaches based smog removal approach to optimistically evaluate various static variables required by smog removal approach such as restoration value, patch size, white balance etc.

iii. To improve the coarse estimated atmospheric veil by designing different image filters in order to remove the halo artifacts and to preserve significant detail of restored images with large smog gradients.

iv. To evaluate the effectiveness of the proposed approach certain performance metrics will also be considered as:

   (a) Contrast gain
   (b) Percentage of saturated pixels
   (c) New visible edges
   (d) New edge gradients
   (e) Perceptual of fog density
   (f) Peak signal to noise ratio
   (g) Mean squared error
   (h) Execution time

2.5 Hypothesis for research

To implement the proposed desmogging models, the following hypothesis are defined:

Hypothesis i. It has been assumed that the smoggy images dataset will be obtainable in the form of low, moderate and high density affected smoggy images.

Hypothesis i. It has been also assumed that the modification in depth map estimation approaches such as dark channel prior, gradient channel prior, color attenuation prior, etc. can improve the accuracy of depth map estimation.

Hypothesis i. Also, it has been assumed that the modified or the designed filter have an ability to refine the transmission map and the atmospheric veil in an efficient manner.

2.6 Datasets and tool used

2.6.1 Tool

The proposed approach is implemented on HP notebook computer with Intel(R) Core(TM) $i7$-4210U CPU @2.40 GHz and 16GB RAM. The experimentation has been carried out on MATLAB 2018a software with the help of image processing software. The window size of channel priors is taken from 3×3 to 11×11 pixels.The parameters setting for the above discussed algorithms are done as per recommended in the original papers.

2.6.2 Datasets

While evaluating the effectiveness of the proposed approaches, the implementations are tested on 9 standard databases of synthetic smoggy/hazy/foggy images. The set of 200 real-time smoggy images are also considered. The details of the data-sets can be found in Table 2.2. These majorly include synthetic images. The images are taken from Foggy road image database (FRIDA) [111], Realistic single image restoration (RESIDE) [112], Waterloo IVC restored image database [113], D-HAZY [114], and Foggy road image database 2(FRIDA2) [115]. Moreover, some real-life images are captured in smoggy environment and utilized for carrying out the experimentation.

Table 2.2: Degraded images datasets used

Dataset	Description	Number of images
RESIDE (ITS)	ITS (Indoor Training Set)	50
RESIDE (OTS)	OTS (Outdoor Training Set)	50
RESIDE (SOTS)	SOTS (Synthetic Objective Testing Set)	50
RESIDE (RTTS)	RTTS (Real-world Task-Driven Testing Set)	50
RESIDE (HSTS)	HSTS (Hybrid Subjective Testing Set)	20
FRIDA	Foggy Road Image Database	90
FRIDA2	Foggy Road Image Database 2	120
IVC	Waterloo IVC restored image database	25
D-HAZY	Dataset to evaluate restoration algorithms	100
Real-life	Real-life images	200

Chapter 3

Desmogging of smog affected images using illumination channel prior

Outline

The existing researches majorly are designed for the restoration of images affected by rain, dust, fog, haze, etc. Thus, the designed models do not provide appropriate performance for the smog affected images. This chapter proposes a novel illumination channel prior for the significant restoration in the case of smoggy images. The filter for efficient refinement of transmission map, namely gradient magnitude based filter is also proposed. Finally, subjective and quantitative analyses are drawn for evaluating the effectiveness of the proposed desmogging model.

3.1 Background

Smog contains a combination of fog and smoke present in the atmosphere [116]. Smog generally occur in winter season when warm water cools quickly due to low temperature and also at a same time pollution is present in the environment. Designing a novel desmogging approach is an ill-posed problem. Therefore, not much work is found in the literature to remove smog from images [54]. However, existing defogging and dehazing approaches can be applied to remove smog from images. However, these restoration approaches are not so-effective for smoggy images [91, 47, 90, 39].

A novel gain intervention-based filter has been designed and implemented in [117]. It has an ability to restore the images in an efficient manner. Fourth-order partial differential equations based anisotropic diffusion model is used in [118]. This model can be utilized during the desmogging process. An integrated dark and bright channel prior based model can restore smoggy images in an efficient manner [119]. An image enhancement model based on gamma correction and dark channel prior is implemented in [120]. An approximation radiance darkness prior is designed and implemented in [121]. It has been found from [122] that the models discussed in [117] to [121] can be used to restore the smoggy images. However, these models are effective only for smoggy images with low degree of smog.

This chapter makes the following contributions:

- An illumination channel prior is proposed to restore smoggy images. This is achieved by replacing the dark channel prior with illumination channel. Therefore, it allows the proposed approach to evaluate the transmission map and atmospheric light in an efficient manner. It has also an ability to handle sky region and gradient reversal artifact issues with existing restoration approaches.
- An edge-preserving filter is proposed for accurately refining the transmission map. Further, it is improved via a newly proposed edge-preserving loss function.
- As existing restoration models designed for dehazing and defogging are not so-effective for smoggy images, therefore in this work, a modification of restoration model is also proposed.
- Extensive experiments are conducted on real-world smoggy images. In addition, comparisons are performed against several recent restoration approaches.

3.2 Proposed illumination channel prior based desmogging approach

This section discusses the designed desmogging model. Figure 3.1 demonstrates the overall flow of the designed desmogging model.

3.2.1 Depth map estimation

Initially, an illumination channel is designed to estimate depth information from smoggy image (I_m) as

$$I^d(p,q) = \delta_{y\in\Psi(p,q)}\Big(\delta_{c\in(r,g,b)}\big(I_s^c(l)\big)\Big) \tag{3.1}$$

Here, I_m^c is the available color channels of I_m. δ represents the illumination channel prior. $\Psi(p,q)$ shows the local window.

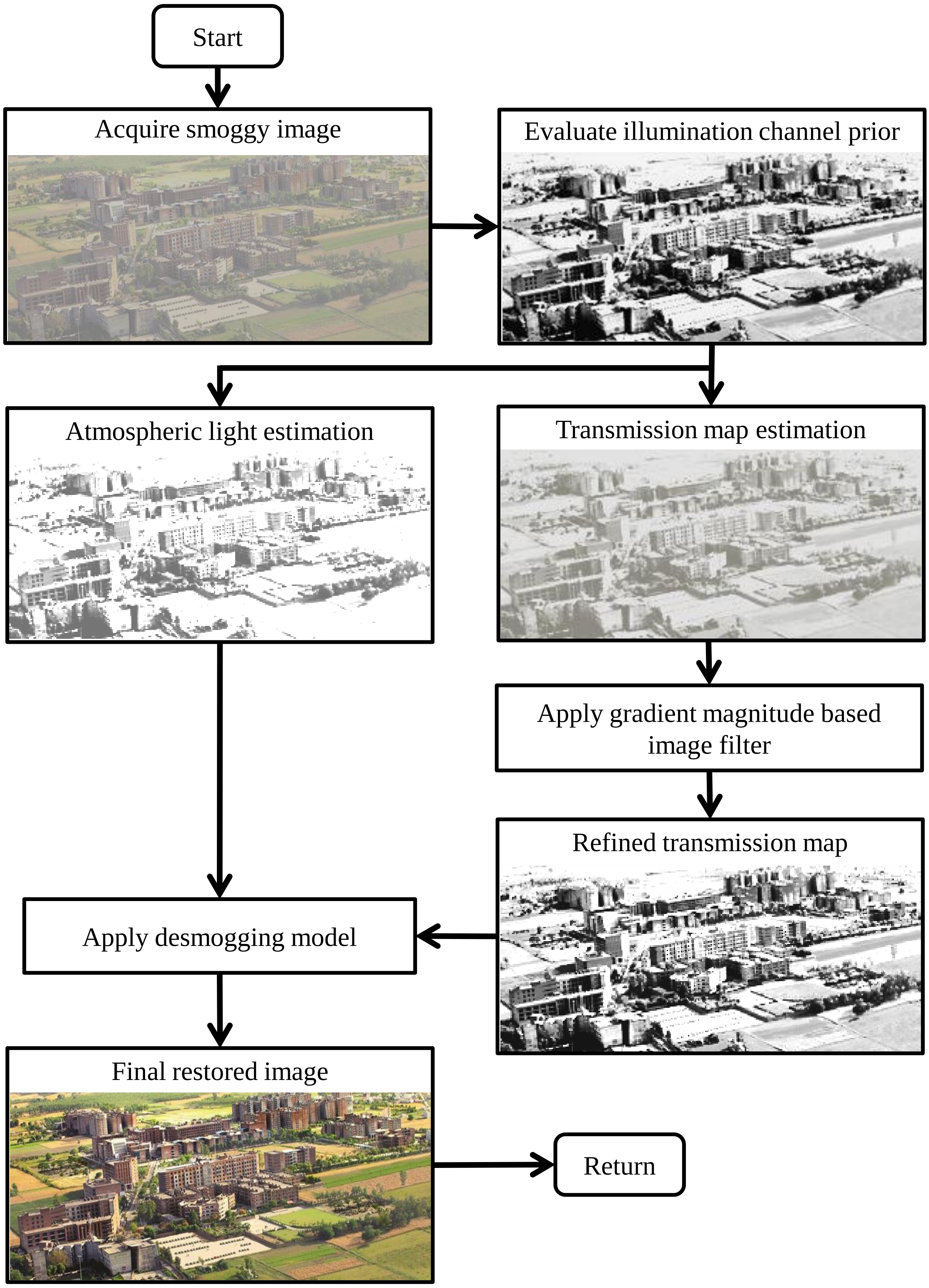

Figure 3.1: Flow of the proposed illumination channel prior approach.

3.2.2 Atmospheric light

Atmospheric light (A_l) has an important role to restore the smoggy image, it can be calculated as [27]:

$$A_l(p,q) = I_m\left(\max_c\left(I_m^c\right)\right). \tag{3.2}$$

3.2.3 Transmission map

Transmission map ($\tilde{t}$) is another building block of desmogging model and it is achieved by:

$$\tilde{t}(p,q) = 1 - \min_{y\in\Psi(p,q)}\left(\min_c \frac{I_m^c(y)}{A_l^c}\right) \tag{3.3}$$

3.2.4 Coarse atmospheric light estimation

The coarse atmospheric light ($A_{viel}(p,q)$) evaluation is performed by [27]:

$$A_{viel}(p,q) = \beta \min_{y\in\Psi(p,q)}\left(\min_c \frac{I_m^c(y)}{A_l^c}\right) \tag{3.4}$$

In this chapter, gradient magnitude based filter is utilized to refine t as:

$$\tilde{t}(p,q) = \sigma(p,q) - J_O^{tf}\left(\left|t-\sigma(p,q)\right|\right) \tag{3.5}$$

Here, $\sigma(p,q)$ is standard deviation.

3.2.5 Restoration model

Lastly, the smog free image (A_r) is recovered by the use of restoration model as:

$$A_r(p,q) = \frac{I_m(p,q) - A_l}{\max(\tilde{t}(p,q), t_l)} + A_l \tag{3.6}$$

3.3 Performance analyses of the illumination channel prior

To evaluate the effectiveness of the designed desmogging model seven existing restoration models are considered. These approaches are DCP [27], CAP [1], CoD [89], WGIF [88], LTQ [123], L_1 norm [11], and FVID [12] on dataset obtained from [124].

3.3.1 Visual analyses of illumination channel prior

The visual results of the designed desmogging approach is compared with seven existing desmogging techniques on some popular benchmark smoggy images.

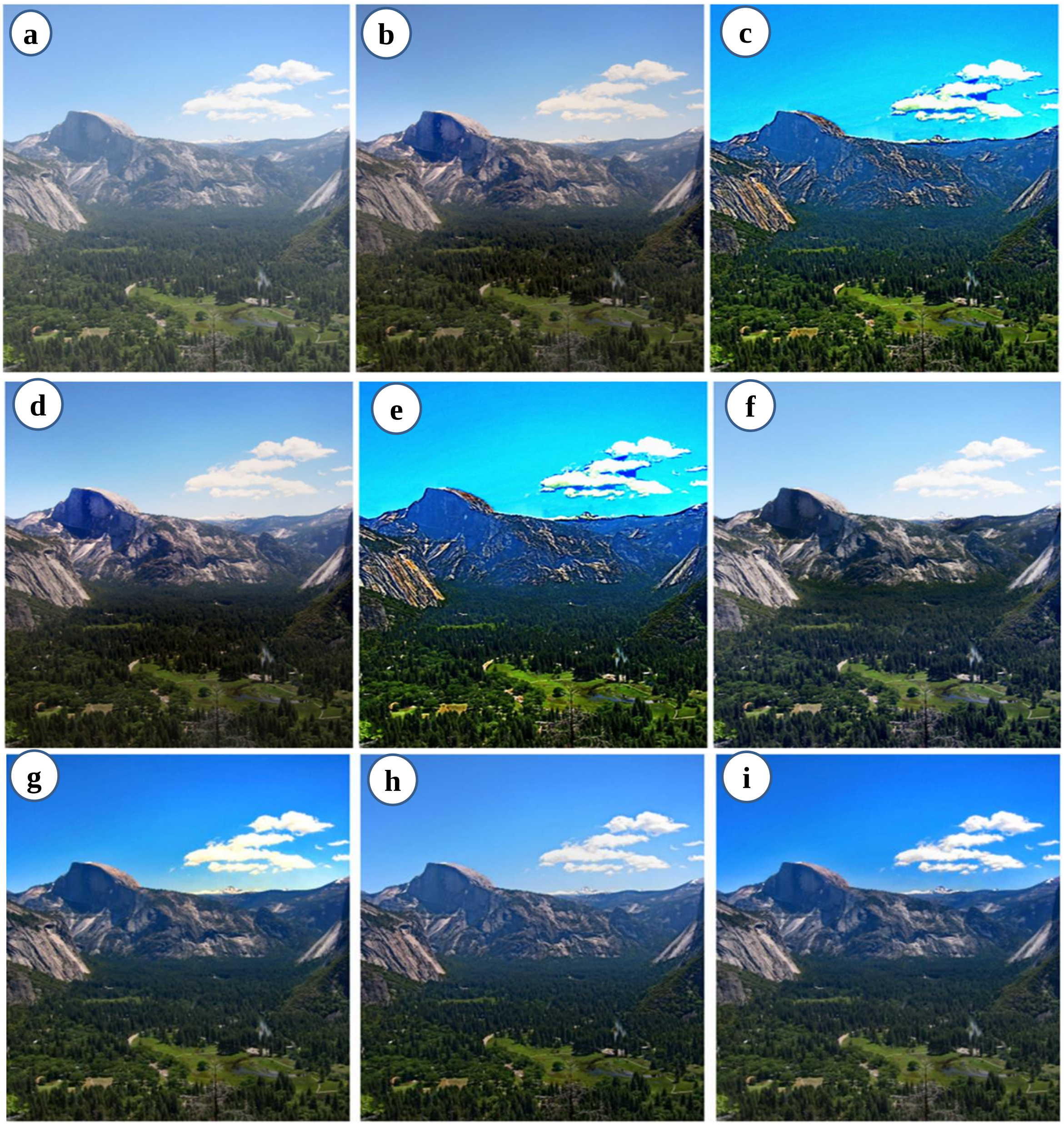

Figure 3.2: Results of desmogging models (a) Input image, (b) DCP [6], (c) CNN [7], (d) CTT [8], (e) TGV [9], (f) WT [10], (g) L_1 norm [11], (h) FVID [12] and (i) Proposed NICP model.

Desmogging results in Figures 3.2 3.3, and 3.4 have demonstrated the benefits of the proposed desmogging model. DCP [27] and CTT [8] contain sky region and abundant textures contain headlights that are significantly different from the atmospheric light. It can be seen that these approaches are not efficient to remove the smog for images effected with large smog gradient.

CNN [7] and TGV [9] tend to oversmooth fine image details and degrade the quality if the especially for images which are effected from large smog gradient. WT [10], L_1 norm [11], and FVID [12] show remarkable good results compared to the other approaches. However, these approaches fail while preserving the texture information of the restored smoggy images. The designed NICP approach does not suffer from texture, edge and color distortion issues.

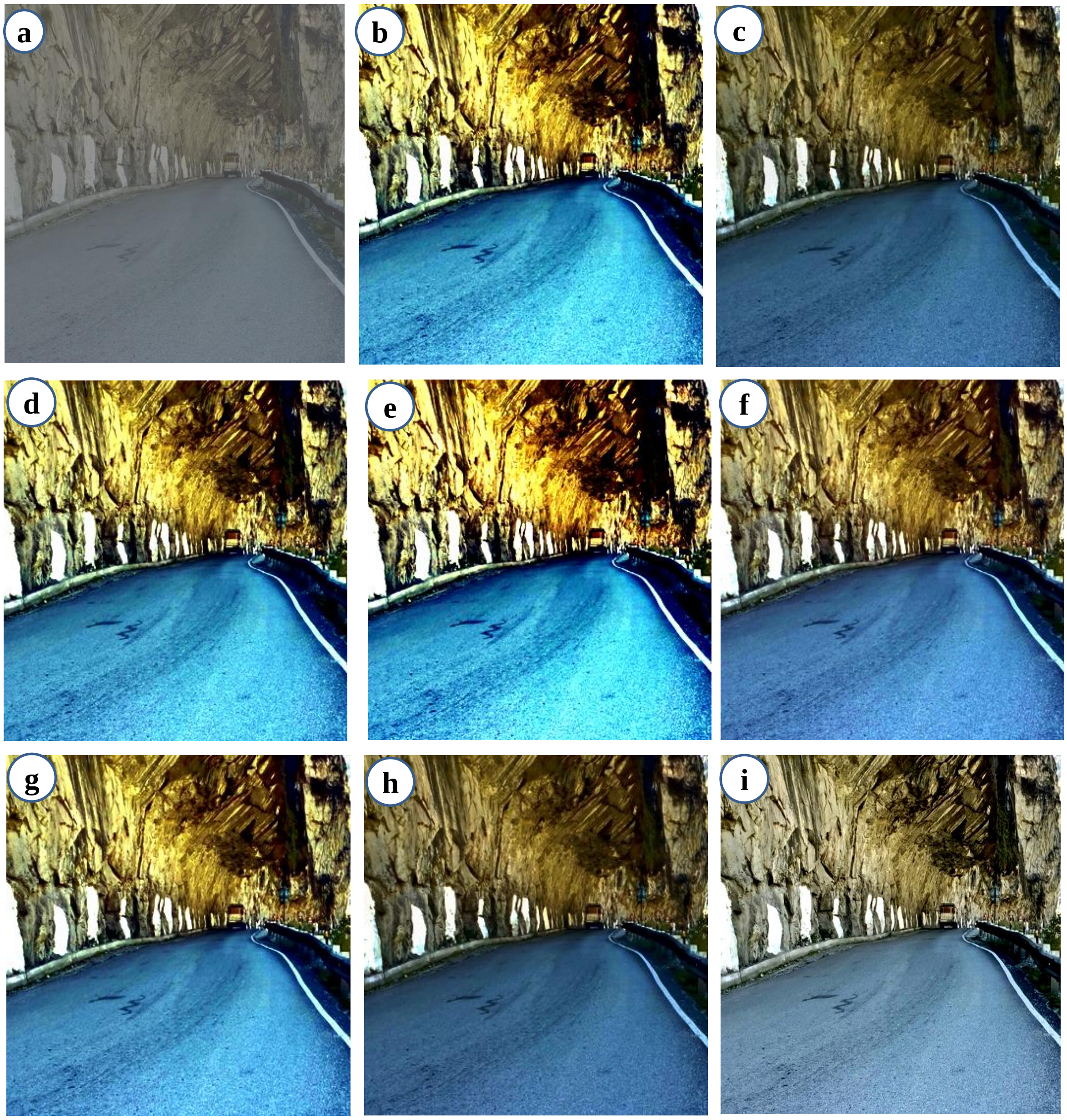

Figure 3.3: Results of desmogging models (a) Input image, (b) DCP [6], (c) CNN [7], (d) CTT [8], (e) TGV [9], (f) WT [10], (g) L_1 norm [11], (h) FVID [12] and (i) Proposed NICP based desmogging model.

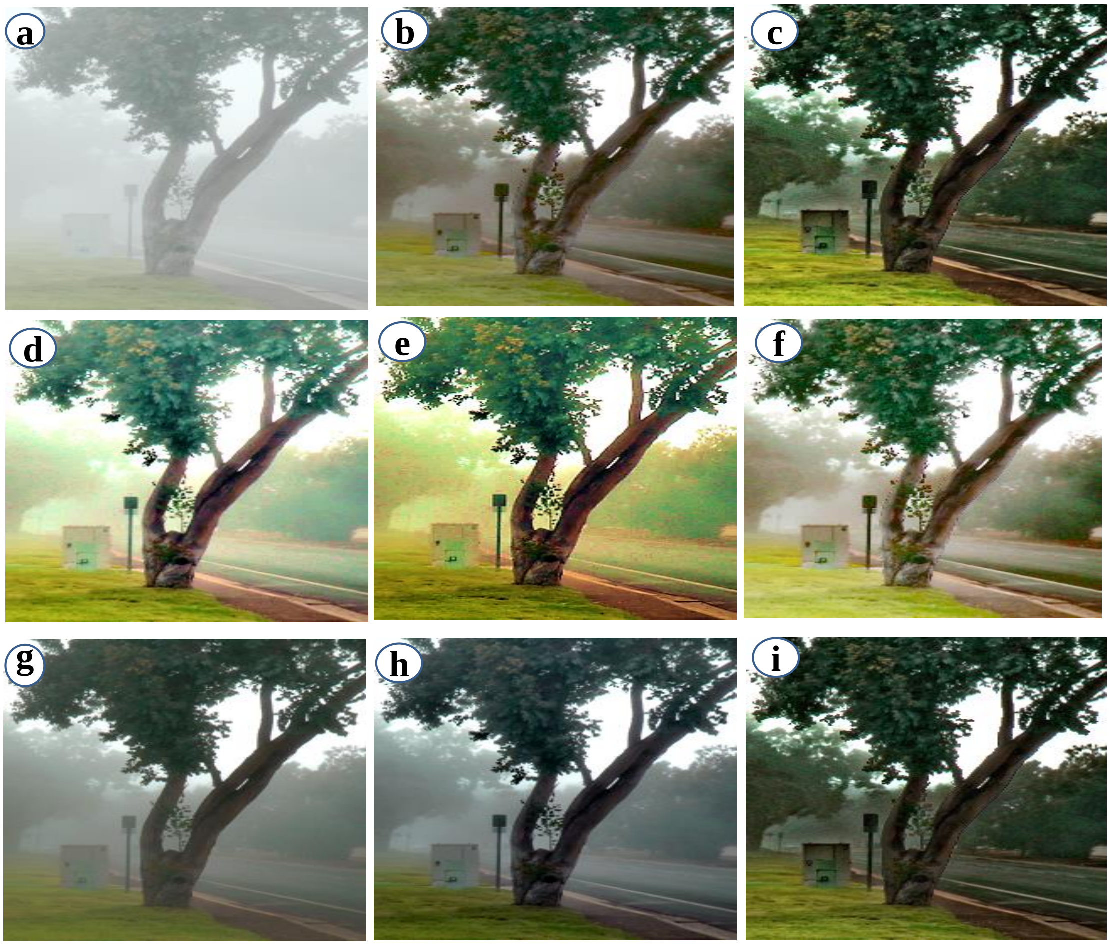

Figure 3.4: Results of desmogging models (a) Input image, (b) DCP [6], (c) CNN [7], (d) CTT [8], (e) TGV [9], (f) WT [10], (g) L_1 norm [11], (h) FVID [12] and (i) Proposed NICP based desmogging model.

3.3.2 Quantitative analyses of illumination channel prior

The comparisons among the designed and the competing desmogging models are also carried out while considering the well-known performance metrics such as contrast gain (CG), percentage of saturated pixels (S_p), smog gradient, visible edges, execution time (ET), structural similarity index metric, and peak signal to noise ratio. Contrast gain (CG) in the restored images is more than the degraded images. Thus the average contrast is improved in the restored images [75].

Table 3.1 demonstrates CG analysis. It can certainly be found in the visual analysis that the designed NICP based desmogging approach has a significant CG values than competing restoration approaches.

Table 3.1: Contrast gain analysis of the illumination channel prior

Img.	DCP	CNN	CTT	TGV	WT	L_1	FVID	NICP
IM_1	1.8712	1.7678	1.7373	1.8906	1.8336	1.7638	1.8363	1.9123
IM_2	1.7856	1.8099	1.7758	1.7483	1.7712	1.7263	1.8239	1.8456
IM_3	1.7419	1.8932	1.8637	1.8357	1.8658	1.7473	1.7686	1.9149
IM_4	1.7466	1.8115	1.8601	1.8447	1.8428	1.8182	1.8015	1.8818
IM_5	1.8647	1.7785	1.8245	1.8216	1.7983	1.8391	1.7383	1.8864
IM_6	1.8927	1.8988	1.7797	1.7652	1.8658	1.7731	1.8229	1.9205
IM_7	1.8318	1.7297	1.8239	1.8998	1.8368	1.8657	1.8734	1.9215
IM_8	1.8989	1.7707	1.7606	1.7443	1.8684	1.7246	1.7295	1.9206
IM_9	1.7269	1.8077	1.8048	1.7998	1.7711	1.7628	1.8537	1.8754
IM_{10}	1.8446	1.7733	1.8493	1.8266	1.8002	1.7967	1.7546	1.8707
IM_{11}	1.8496	1.7974	1.7681	1.8046	1.8614	1.8889	1.8553	1.9106
IM_{12}	1.8347	1.7984	1.7432	1.7755	1.7343	1.7971	1.7859	1.8564
IM_{13}	1.8569	1.8237	1.7848	1.8832	1.8119	1.8016	1.7855	1.9047
IM_{14}	1.7522	1.7241	1.7526	1.8273	1.7513	1.8308	1.8454	1.8671
IM_{15}	1.8962	1.8774	1.7544	1.8648	1.8493	1.8128	1.7894	1.9179

Table 3.2: Saturated pixels (S_p analyses of the illumination channel prior)

Img.	DCP	CNN	CTT	TGV	WT	L_1	FVID	NICP
IM_1	0.0592	0.0612	0.0237	0.0828	0.0834	0.0194	0.0939	0.0182
IM_2	0.0731	0.0524	0.0283	0.0294	0.0402	0.0123	0.0688	0.0108
IM_3	0.2025	0.1563	0.2605	0.2642	0.2748	0.2684	0.1232	0.1218
IM_4	0.2757	0.2736	0.2132	0.2843	0.2788	0.2414	0.2204	0.2121
IM_5	0.1751	0.1815	0.1965	0.1275	0.1369	0.2046	0.2841	0.1263
IM_6	0.2735	0.2316	0.2564	0.1317	0.2913	0.1607	0.2064	0.1305
IM_7	0.1943	0.1565	0.2831	0.2529	0.2017	0.2561	0.2694	0.1553
IM_8	0.2385	0.2636	0.2123	0.1837	0.2673	0.2021	0.2858	0.1825
IM_9	0.2687	0.2774	0.1518	0.1696	0.2365	0.1449	0.1948	0.1437
IM_{10}	0.1796	0.1483	0.2823	0.2689	0.2485	0.1865	0.2139	0.1471
IM_{11}	0.2047	0.1883	0.2056	0.1741	0.1256	0.2736	0.2275	0.1244
IM_{12}	0.1832	0.1595	0.2265	0.2877	0.1767	0.2622	0.1883	0.1583
IM_{13}	0.2385	0.2044	0.1727	0.2441	0.2541	0.2098	0.2168	0.1715
IM_{14}	0.2058	0.2673	0.1799	0.2022	0.2206	0.2205	0.2116	0.1787
IM_{15}	0.2738	0.2177	0.2069	0.1497	0.1396	0.1532	0.1999	0.1384

Focusing only on improving the CG of the image may cause the saturated pixels problem. Therefore, in our experiments, we also performed an analysis for Saturated pixels (Please see Table 3.2). It shows that the designed NICP based desmogging approach has minimum S_p values than competing desmogging models.

The visible edges ratio [77] composes two measures such as ratio of average gradient $(\bar{r})$ and ratio of new visible edges (e).

Table 3.3: New visible edges analyses of the illumination channel prior

Img.	DCP	CNN	CTT	TGV	WT	L_1	FVID	NICP
IM_1	2.2691	2.3926	2.8329	2.2196	1.8705	2.5349	1.7291	3.0546
IM_2	1.9383	1.8068	2.4294	1.9364	2.2461	2.1848	2.8553	2.9877
IM_3	2.6755	1.7986	2.4626	2.7579	2.0099	2.8602	2.2655	3.0819
IM_4	2.0508	2.6467	2.1546	1.8039	2.4014	2.6061	2.7488	2.9705
IM_5	2.5293	2.7936	2.4721	2.8382	2.0049	2.7176	1.9527	3.0599
IM_6	2.3231	2.8811	2.4151	1.8045	1.8666	2.4644	2.2889	3.1028
IM_7	2.2891	2.3192	2.5386	2.4458	2.3945	2.5283	2.4024	2.7597
IM_8	2.5016	2.7598	2.7896	2.1377	1.9336	2.7568	2.5761	3.0113
IM_9	1.7488	2.2603	1.9105	2.7227	2.2826	2.5833	1.9954	2.9444
IM_{10}	2.6873	1.7741	1.9938	2.6121	1.8624	1.2155	2.5628	2.9093
IM_{11}	1.8875	2.4513	1.8276	2.2968	2.3327	2.5899	2.4081	2.8116
IM_{12}	2.7707	2.7062	2.0005	2.2532	1.8999	2.2284	2.6742	2.9924
IM_{13}	2.7526	1.7877	2.3549	2.4814	2.2116	1.9634	2.1882	2.9743
IM_{14}	2.1094	2.7344	1.9087	2.4499	1.8264	1.9453	1.8654	2.9561
IM_{15}	2.1851	2.0108	2.2535	1.8968	1.7555	2.8844	2.1197	3.1061

The maximum values of e proves that proposed NICP based desmogging approach can significantly preserve edges. The edge gradient in a restored image is represented by $\bar{r}$. It is clearly visible that the gradient and texture details are preserved in the restored images.

Tables 3.3 and 3.4 demonstrate that the proposed NICP based desmogging approach provide notably more values of $\bar{r}$ and e than the competing desmogging techniques.

Table 3.5 demonstrates execution time (in seconds) analysis. The proposed NICP based desmogging model is found computationally faster than the existing approaches. Table 3.6 demonstrates smog gradient analyses. It evaluates the effect of smog on the restored smoggy image. It should be minimum.

Table 3.4: Ratio of average gradient analyses of the illumination channel prior

Img.	DCP	CNN	CTT	TGV	WT	L_1	FVID	NICP
IM_1	2.4651	2.4224	2.0728	2.8778	2.0303	2.7225	2.7371	3.0987
IM_2	1.8191	2.0878	1.7578	2.2497	2.1766	2.5478	2.8008	3.0225
IM_3	2.5583	2.0362	2.5776	2.2883	1.9099	2.0826	2.8027	3.0244
IM_4	2.3212	2.4841	2.1634	2.6585	2.5526	1.8614	2.1278	2.8802
IM_5	2.7166	1.7882	2.6319	1.8113	2.6157	2.5614	1.7494	2.9383
IM_6	2.7434	2.6749	2.8224	1.9137	2.5078	2.1719	1.9238	3.0441
IM_7	1.7887	2.3264	2.8446	2.3416	2.0669	2.2724	2.4803	3.0663
IM_8	2.5226	2.5995	2.5775	2.2922	2.7204	2.6308	2.2287	2.9421
IM_9	2.3511	2.6976	2.8197	2.0052	2.8875	2.2737	1.9267	3.1092
IM_{10}	2.0944	1.7905	2.4745	1.9485	2.1756	2.4351	2.1276	2.6962
IM_{11}	1.8163	2.0128	2.4966	2.4754	2.4752	1.7449	2.6511	2.8728
IM_{12}	1.8831	2.6742	1.9155	2.4168	1.7321	2.8328	2.6915	3.0545
IM_{13}	2.6985	2.4977	2.2088	2.8134	2.0898	1.7682	1.8581	3.0351
IM_{14}	1.9462	2.4925	1.8019	2.3184	2.2801	2.4636	1.8711	2.7142
IM_{15}	2.5875	1.8017	2.8206	2.4801	1.9618	2.0122	1.9258	3.0423

Table 3.5: Execution time analyses of the illumination channel prior

Img.	DCP	CNN	CTT	TGV	WT	L_1	FVID	NICP
IM_1	1.6159	1.1703	1.4198	1.1778	1.2347	1.1638	1.3278	1.1626
IM_2	1.2227	1.4718	1.5877	1.5012	1.0257	1.9137	1.8997	1.0238
IM_3	1.1918	1.0884	1.3989	1.4829	1.8833	1.3833	1.9647	1.0872
IM_4	1.6797	1.2384	1.1345	1.8476	1.3522	1.8682	1.0328	1.0316
IM_5	1.8445	1.9237	1.3906	1.0994	1.1695	1.5762	1.2419	1.0982
IM_6	1.4468	1.1944	1.2253	1.5876	1.9786	1.4602	1.1118	1.1106
IM_7	1.2179	1.4843	1.2153	1.3501	1.0342	1.4475	1.8113	1.0337
IM_8	1.6014	1.1551	1.1834	1.8072	1.8831	1.0613	1.9274	1.0598
IM_9	1.5626	1.6213	1.7856	1.6064	1.4838	1.2871	1.4438	1.2859
IM_{10}	1.1787	1.5297	1.2093	1.6512	1.6039	1.2624	1.5966	1.1775
IM_{11}	1.3262	1.6373	1.3874	1.8469	1.0338	1.2128	1.1124	1.0326
IM_{12}	1.3179	1.0518	1.5105	1.8375	1.0383	1.3643	1.9715	1.0371
IM_{13}	1.6286	1.6485	1.0743	1.7719	1.9179	1.7011	1.7431	1.0731
IM_{14}	1.1943	1.2409	1.8611	1.1078	1.6581	1.6101	1.8697	1.1066
IM_{15}	1.9622	1.4577	1.5971	1.7916	1.5699	1.3623	1.6244	1.3611

Table 3.6: Smog gradient analyses of the illumination channel prior

Img.	DCP	CNN	CTT	TGV	WT	L_1	FVID	Proposed
IM_1	2.1235	2.1746	2.1729	2.2982	1.9913	2.2124	2.0693	1.9901
IM_2	1.8208	2.1828	1.8007	2.1174	2.1275	2.0667	2.2639	1.7995
IM_3	1.7413	1.7458	2.2251	1.8532	1.8454	2.0931	2.0243	1.7401
IM_4	2.1756	1.9152	2.0678	2.1196	1.9168	1.9886	1.7305	1.7293
IM_5	1.9048	2.0302	1.7403	2.2329	2.2582	2.2889	1.7461	1.7391
IM_6	1.9465	1.9276	1.8966	1.7693	2.0229	1.7622	1.9229	1.7618
IM_7	1.9373	2.1483	1.8518	2.0195	1.8389	2.2781	2.2921	1.8377
IM_8	1.8367	2.1225	1.7718	2.2753	1.8779	1.9834	2.1937	1.7698
IM_9	1.8101	2.0988	1.9211	1.7789	1.8039	2.0741	2.2337	1.7777
IM_{10}	2.2731	2.2408	2.0976	2.0585	2.2042	2.0019	2.0265	2.0007
IM_{11}	2.2443	1.8433	1.8775	2.2809	2.0446	1.9986	2.2078	1.8421
IM_{12}	2.264	1.7375	1.7881	1.9744	2.2339	2.2418	1.8244	1.7363
IM_{13}	1.9523	2.0727	2.1661	1.7469	1.8726	1.9246	1.7923	1.7457
IM_{14}	2.2924	1.7374	2.1076	2.2774	2.0796	1.9338	2.0374	1.7362
IM_{15}	1.8854	1.9647	2.2828	2.2913	1.8428	2.0621	2.0832	1.8416

Table 3.7: Peak signal to noise ratio (*PSNR*) analyses of the illumination channel prior

Img.	DCP	CNN	CTT	TGV	WT	L_1	FVID	NICP
IM_1	19.4967	25.8678	26.5614	25.3188	24.6994	20.3634	22.9475	27.7831
IM_2	17.9609	19.1804	22.7676	20.8877	20.8544	19.1818	21.4215	23.9893
IM_3	23.9252	17.2231	26.6083	23.4315	17.1802	26.5301	25.7059	27.8364
IM_4	24.2416	17.8427	18.2248	21.2288	19.0258	20.3897	21.3242	25.4633
IM_5	27.2327	18.8738	24.4451	22.5464	20.2524	20.5625	18.5325	28.4544
IM_6	21.3832	27.5935	27.4562	26.9541	23.7733	27.7265	21.6951	28.9482
IM_7	18.5394	26.1746	20.7383	17.1557	18.1453	26.3525	18.8973	27.5742
IM_8	21.5181	23.2813	24.3041	24.2358	22.4541	19.4586	25.5077	26.7294
IM_9	24.5462	23.3565	25.6923	26.3778	20.0001	26.6648	17.8466	27.8857
IM_{10}	19.6222	26.0307	21.3743	18.3251	17.9072	16.8912	22.1692	27.2524
IM_{11}	27.7701	25.3064	18.3383	16.9123	17.5836	19.7853	21.0754	28.9918
IM_{12}	17.2465	26.7442	25.9829	18.0294	18.6671	24.1108	25.5503	27.9659
IM_{13}	21.0985	26.5674	27.4639	21.2924	22.2158	23.6235	19.6316	28.6856
IM_{14}	23.9286	19.7038	16.8995	22.1721	27.3136	25.2591	24.2094	28.5353
IM_{15}	17.6817	26.1174	21.9024	26.3754	23.0086	18.9259	18.3693	27.5971

Peak signal to noise ratio (*PSNR*) needs to be maximized. It is defined as the similarity between the actual smog-free image the restored mage obtained from the desmogging approach. Table 3.7 shows *PSNR* analyses of the proposed and the competing desmogging approaches. The *PSNR* values of the proposed NICP based desmogging model is found to be significantly more than the competing desmogging approaches.

Structural similarity index metric (*SSIM*) needs to be maximized. It is defined as the similarity between the actual smog-free image the restored mage obtained from the desmogging approach. Table 3.8 shows *SSIM* analysis of the proposed and the competitive desmogging approaches. It is found that the designed NICP based desmogging model has significantly more values for *SSIM* than the competitive desmogging approaches.

Table 3.8: Structural similarity index metric (*SSIM*) analyses of the illumination channel prior

Img.	DCP	CNN	CTT	TGV	WT	L_1	FVID	NICP
IM_1	0.8924	0.7568	0.7746	0.8168	0.7962	0.8275	0.8994	0.9011
IM_2	0.8297	0.8432	0.8086	0.8438	0.8507	0.7544	0.7702	0.8524
IM_3	0.7686	0.7433	0.8279	0.7233	0.7326	0.8944	0.8482	0.8961
IM_4	0.8418	0.7861	0.7309	0.8592	0.8808	0.8892	0.8304	0.8909
IM_5	0.8321	0.8207	0.8796	0.8591	0.8174	0.8323	0.8238	0.8813
IM_6	0.7772	0.7743	0.8521	0.7868	0.8143	0.8253	0.8532	0.8549
IM_7	0.8806	0.8471	0.8944	0.8479	0.7978	0.7973	0.7738	0.8957
IM_8	0.7422	0.7695	0.7964	0.7399	0.8691	0.8496	0.7291	0.8708
IM_9	0.7517	0.7673	0.7456	0.8344	0.8673	0.8424	0.8353	0.8687
IM_{10}	0.7273	0.8223	0.8005	0.7715	0.7746	0.7255	0.8433	0.8957
IM_{11}	0.7488	0.7677	0.7873	0.8169	0.8307	0.8614	0.8847	0.8864
IM_{12}	0.8434	0.7603	0.7716	0.8893	0.8879	0.8923	0.7838	0.8943
IM_{13}	0.7429	0.7582	0.7249	0.8789	0.8958	0.8983	0.7416	0.9154
IM_{14}	0.8379	0.8002	0.7263	0.8978	0.8986	0.8188	0.8671	0.9003
IM_{15}	0.8716	0.8203	0.8422	0.7317	0.8127	0.7536	0.8074	0.8733

From Tables 3.1 to 3.8, it has been found that the NICP outperforms the competitive desmogging models in terms of contrast gain, new visible edges, average gradient, peak signal to noise ratio, and structural similarity index metric by 1.2883%, 1.5392%, 0.8271%, 0.8928% and 1.2813%, respectively. In comparison with the competitive models, NICP also minimizes the smog gradient, saturated pixels, and execution time by 0.8282%, 0.7291% and 1.1428%, respectively.

3.4 Summary

An efficient desmogging approach has been proposed in this chapter. The proposed approach uses two new concepts namely illumination channel prior and refined trilateral filter. The dynamic threshold is used to reduce the color distortion rate. The experimental results illustrate that the proposed approach can mention the colors of a smog-free image. Based on the results obtained, we can conclude that the proposed approach can be applied to real-time applications.

The work leads to new and exciting future applications and quests. Firstly, supervised learning based approaches can be applied for the estimation of transmission map and atmospheric veil. Secondly, the desmogging models can be integrated with machine learning models to improve the performance significantly. It is also useful to deploy the applicability of the proposed approach for different computer vision problems such as underwater image analysis, outdoor video surveillance, and remote sensing imaging, etc.

Chapter 4

Image desmogging using information gain based bilateral filter

Outline

Many visibility restoration models approaches have been designed to restore smog from still images. But, removing the smog from images is defined as an ill-posed problem. Therefore, a novel desmogging approach is designed. Initially, gradient channel prior is used to estimate the optical information of smoggy images. Thereafter, an information gain based filter is designed to improve the transmission map. The smog-free image is then computed using an improved restoration model.

4.1 Background

Smog degrades the optical information of the actual scene, therefore, computed images become useless for various imaging systems [125]. Therefore, removing the smog from images turn out to be a challenging issue. To restore smoggy images, approximation of transmission map and atmospheric viel is required [126]. To approximate these maps, many researchers have used various channel priors to compute the depth information of smoggy images [127, 128].

A smog formation model can be mathematically defined as:

$$\begin{aligned} S_i(i) &= t_x(i)S_r(i) + (1 - t_x(i))A_l, \\ t_x(i) &= e^{-\beta d(i)}. \end{aligned} \tag{4.1}$$

Here, $S_i(i)$ represents the captured smoggy image. $S_r(i)$ demonstrates the actual scene radiance. A_l is defined as atmospheric light. $t_x(i)$ demonstrates the transmission map. $d(i)$ gives the difference between camera and object [66]. The main objective of single image desmogging is to restore $S_r(i)$, when only $S_i(i)$ is given in prior [129, 130]. Therefore, an efficient approximation of t_x and A_l becomes a challenging issue.

Ge et al. designed a desmogging model to approximate atmospheric light by using an infinite sky regions [85]. Li et al. designed a change of detail prior for visibility restoration of smoggy images. It considers multiple scattering model to estimate the depth information [89]. But, [85] and [89] are not able to handle sky-region issues [1, 116, 131].

Ding et al. designed a L2-norm based desmogging model. Mean vector L2-norm of sample window has been used to estimate the optical information of smoggy images [87]. But, L2-Norm suffer from gradient reversal artifacts issue. Li et al. used a weighted guided image filter to refine the transmission map. It refines transmission map quickly [88]. But, this approach performs poorly whenever objects are inherently similart to each other [132, 133].

He et al. utilized Local surface analysis (LSA) to restore the visibility of images. Although, it outpeforms existing approaches, but still suffer from images with large smog gradient [134, 66]. Ma and Zhang implemented a Saturated aware Dark channel prior (SDCP) to reduce the saturation pixels problem [135]. But, this technqiue is not so-effective against images with texture inormation. Singh and Kumare implemented a Gradient channel prior (GCP) for successfully restore the smoggy images. Although, it has demonstrated good results for texture images, but, not so-effective when objects in input images are inherently similar with the background [136].

Chang et al. designed a novel External gradient prior (EGP) to restore the smog from images. It is able to achieve significant results, but, not so-effective for images with huge smog gradient [137]. Image filtering process is also becomes challenging in for desmogging model [126, 138]. Image filtering approaches are utilized to improve computed transmission map [129].

Therefore, it has been found that the dark channel prior is found to be one of the popular channel prior. It has been widely accepted as a visibility restoration model. However, it is not so-effective for images having brighter segments i.e., sky-region issue or image contain high density of smog. Also, if images contain texture information [139, 140].

A novel desmogging model is designed by using gradient channel prior and information gain based bilateral filter. Gradient channel prior is found to be effective for images contain high density of smog, brighter segments, and/or also texture information. However, computed transmission map using gradient channel prior is not smooth and prone to some noise. Therefore, we have designed and applied a novel information gain based bilateral filter on computed transmission map. Finally, an improved restoration model is applied to restore the smoggy images. To validate the designed approach, comparison of the designed approach is drawn with 4 visibility restoration approaches and the designed approach upon benchmark smoggy images.

4.2 Information gain based bilateral filter

4.2.1 Gradient channel prior

The gradient channel prior can be defined as a statistical property of image. It defines that in local window of smog-free images, the gradient pixel across RGB channels approaches toward 0. It is mathematically defined as:

$$S_r^{\Delta}(i) = \underset{c\in\{r,g,b\}}{\Delta}\big(\underset{j\in\Omega(i)}{\Delta}(S_r^c(j))\big), \tag{4.2}$$

Here, $\Omega(i)$ defines patch centered at i.

Let A_l is known. Then, the transmission in a patch is defined using constant $\tilde{t}(i)$. A minimum operation can be applied across all channels and pixels in Eq. (4.1) and obtain an estimation for the transmittance [141]:

$$\tilde{t}(i) = 1 - \delta \cdot \underset{c}{\Delta}\left(\underset{j\in\Omega(i)}{\Delta}\left(\frac{S_i^c(j)}{A^c}\right)\right), \tag{4.3}$$

Here $\delta = 0.89$ is used to prevent over-restoration of smoggy images. Let $S_i/A_l \to 1$, therefore, $\tilde{t}(i) \to 0$. Thus, the computed transmission map requires filtering.

4.2.2 Transmission map refinement

In this chapter, we have designed a novel information gain based bilateral filter to refine the transmission map. Initially, we will recall bilateral filter. Thereafter, we will discuss the designed filter.

Figure 4.1 shows the designed information gain based bilateral filter based desmogging model.

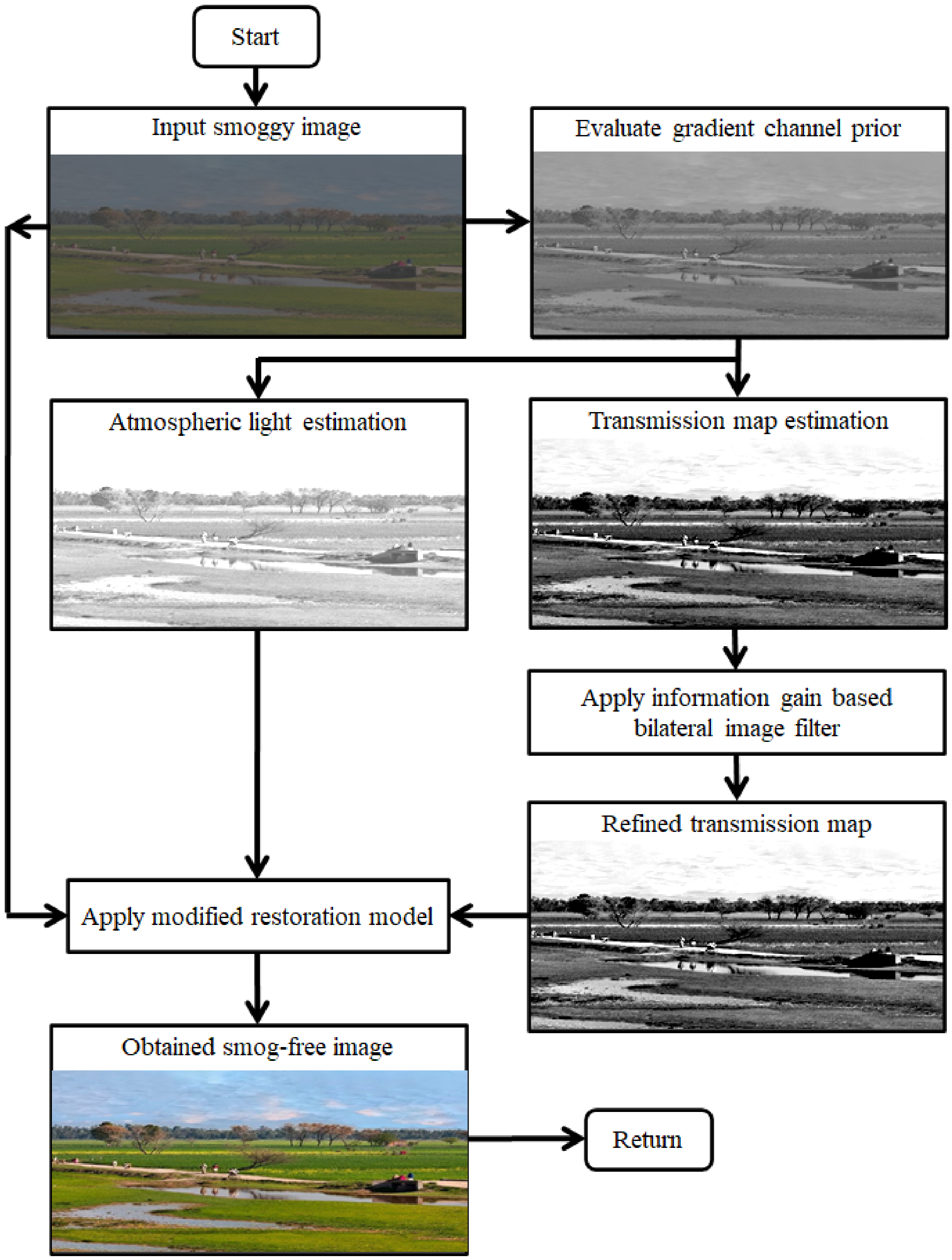

Figure 4.1: Flowchart of the proposed information gain with bilateral filter based desmogging model

Bilateral fitler is a well-known spatially-invariant Gaussian kernel based image filter. The range kernel evaluates the pixels in patches and evaluate weighted average to replace the value of central pixel. Mathematically, bilateral filter is computed as:

$$\hat{I}(i) = \left\{ \frac{I(i)}{\theta_I}, \frac{i}{\theta_i} \right\}, \tag{4.4}$$

Here, θ_i demonstrates the constant conduction coefficient. θ_I is a range kernel. After deriving the Eq. (4.4), the filtering process can be redefined as:

$$O(I(i)) = I(i) + R\left(\hat{I}(i), \hat{I}(\vec{\chi})\right), \tag{4.5}$$

Here, $\vec{\chi}$ demonstrates the coordinate of sibling pixels when patch is centered at i. $R\left(\hat{I}(i), \hat{I}(\vec{\chi})\right)$ can be estimated as:

$$R\left(\hat{I}(i), \hat{I}(\vec{\chi})\right) = \frac{\sum_{\vec{\chi}} \hat{w}(\vec{x}, \vec{\chi})\,(I(\vec{\chi}) - I(i))}{\sum_{\vec{\chi}} \hat{w}(\vec{x}, \vec{\chi})}, \tag{4.6}$$

Here, $(I(\vec{\chi}) - I(i))$ defines as difference between intensity values of sibling pixels. The kernel can be redefined as:

$$\hat{w}(\vec{x}, \vec{\chi}) = \exp\left\{-\frac{1}{2}\left\|\hat{I}(i) - \hat{I}(\vec{\chi})\right\|^2\right\} \tag{4.7}$$

If we normalized the weights, $R\left(\hat{I}(i), \hat{I}(\vec{\chi})\right)$ can be demonstrated as approximation of local intensity variation.

However, the bilateral filter refines each and every pixel. Therefore, we have designed a selective bilateral filter by using information gain. It states that bilateral filter will change the values of given pixel if and only if it has significant information gain with all its sibling pixels. We have has used 0.1 as a threshold value to achieve the selective bilateral filter.

4.2.3 Visibility restoration

Finally, from Eq. (4.1), smog free image can be restored as:

$$S_r(i) = \frac{S_i(i) - A_l}{\max(t_\theta(i), l_b)} + A_l, \tag{4.8}$$

Here, l_b, represents the lower bound which states how much smog can be allowed in the restored image. We have considered l_b because if we completely restores the image then it may seems like an artificial image.

4.3 Performance analysis of information gain based bilateral filter

Benchmark smoggy images have been considered for experimental analyses. The comparisons are drawn with 4 well-known visibility restoration approaches.

4.3.1 Visual analyses of information gain based bilateral filter

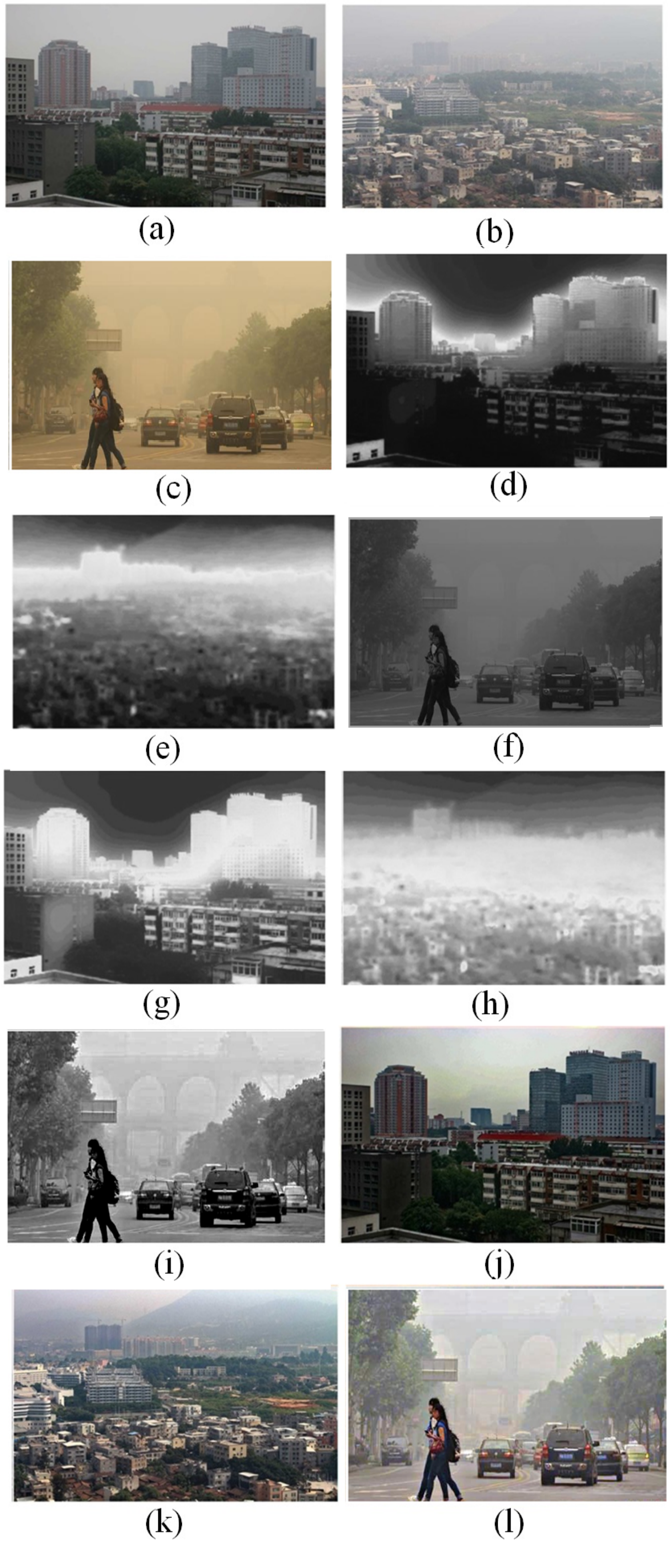

Figure 4.2: Gradient map analyses of the proposed information gain with bilateral filter based desmogging model

Figure 4.2 demonstrates gradient map analysis of smoggy images. Figures 4.2 (a), (b) and (c) demonstrate the input smoggy images. The estimated depth maps computed using gradient channel prior are demonstrated in Figures 4.2 (d), (e) and (f). The refined transmission maps are demonstrated in Figures 4.2 (g), (h) and (i). The corresponding restored images are demonstrated in Figures 4.2 (j), (k) and (l). Thus, Figure 4.2 proves that the restored images computed using the designed approach obtains more natural results with good spectral and spatial information.

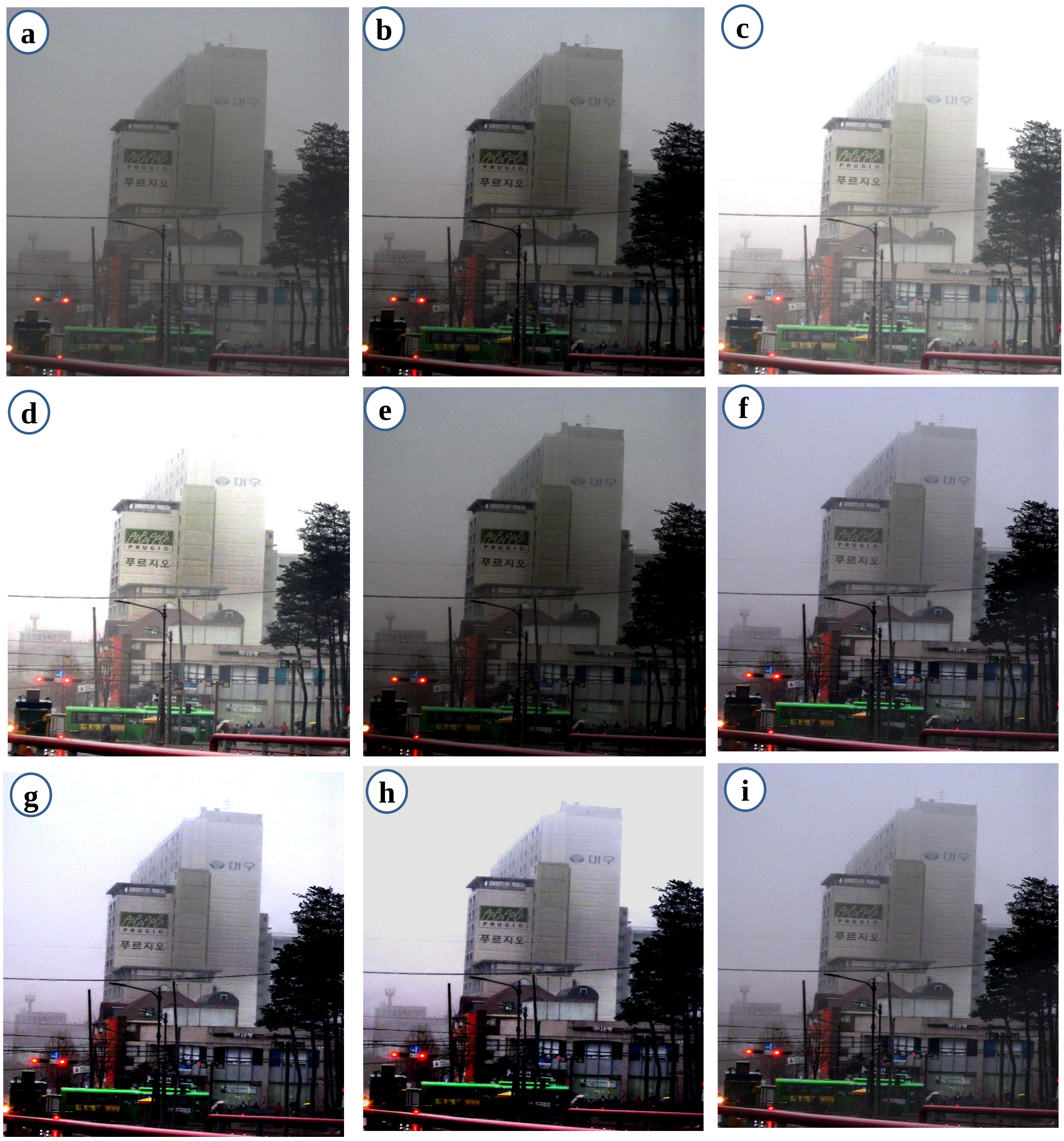

Figure 4.3: Results of desmogging models (a) Input image, (b) DCP [6], (c) CNN [7], (d) CTT [8], (e) TGV [9], (f) WT [10], (g) L_1 norm [11], (h) FVID [12] and (i) Proposed NGCP model.

Desmogging results in Figures 4.3 4.4, and 4.5 have demonstrated the benefits of the proposed desmogging model. DCP [27] and CTT [8] contain sky region and abundant textures contain headlights that are essentially different from the atmospheric light. It can be found that the approaches are not efficient to remove the smog for images effected from large smog gradient.

CNN [7] and TGV [9] tend to oversmooth fine image details and degrade image quality especially for images which are effected from large smog gradient. WT [10], L_1 norm [11], and FVID [12] show remarkable good results compared to the other approaches. However, these approaches are not capable of preserving texture information of the restored smoggy images. The proposed approach does not suffer from edge, color and texture distortion issues.

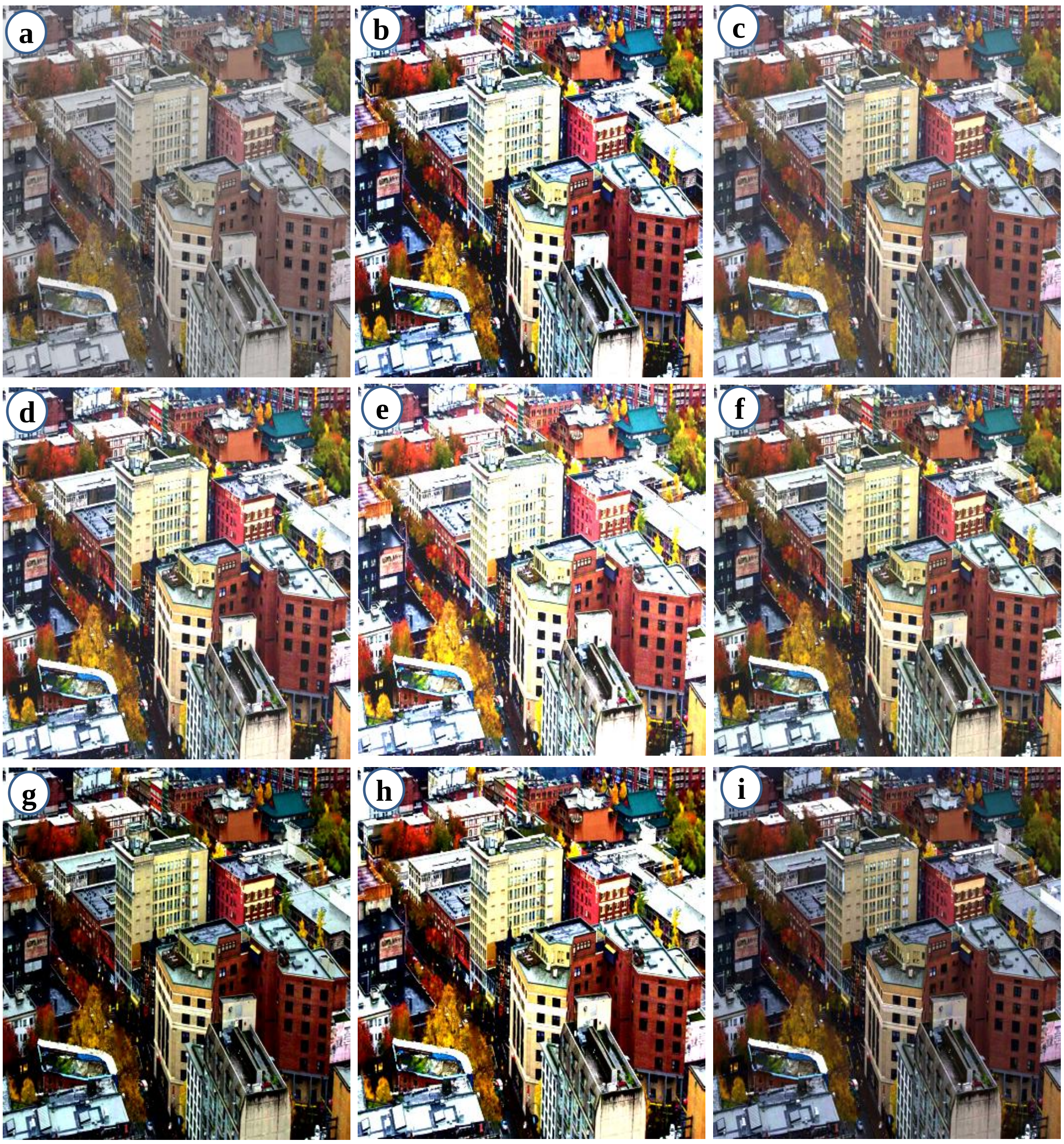

Figure 4.4: Results of desmogging models (a) Input image, (b) DCP [6], (c) CNN [7], (d) CTT [8], (e) TGV [9], (f) WT [10], (g) L_1 norm [11], (h) FVID [12] and (i) Proposed NGCP based desmogging model.

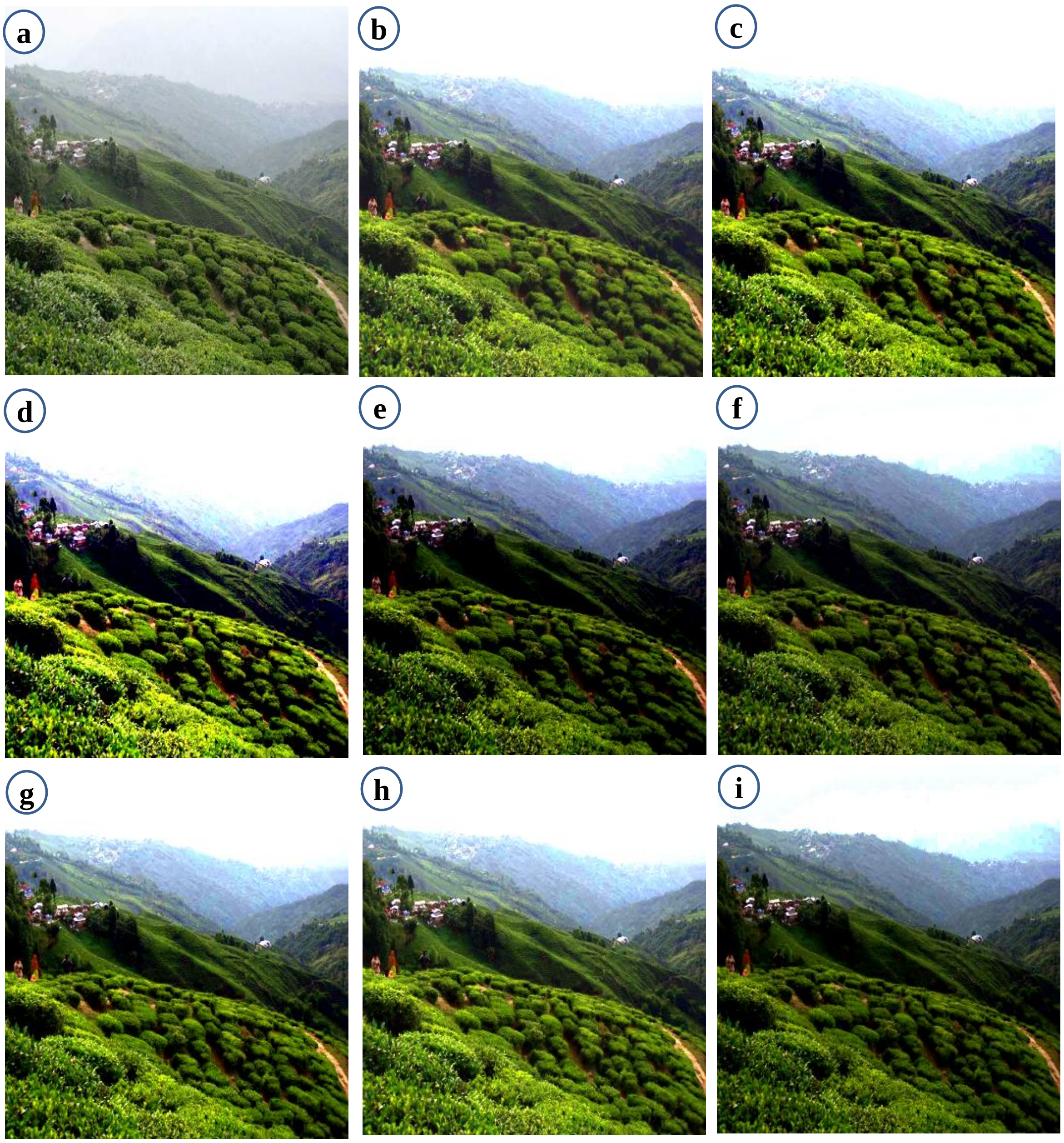

Figure 4.5: Results of desmogging models (a) Input image, (b) DCP [6], (c) CNN [7], (d) CTT [8], (e) TGV [9], (f) WT [10], (g) L_1 norm [11], (h) FVID [12] and (i) Proposed NGCP based desmogging model.

It has been found that the designed approach provides more significant spatial and spectral information in comparison with the existing visibility restoration approaches. Additionally, it has demonstrated that the designed approach introduces lesser gradient reversal and halo artifacts as compared to the existing restoration approaches.

4.3.2 Quantitative analyses of information gain based bilateral filter

The designed desmogging model is compared to the well-known existing techniques while considering various performance measures like percentage of saturated pixels (S_p), smog gradient, contrast gain (CG), visible edges, execution time (ET), structural similarity index metric, and peak signal to noise ratio .

Table 4.1 demonstrates CG analysis. It has been observed that the designed NGCP based desmogging model has notable CG values than competitive desmogging approaches.

Table 4.1: Contrast gain analyses of the proposed information gain with bilateral filter based desmogging model

Img.	DCP	CNN	CTT	TGV	WT	L_1	FVID	NGCP
IM_1	1.8807	1.8683	1.8507	1.8003	1.7674	1.8632	1.7454	1.9024
IM_2	1.7825	1.8536	1.7888	1.8127	1.7524	1.7765	1.8478	1.8753
IM_3	1.7689	1.7743	1.8414	1.8769	1.7277	1.7499	1.7466	1.8986
IM_4	1.8622	1.8159	1.8985	1.7387	1.7705	1.7962	1.8916	1.9202
IM_5	1.8784	1.8155	1.7322	1.7906	1.7603	1.7355	1.7464	1.9001
IM_6	1.8737	1.7974	1.7666	1.8519	1.8402	1.8196	1.8085	1.8954
IM_7	1.7643	1.7903	1.7536	1.7541	1.7526	1.8125	1.8068	1.8342
IM_8	1.8358	1.7628	1.8353	1.7642	1.7492	1.7955	1.7833	1.8575
IM_9	1.8014	1.8902	1.7568	1.8108	1.8122	1.8958	1.7761	1.9175
IM_{10}	1.7902	1.8826	1.8134	1.7893	1.8754	1.7906	1.7342	1.9043
IM_{11}	1.7887	1.7438	1.7993	1.8344	1.7368	1.8706	1.8142	1.8923
IM_{12}	1.8898	1.7752	1.7998	1.8937	1.7885	1.8339	1.8424	1.9154
IM_{13}	1.8672	1.7772	1.8352	1.7241	1.7812	1.8444	1.8188	1.8889
IM_{14}	1.8867	1.7807	1.7643	1.7985	1.7733	1.8697	1.7377	1.9084
IM_{15}	1.8235	1.8363	1.8873	1.8434	1.7847	1.7542	1.8908	1.9125

Table 4.2 reveals that the proposed NGCP based desmogging model has minimum S_p values than competing restoration techniques.

Table 4.2: Saturated pixels (S_p) analyses of the proposed information gain with bilateral filter based desmogging model

Img.	DCP	CNN	CTT	TGV	WT	L_1	FVID	NGCP
IM_1	0.0396	0.0152	0.0398	0.0336	0.0517	0.0779	0.0188	0.0145
IM_2	0.0332	0.0172	0.0569	0.0776	0.0695	0.0211	0.0441	0.0158
IM_3	0.0835	0.2358	0.2031	0.2626	0.1305	0.2014	0.1368	0.0823
IM_4	0.0657	0.1728	0.1454	0.2508	0.2078	0.2302	0.2054	0.0645
IM_5	0.0554	0.2083	0.1352	0.2299	0.2619	0.2667	0.2618	0.0542
IM_6	0.0278	0.2356	0.2872	0.2077	0.2328	0.1657	0.2172	0.0266
IM_7	0.0714	0.1924	0.2834	0.2567	0.1424	0.2769	0.1315	0.0702
IM_8	0.0508	0.1944	0.2319	0.1605	0.1557	0.1399	0.187	0.0496
IM_9	0.0471	0.1567	0.2707	0.1332	0.2006	0.1879	0.2265	0.0459
IM_{10}	0.0864	0.1796	0.2677	0.2518	0.1372	0.2699	0.1724	0.0852
IM_{11}	0.0632	0.1417	0.1237	0.1792	0.2895	0.1545	0.1485	0.0624
IM_{12}	0.0151	0.2895	0.1587	0.1697	0.1931	0.2088	0.2455	0.0139
IM_{13}	0.0416	0.2581	0.2377	0.1992	0.2818	0.1932	0.1958	0.0404
IM_{14}	0.0564	0.1937	0.1439	0.2276	0.1822	0.2472	0.1238	0.0552
IM_{15}	0.0733	0.1308	0.2792	0.1943	0.1711	0.1618	0.1529	0.0721

Table 4.3: New visible edges analyses of the proposed information gain with bilateral filter based desmogging model

Img.	DCP	CNN	CTT	TGV	WT	L_1	FVID	NGCP
IM_1	2.0415	2.5582	2.8926	2.8944	2.7428	2.7339	2.5273	3.1161
IM_2	2.4182	1.8141	2.7945	2.3007	2.1626	2.0042	2.8182	3.0399
IM_3	2.8981	2.2719	1.9588	2.2765	1.7237	2.4473	2.2722	3.1198
IM_4	1.9863	2.5957	2.4396	2.5064	2.0301	2.0161	2.1918	2.8174
IM_5	2.0713	2.1785	1.8322	1.9146	2.3961	1.7588	2.5957	2.8174
IM_6	2.6851	2.0124	2.5936	1.8566	2.3779	2.5248	2.7927	3.0144
IM_7	1.7437	2.1035	2.7544	1.9913	2.0751	2.1306	2.0156	2.9761
IM_8	2.1723	2.8471	2.0824	2.7857	1.8929	2.1453	1.7957	3.0688
IM_9	2.1182	2.5655	2.0107	1.9735	2.4797	2.1908	2.1806	2.7872
IM_{10}	2.1801	2.3551	2.1429	1.7657	2.8405	1.7852	1.8437	3.0622
IM_{11}	1.8997	1.9425	1.7723	1.9559	1.9967	1.7569	1.8448	2.2184
IM_{12}	2.5858	2.6071	2.6327	2.6613	1.7377	2.6515	2.8852	3.1069
IM_{13}	1.9731	1.9439	2.2386	2.0413	2.6833	2.0861	1.9183	2.9059
IM_{14}	2.8671	2.5818	1.7657	2.5461	2.6899	1.8332	2.0963	3.0888
IM_{15}	2.4713	2.2697	1.7345	1.8815	2.1696	2.7477	2.1396	2.9694

Tables 4.3 and 4.4 demonstrate that the proposed NGCP based desmogging technique has notably more values of $\bar{r}$ and e than existing restoration techniques.

Table 4.4: Ratio of average gradient analyses of the proposed information gain with bilateral filter based desmogging model

Img.	DCP	CNN	CTT	TGV	WT	L_1	FVID	NGCP
IM_1	1.8134	2.6248	2.1904	2.6222	2.1658	2.7258	2.1134	2.9475
IM_2	2.5226	1.7691	2.0723	2.1283	2.6184	2.0666	2.8167	3.0384
IM_3	1.7539	2.3621	2.2279	2.3122	2.3233	1.9227	2.0539	2.5838
IM_4	2.2986	2.5617	2.2836	1.7657	1.8494	2.6002	2.3275	2.8219
IM_5	2.7684	2.8464	2.1402	2.8414	1.7303	2.3961	2.4124	3.0681
IM_6	2.7407	1.9135	1.7282	2.2457	1.9422	2.7452	2.1703	2.9669
IM_7	1.9927	2.2743	2.5568	2.4504	2.3906	2.3615	2.7256	2.9473
IM_8	2.4469	2.1999	1.9042	1.8402	2.7522	2.6418	2.7539	2.9756
IM_9	2.2855	2.3527	2.1257	2.2185	2.8017	2.4132	2.7476	3.0234
IM_{10}	1.9872	2.7178	2.1763	1.9391	2.3772	2.0128	2.1279	2.9395
IM_{11}	2.2301	2.2861	1.8692	1.9205	2.5546	1.8956	1.9341	2.7763
IM_{12}	2.5327	2.1642	2.2455	2.7624	2.7799	1.8273	2.2425	3.0016
IM_{13}	2.1484	2.1493	2.5719	2.0841	1.9628	1.8125	2.3361	2.7936
IM_{14}	2.4881	2.7677	2.1813	1.8909	2.6928	1.7264	2.2499	2.9894
IM_{15}	2.0199	1.8425	2.6932	2.3899	2.8555	1.7488	2.5424	3.0772

Table 4.5 demonstrates execution time (in seconds) analysis. It can be found that the designed NGCP based desmogging approach is computationally faster than the existing approaches.

Table 4.5: Execution time analyses of the proposed information gain with bilateral filter based desmogging model

Img.	DCP	CNN	CTT	TGV	WT	L_1	FVID	NGCP
IM_1	1.3236	1.4551	1.2357	1.5833	1.8672	1.2694	1.4615	1.2345
IM_2	1.9139	1.3972	1.8787	1.5387	1.1987	1.6033	1.1859	1.1847
IM_3	1.1675	1.0375	1.1812	1.1667	1.2859	1.6794	1.1671	1.0363
IM_4	1.1894	1.9465	1.9889	1.4675	1.5353	1.8388	1.0322	1.0317
IM_5	1.4731	1.7385	1.0879	1.5394	1.5843	1.6872	1.2862	1.0867
IM_6	1.7857	1.9363	1.3632	1.1071	1.3404	1.0351	1.7226	1.0339
IM_7	1.1929	1.7691	1.2035	1.6354	1.2369	1.8565	1.9677	1.1917
IM_8	1.0546	1.2886	1.9848	1.9462	1.4057	1.8323	1.6474	1.0534
IM_9	1.9923	1.6349	1.0712	1.4351	1.0474	1.1575	1.1794	1.0462
IM_{10}	1.7371	1.6748	1.8675	1.0379	1.3305	1.5901	1.9355	1.0367
IM_{11}	1.3231	1.3072	1.1466	1.7661	1.7472	1.5728	1.3045	1.1454
IM_{12}	1.3508	1.6435	1.2047	1.4904	1.4468	1.1086	1.1891	1.1074
IM_{13}	1.8763	1.4463	1.9791	1.7968	1.5654	1.5576	1.1067	1.1055
IM_{14}	1.5111	1.8878	1.1631	1.9684	1.7113	1.1418	1.1267	1.1255
IM_{15}	1.1975	1.8825	1.7349	1.2722	1.2234	1.5273	1.6245	1.1963

Table 4.6: Smog gradient analyses of the proposed information gain with bilateral filter based desmogging model

Img.	DCP	CNN	CTT	TGV	WT	L_1	FVID	Proposed
IM_1	2.0392	2.2865	1.7521	2.2553	1.7777	2.1373	2.1452	1.7509
IM_2	1.7761	2.2236	2.0991	2.2632	1.8965	1.8836	2.1233	1.7749
IM_3	2.1382	2.1332	1.9721	1.8864	1.7276	1.7888	2.1013	1.7264
IM_4	2.1293	1.7624	2.0108	1.8697	2.1373	1.8579	1.9716	1.7612
IM_5	2.0238	2.1791	2.1148	1.9386	1.9976	2.0498	2.1965	1.9374
IM_6	2.1192	1.9618	1.8699	2.2013	2.1969	1.8991	2.0984	1.8687
IM_7	1.7239	1.9157	1.7544	1.9754	1.7346	2.0192	1.9546	1.7227
IM_8	2.0248	1.9933	2.1714	2.1275	2.1709	1.7423	1.7419	1.7407
IM_9	1.9842	2.2328	1.7368	1.7815	2.2741	2.0355	2.0799	1.7356
IM_{10}	2.1369	2.2613	1.8693	2.1306	2.1246	2.2079	1.9249	1.8678
IM_{11}	1.9996	1.9508	1.8916	1.9784	1.7356	2.0541	1.7503	1.7344
IM_{12}	1.8053	1.7333	1.7906	2.2143	1.7937	1.9684	1.8566	1.7321
IM_{13}	1.8796	2.0368	1.7569	1.7858	1.9348	1.8707	2.1618	1.7557
IM_{14}	2.0495	1.7383	1.7505	2.0032	2.2089	1.8081	2.0199	1.7371
IM_{15}	1.9628	1.9721	2.1311	2.1853	2.2128	1.9848	2.2754	1.9616

Table 4.6 demonstrates smog gradient analyses. It can be observed that the designed approach is significantly faster than the competitive approaches.

Table 4.7 shows *PSNR* analyses of the designed and the existing desmogging models. It is found that the designed NGCP based desmogging technique has significant *PSNR* values than the existing desmogging approaches.

Table 4.7: Peak signal to noise ratio (*PSNR*) analyses of the proposed information gain with bilateral filter based desmogging model

Img.	DCP	CNN	CTT	TGV	WT	L_1	FVID	NGCP
IM_1	21.2316	17.2917	22.4035	23.5759	23.2901	18.5268	17.0875	24.7976
IM_2	25.3084	17.7327	27.6439	19.5342	24.6107	19.8689	25.8095	28.8656
IM_3	20.1986	20.7476	17.4901	20.4892	16.8533	21.5116	26.1205	27.3422
IM_4	26.8931	25.88	21.9282	25.9135	18.1848	25.115	27.1509	28.3726
IM_5	21.125	24.4355	17.2777	27.1253	25.9638	27.5712	18.2023	28.7929
IM_6	19.0042	25.2068	21.4021	21.0135	20.0635	16.8616	22.3635	26.4285
IM_7	23.3863	27.2402	20.3578	26.2598	17.0738	26.3416	22.0908	28.4619
IM_8	20.9865	24.042	22.8413	17.2838	23.3211	24.6901	19.0626	25.9118
IM_9	20.9426	26.1495	24.1349	24.1932	20.4048	26.056	20.8845	27.3712
IM_{10}	26.1722	17.3141	24.4068	23.1816	18.9491	26.8676	17.0198	28.0893
IM_{11}	19.7411	17.9029	19.8054	25.8732	25.4225	27.7896	17.1378	29.0113
IM_{12}	17.1328	19.6373	26.679	17.6296	16.8633	25.1239	17.0042	27.9007
IM_{13}	21.4174	21.0845	20.7443	16.8599	22.0576	24.3061	21.9045	25.5278
IM_{14}	27.7001	18.8313	25.0399	17.919	26.6615	23.1649	17.8818	28.9218
IM_{15}	21.3484	20.0144	22.4383	19.8097	22.0131	20.6223	17.7371	23.66

Table 4.8 shows *SSIM* analyses of the designed and the competitive desmogging approaches. It is observed that the designed NGCP based desmogging model has significant *SSIM* values than the competitive desmogging approaches.

From Tables 4.1 to 4.8, it has been found that the proposed model outperforms the competitive models in terms of contrast gain, new visible edges, average gradient, peak signal to noise ratio, and structural similarity index metric by 1.8373%, 1.9379%, 1.9838%, 1.9382% and 1.8272%, respectively. Compared to the existing models, NGCP also minimizes the smog gradient, saturated pixels, and execution time by 1.2279%, 1.8273% and 0.9823%, respectively.

Table 4.8: Structural similarity index metric ($SSIM$) analyses of the proposed information gain with bilateral filter based desmogging model

Img.	DCP	CNN	CTT	TGV	WT	L_1	FVID	NGCP
IM_1	0.8243	0.8672	0.7547	0.7367	0.7725	0.8502	0.7953	0.8689
IM_2	0.8957	0.8887	0.8106	0.7472	0.7775	0.8989	0.8496	0.8997
IM_3	0.7672	0.7507	0.8328	0.8619	0.7469	0.8238	0.7878	0.8636
IM_4	0.7858	0.7446	0.8303	0.7359	0.8826	0.7752	0.7618	0.8843
IM_5	0.8237	0.7861	0.8499	0.7293	0.7813	0.7823	0.8168	0.8516
IM_6	0.8096	0.8758	0.8605	0.8076	0.7902	0.7276	0.8963	0.8977
IM_7	0.8264	0.7333	0.8421	0.7379	0.7392	0.7474	0.7956	0.8438
IM_8	0.8209	0.8676	0.8575	0.8734	0.7969	0.7519	0.8599	0.8751
IM_9	0.7733	0.7542	0.8021	0.7668	0.7977	0.7777	0.7384	0.8038
IM_{10}	0.8974	0.7592	0.8605	0.8743	0.8743	0.7518	0.8676	0.8991
IM_{11}	0.7492	0.7853	0.7587	0.8856	0.7764	0.7472	0.8593	0.8873
IM_{12}	0.8287	0.8825	0.8622	0.7668	0.8315	0.8765	0.8895	0.8912
IM_{13}	0.8065	0.7897	0.7851	0.8883	0.8986	0.8294	0.7534	0.9003
IM_{14}	0.8541	0.8293	0.8781	0.7395	0.8274	0.8535	0.8188	0.8798
IM_{15}	0.7301	0.8083	0.8524	0.8665	0.8586	0.8699	0.7265	0.8716

4.4 Summary

A novel smog removal approach was designed for still smoggy images. Initially, gradient channel prior has been utilized to approximate the optical information of smoggy images. Thereafter, an information gain based bilateral filter was utilized to improve the transmission map. The smog free image is then obtained by implementing an improved restoration model.

Extensive experiments have been carried out by considering benchmark smoggy images. Performance analysis have proved that the designed approach outperforms the existing visibility restoration approaches. Although, the designed approach has obtained significant results, but, it can be improved further by efficiently tuning the hyperparameters of the designed approach.

Chapter 5

Desmogging using oblique gradient profile prior and variational minimization

Outline

In this chapter, a novel transmission map estimation is developed by deploying weighted integrated transmission maps obtained from foreground and sky regions. Additionally, the further refinement of the transmission map is done by using an integrated variational regularized model with hybrid constraints. However, the suggested approach suffers from the hyper-parameters tuning issue. Therefore, in this chapter, a Non-dominated sorting genetic algorithm (NSGA) is also used to tune the hyper-parameters of the proposed approach.

5.1 Background

Images captured in poor environmental situations such as haze, fog, haze, smog, etc. suffer from poor visibility issue. The optical imaging model is formulated as a linear combination of an actual scene radiance, airlight and the transmission map. It is mathematically defined as [27]:

$$\alpha(\delta) = \kappa(\delta)\,\mu(\delta) + (1 - \mu(\delta))\,\nu, \tag{5.1}$$

Here, κ denotes the actual object radiance and α represents the obtained smoggy image. μ and ν represents the transmission map and global atmospheric light, respectively. The foremost function of desmogging method is to restore κ from α. Though, atmospheric light (ν) and transmission (μ) are unknown.

To evaluate the atmospheric light (ν) and transmission (μ), many desmogging models have been designed so far. Many authors have designed multiple-images based desmogging models [142]. These models demand additional information of input images in prior [143, 144, 145]. However, in real-time desmogging it is hard to obtain additional information of the given scene [146, 147].

Guo et al. [148] implemented a fusion based desmogging model. Yoon [149] designed an adaptive variation minimization based desmogging model. But, [148] and [149] suffers from poor computational speed. [119].

Recently, learning based desmogging models such as DesmogNet [45] gains much attention of the researchers. Jiang et al. [101] implemented a regression based model to evaluate depth information. Nishino et al. [150] implemented a Bayesian probabilistic model to evaluate transmission map. The performance of these models depends on the volume and variety of training data sets. However, guaranteeing high-quality desmogging results following unusual imaging conditions becomes a challenging task. Also, these approaches suffer from lesser computational speed issues.

The main objectives of this chapter is to suppress artifacts for restoration of radiometric detail and restore visibility of smoggy outdoor images. Two novel concepts, i.e., integrated variational regularized model and integrated transmission map estimation with hybrid constraints are presented in the proposed desmogging model. Finally, to tune hyper-parameters of the proposed approach, a Non-dominated sorting genetic algorithm (NSGA) is also used.

The performance of proposed desmogging model is evaluated on outdoor images with respect to some well-known visibility restoration performance measures. The comparative analyses with competitive desmogging approaches are also drawn.

5.2 Proposed oblique gradient profile prior and variational minimization based desmogging model

This section provides a mathematical formulation of the designed desmogging model. Initially, we try to accurately estimate the transmission map. Thereafter, transmission map refinement is considered, Finally, the restored image is obtained using restoration model.

5.2.1 Transmission map estimation

Natural images generally contain a background (i.e., sky) and foreground regions. The transmission map in foreground regions is obtained using Dark channel prior (DCP) [27] and Gradient profile prior (GPP) [136] assumption in this chapter. But, DCP and GPP suffer from various artifacts when there exists large sky regions. The oblique gradient profile prior (OGPP) has an ability to evaluate transmission map in sky regions.

Oblique gradient prior

Singh and Kumar [151] designed an OGPP of a smoggy image (α). An OGPP composes magnitude and direction information of α. It is evaluated as:

$$\nabla \alpha \kappa = \begin{pmatrix} \psi_\gamma \\ \psi_\rho \end{pmatrix} = \begin{pmatrix} \partial \alpha / \partial \gamma \\ \partial \alpha / \partial \rho \end{pmatrix} \tag{5.2}$$

The amplitude of α is defined as:

$$mag(\alpha) = \sqrt{(\psi_\gamma^2 + \psi_\rho^2)} \tag{5.3}$$

An orientation angle of $\nabla \alpha$ is calculated as:

$$\nabla_O(\kappa) = \arctan\left(\frac{\psi_\rho}{\psi_\gamma}\right) \tag{5.4}$$

For $\alpha(\gamma, \rho)$, ψ_γ and ψ_ρ are calculated by using various masks. A mask (ω) with 3×3 size is shown in Figure 5.1. The intensity of a central pixel is represented by λ. $\tau(\varphi = 1, 2, \ldots, 8)$ shows φ^{th} sibling of σ.

I_1	I_2	I_3
I_4	I_c	I_5
I_6	I_7	I_8

Figure 5.1: Oblique gradients based mask (W)

An OGPP prior has an ability to estimate 9 different oblique edges available in α with 3×3 patch size. Therefore, standard gradient operator has not ability to estimate all potential oblique edges [152].

Eleven possible oblique edges are presented in Figure 5.2. Figures 5.2 (a) and (b) represent oblique edges with mask size of 2×2.

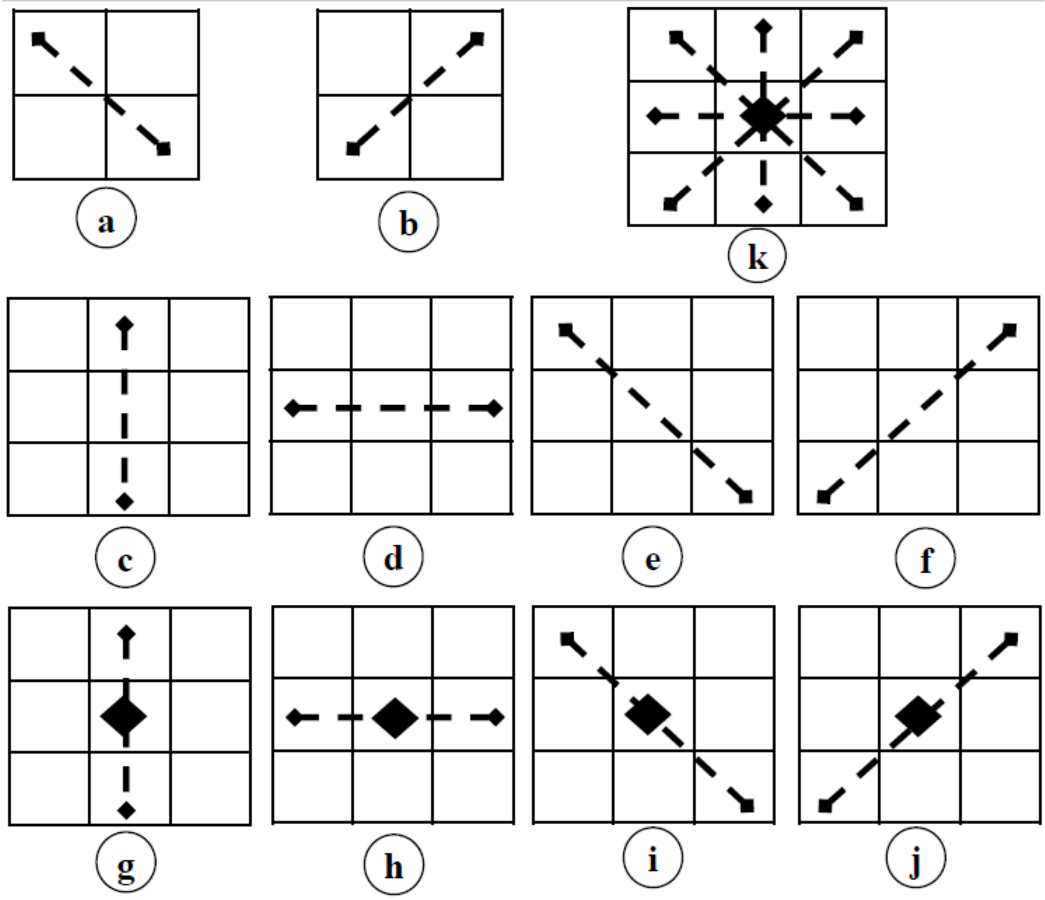

Figure 5.2: Oblique gradients with different mask sizes

Figures 5.2 (a) and (b) shows possible oblique edges as $\frac{\pi}{4} \leftrightarrow \frac{5\pi}{4}$ and $\frac{3\pi}{4} \leftrightarrow \frac{7\pi}{4}$. By considering $\omega \in \rho^{3\times3}$, four 2×2 masks are computed as: $\begin{bmatrix} \alpha_1 & \alpha_2 \\ \alpha_4 & \sigma \end{bmatrix}$, $\begin{bmatrix} \alpha_2 & \alpha_3 \\ \sigma & \alpha_5 \end{bmatrix}$, $\begin{bmatrix} \alpha_4 & \lambda \\ \alpha_6 & \alpha_7 \end{bmatrix}$, and $\begin{bmatrix} \alpha_c & I_5 \\ \alpha_7 & I_8 \end{bmatrix}$ with respect to σ. The corresponding OGPP angles are evaluated using Eqs.(5.5)-(5.8). If $\beta^1(m,n)$ =0, then an oblique edge (i.e, $\frac{\pi}{4} \leftrightarrow \frac{5\pi}{4}$) exists in mask $\begin{bmatrix} I_1 & I_2 \\ I_4 & I_c \end{bmatrix}$. If $\beta^1(m,n)$ is trend to $\pi/2(or-\pi/2)$, then oblique edge can be evaluated (along $3\pi/4 \leftrightarrow 7\pi/4$) in the mask $\begin{bmatrix} I_1 & I_2 \\ I_4 & I_c \end{bmatrix}$. Similarly, the different oblique edges can be found in other masks. Figures 5.2 (b)-(j) show eight different oblique gradient operators with mask size of 3×3. A combined OGPP operator is presented in Figure 5.2 (k). In Figure 5.2 (c)-(j), additional oblique edges (i.e, $\frac{\pi}{4} \leftrightarrow \frac{5\pi}{4}$, $\frac{3\pi}{4} \leftrightarrow \frac{7\pi}{4}$, $0 \leftrightarrow \pi$ and $\frac{\pi}{2} \leftrightarrow \frac{3\pi}{2}$) can be evaluated.

The corresponding OGPPs are evaluated by using Eqs. (5.9)-(5.12). λ is utilized in Eqs. (5.9) and Eqs. (5.10). However, I_c is not utilized in Eqs. (5.11) and (5.12).

$$\beta^1(\Lambda) = \arctan\left(\frac{\psi_\rho^1}{\psi_\gamma^1}\right) = \arctan\left(\frac{\alpha_1 - \lambda}{\alpha_2 - \alpha_4}\right) \tag{5.5}$$

$$\beta^2(\Lambda) = \arctan\left(\frac{\psi_\rho^2}{\psi_\gamma^2}\right) = \arctan\left(\frac{\alpha_3 - \lambda}{\alpha_2 - \alpha_5}\right) \tag{5.6}$$

$$\beta^3(\Lambda) = \arctan\left(\frac{\psi_\rho^3}{\psi_\gamma^3}\right) = \arctan\left(\frac{\alpha_6 - \lambda}{\alpha_7 - \alpha_4}\right) \tag{5.7}$$

$$\beta^4(\Lambda) = \arctan\left(\frac{\psi_\rho^4}{\psi_\gamma^4}\right) = \arctan\left(\frac{\alpha_8 - \lambda}{\alpha_7 - \alpha_5}\right) \tag{5.8}$$

$$\beta^5(\Lambda) = \arctan\left(\frac{\psi_\rho^5}{\psi_\gamma^5}\right) = \arctan\left(\frac{\alpha_2 + \alpha_7 - 2\times\lambda}{\alpha_4 + \alpha_5 - 2\times\lambda}\right) \tag{5.9}$$

$$\beta^6(\Lambda) = \arctan\left(\frac{\psi_\rho^6}{\psi_\gamma^6}\right) = \arctan\left(\frac{\alpha_1 + \alpha_8 - 2\times\lambda}{\alpha_3 + \alpha_6 - 2\times\lambda}\right) \tag{5.10}$$

$$\beta^7(\Lambda) = \arctan\left(\frac{\psi_\rho^7}{\psi_\gamma^7}\right) = \arctan\left(\frac{\alpha_2 - \alpha_7}{\alpha_4 - \alpha_5}\right) \tag{5.11}$$

$$\beta^8(\Lambda) = \arctan\left(\frac{\psi_\rho^8}{\psi_\gamma^8}\right) = \arctan\left(\frac{\alpha_1 - \alpha_8}{\alpha_3 - \alpha_6}\right) \tag{5.12}$$

Figure 5.2 (k) uses all siblings of Λ and computes an integrated gradient operator. The OGPP operator can be computed as:

$$\beta^9(\Lambda) = \arctan\left(\frac{\psi_\rho^9}{\psi_\gamma^9}\right) = \arctan\left(\frac{\sum_{\varphi=1}^{8}(\Lambda - \tau)}{8}\right) \tag{5.13}$$

The OGPPs (β) of a smoggy image can be estimated by considering Eqs. (5.5) to (5.13). An arctangent (arctan(.)) is utilized to estimate $\beta^s(\gamma,\rho)$. arctan(.) is used to control and monitor $\beta(\gamma,\rho)$ from rapid variation whenever I turns out to be greater or smaller. The range of pixel angle in orientation image ($\theta(\gamma,\rho)$) is constrained to $(\frac{-\pi}{2}, \frac{\pi}{2})$.

The transmission map $\bar{t}_{\mathrm{d}}$ can be mathematically defined as:

$$\eth(\delta) = 1 - \omega\beta^9_{c\in\{r,g,b\}}\left(beta^9_{y\in\Omega(\delta)}\left(\frac{\Lambda(\delta)}{\iota}\right)\right) \tag{5.14}$$

Here, $\omega = 0.95$ is a control parameter. The patch $\Omega(\delta)$ centered at δ.

The luminance-based transmission map (υ_l) can be defined as:

$$\upsilon_l(\delta) = \exp(-\beta\Gamma(\delta)) \tag{5.15}$$

Here, β is a scattering coefficient. Γ shows the modified luminance value. β is set to be 0.3324, 0.3433 and 0.3502 for red, green and blue channels, respectively.

The modified luminance (Γ) to compute the effect of depth map on the transmission map is redefined as:

$$\Gamma(\delta) = \frac{\tau}{\Gamma*}\Gamma(\delta), \tag{5.16}$$

Here, Γ defines luminance of smoggy image (α). τ defines the depth range. Γ^* indicates 95% percentile value of Γ. The coarse transmission map (μ) is computed by weightedly fusing of $\eth$ and μ_l as:

$$\mu(\delta) = \chi(\delta)\eth(\delta) + (1-\chi(\delta))\upsilon_l(\delta), \tag{5.17}$$

Here, transmission weight $\chi \in [0,1]$. If given pixel $\delta \in \Omega$ belongs to foreground objects, then, $\chi(\delta)$ approaches towards 1 and $\bar{t}(\delta) \to \eth(\delta)$. Similarly, $\chi(\delta)$ approaches toward 0 and $\upsilon(\delta) \to \upsilon_l(\delta)$.

The weight function (χ) is defined as:

$$\chi(\delta) = \frac{1}{1+\varkappa^{-\theta_1\eth(\delta)-\theta_2}} \tag{5.18}$$

Also,

$$\theta_1 = \frac{20}{\max(\eth)-\min(\eth)} \tag{5.19}$$

and

$$\theta_2 = -10 - \theta_1 \times \min(\eth) \tag{5.20}$$

But, it is not possible to restore the smoggy image in an efficient manner by using υ. Thus, a variational regularized model with hybrid constraints is implemented to refine υ.

5.2.2 Coarse transmission map refinement

Initially, to define a more efficient optical imaging model from Eq. (5.1) is redefined as:

$$\bar{\alpha}(\delta) = \bar{\phi}(\delta)\mu(\delta), \tag{5.21}$$

Here,

$$\bar{\alpha}(\delta) = \nu - \alpha(\delta) \tag{5.22}$$

and

$$\bar{\phi}\,(\mathrm{x}) = \nu - \kappa\,(\delta) \tag{5.23}$$

Here, $\delta \in \Omega$. Also, $\bar{\phi}$ can is defined as:

$$\bar{\phi}^{0}\,(\delta) = \frac{\nu - \delta\,(\delta)}{\max\left(\upsilon\,(\delta)\,,\mu_{\varepsilon}\right)} \tag{5.24}$$

Here, μ_{ε} is utilized to prevent imaging instability. For simplification $\alpha = \Lambda$, $\bar{\alpha} = \Lambda$ and $\bar{\phi} = \bar{\Omega}$ for $c \in \{r, g, b\}$.

To obtain more efficient restore images, variational model with hybrid regularization terms for transmission map refinement is formulated as:

$$\begin{aligned} \min_{\bar{\phi},\mu} \Big\{ & \frac{\lambda_1}{2}\left\|\bar{\alpha} - \bar{\phi}\mu\right\|_2^2 + \frac{\lambda_2}{2}\left\|\mu - \upsilon\right\|_2^2 \\ & + \lambda_3\left\|\omega \circ (\nabla\mu - \nabla\alpha)\right\|_1 + \lambda_4\left\|\nabla\bar{\phi}\right\|_1 + \lambda_5\left\|\nabla\mu\right\|_1 \Big\}, \end{aligned} \tag{5.25}$$

Here, $\lambda_{1\leq\bar{\alpha}\leq 5}$ represents a regularization parameter. In Eq. (5.25), the initial two terms can be viewed as a squared L2-norm data-fidelity term. The next L1-norm regularization is employed for edge preservation of transmission map. The final terms are total variation (TV) regularizers that may strengthen the approximation process. The weighting function (ω) is elected as:

$$\omega = \vartheta^{-\aleph\|\nabla I\|_2^2} \tag{5.26}$$

Here, $\aleph$ act as a controller. It can differentiate the homogeneous regions and the edges. The proposed approach (5.25) is hence effective for keeping the edges when controlling the undesirable artifacts in homogeneous regions. Because of the nonsmooth L1-norm penalties in Eq. (5.25), it is not suitable to produce stable options through conventional statistical approaches. Therefore, an switching method to successfully manage the nonsmooth optimization issue (5.25) is implemented. Three different parameters such as $\delta = \nabla\mu - \nabla\alpha$, $\iota = \nabla\bar{\phi}$ and $\varkappa = \nabla\mu$ are utilized. Thereafter, convert the unconstrained optimization issue (5.25) in to these confined variation as:

$$\begin{aligned} \min_{\alpha,\iota,\varkappa,\bar{\phi},\mu} \Big\{ & \frac{\lambda_1}{2}\left\|\bar{\alpha} - \bar{\phi}\mu\right\|_2^2 + \frac{\lambda_2}{2}\left\|\mu - \upsilon\right\|_2^2 \\ & + \lambda_3\left\|\omega \circ \delta\right\|_1 + \lambda_4\left\|\iota\right\|_1 + \lambda_5\left\|\varkappa\right\|_1 \Big\} \\ \text{s.t.} \quad & \delta = \nabla\mu - \nabla\alpha,\ \iota = \nabla\bar{\phi},\ \varkappa = \nabla\mu, \end{aligned} \tag{5.27}$$

The Lagrangian function can be redefined as:

$$\begin{aligned}\upsilon_v = \frac{\lambda_1}{2}\|\bar{\alpha}-\bar{\phi}\mu\|_2^2+\frac{\lambda_2}{2}\|\mu-\upsilon\|_2^2+\lambda_3\|\omega\circ\delta\|_1+\lambda_4\|\iota\|_1 \\ +\lambda_5\|\varkappa\|_1+\frac{\beta_1}{2}\|\delta-(\nabla\mu-\nabla I)-\frac{\xi}{\beta_1}\|_2^2 \\ +\frac{\beta_2}{2}\|\iota-\nabla\bar{\phi}-\frac{\eta}{\beta_2}\|_2^2+\frac{\beta_3}{2}\|\varkappa-\nabla\mu-\frac{\zeta}{\beta_3}\|_2^2\end{aligned} \tag{5.28}$$

Here, ξ, η and ζ show the Lagrangian multipliers, β_1, β_2 and β_3 are positive variables. The alternating direction approach of multipliers (ADMM) is utilized to divide $\mathscr{L}_{\mathscr{A}}$ into various constraints with respect to X, Y, Z, $\bar{J}$ and t. These alternative issues are resolved till we obtain optimal solutions.

$(\delta,\iota,\varkappa)$**-subproblems**: Given $\bar{\phi}$ and μ, $(\delta,\iota,\varkappa)$-subproblems are L1-regularized least-squares as:

$$\delta \leftarrow \min_{\delta}\left\{\lambda_3\|\omega\circ\delta\|_1+\frac{\beta_1}{2}\|\delta-(\nabla\mu-\nabla\alpha)-\frac{\xi}{\beta_1}\|_2^2\right\}, \tag{5.29}$$

$$\iota \leftarrow \min_{\iota}\left\{\lambda_4\|\iota\|_1+\frac{\beta_2}{2}\|\iota-\nabla\bar{\phi}-\frac{\eta}{\beta_2}\|_2^2\right\}, \tag{5.30}$$

$$\varkappa \leftarrow \min_{\varkappa}\left\{\lambda_5\|\varkappa\|_1+\frac{\beta_3}{2}\|\varkappa-\nabla t-\frac{\zeta}{\beta_3}\|_2^2\right\}, \tag{5.31}$$

Shrinkage operator can be utilized to obtain these subproblems as:

$$\delta \leftarrow \mathbf{shrinkage}\left(\nabla\mu-\nabla\alpha+\xi/\beta_1,\lambda_3\omega/\beta_1\right), \tag{5.32}$$

$$\iota \leftarrow \mathbf{shrinkage}\left(\nabla\bar{\phi}+\eta/\beta_2,\lambda_4/\beta_2\right), \tag{5.33}$$

$$\varkappa \leftarrow \mathbf{shrinkage}\left(\nabla\mu+\zeta/\beta_3,\lambda_5/\beta_3\right), \tag{5.34}$$

Here, the shrinkage operator is defined as:

$$\mathbf{shrinkage}(\iota,\theta)=\max(|\iota|-\theta,0)\circ\mathbf{sign}(\iota) \tag{5.35}$$

Here, **sign** defines signum function.

$(\bar{\phi},\mu)$**-subproblems**: Given δ, ι and $\varkappa$ computer using earlier iterations, the minimizations of υ_v with respect to $\bar{\phi}$ and μ are similar to resolve the following least-squares optimization issues as:

$$\begin{cases}\bar{\phi} \leftarrow \min_{\bar{\phi}}\left\{\frac{\lambda_1}{2}\|\bar{\alpha}-\bar{\phi}\mu\|_2^2+\frac{\beta_2}{2}\|\iota-\nabla\bar{\phi}-\frac{\eta}{\beta_2}\|_2^2\right\} \\ \mu \leftarrow \min_{\mu}\left\{\frac{\lambda_1}{2}\|\bar{\phi}\mu-\bar{\alpha}\|_2^2+\frac{\lambda_2}{2}\|\mu-\upsilon\|_2^2+\frac{\beta_1+\beta_3}{2}\|\nabla\mu-\psi\|_2^2\right\}\end{cases} \tag{5.36}$$

Here,

$$\psi=\frac{\beta_1\hat{\delta}+\beta_3\hat{\varkappa}}{\beta_1+\beta_3} \tag{5.37}$$

with

$$\hat{\delta} = \delta + \nabla I - \frac{\xi}{\beta_1} \tag{5.38}$$

and

$$\hat{\varkappa} = \varkappa - \frac{\zeta}{\beta_3} \tag{5.39}$$

Assume that $\mathscr{F}$ is forward fast Fourier transform (FFT). Therefore, closed-form solutions $\bar{\phi}$ and μ can be computed by making use of forward and inverse FFT operators as:

$$\bar{\phi} \leftarrow \mathscr{F}^{-1}\left(\frac{\lambda_1 \mathscr{F}(\bar{\alpha}/\mu) + \beta_2 \overline{\mathscr{F}(\nabla)} \mathscr{F}(\iota - \eta/\beta_2)}{\lambda_1 \mathscr{F}(\alpha) + \beta_2 \overline{\mathscr{F}(\nabla)} \mathscr{F}(\nabla)}\right), \tag{5.40}$$

$$t \leftarrow \mathscr{F}^{-1}\left(\frac{\lambda_1 \mathscr{F}(\bar{\alpha}/\bar{\phi}) + \lambda_2 \mathscr{F}(\upsilon) + (\beta_1 + \beta_3) \overline{\mathscr{F}(\nabla)} \mathscr{F}(\psi)}{(\lambda_1 + \lambda_2) \mathscr{F}(\alpha) + (\beta_1 + \beta_3) \overline{\mathscr{F}(\nabla)} \mathscr{F}(\nabla)}\right), \tag{5.41}$$

Here, α shows identity matrix, $\mathscr{F}^{-1}(\cdot)$ defines inverse FFT. $\overline{\mathscr{F}(\cdot)}$ shows complex conjugate function.

ξ, η and ζ update: In every iteration, the Lagrangian multipliers ξ, η and ζ can be reevaluated as

$$\begin{aligned} &\xi \leftarrow \xi - \upsilon\beta_1 (\delta - (\nabla\mu - \nabla\alpha)) \\ &\eta \leftarrow \eta - \upsilon\beta_2 (Y - \nabla\bar{J}) \\ &\zeta \leftarrow \zeta - \upsilon\beta_3 (\varkappa - \nabla t) \end{aligned} \tag{5.42}$$

Here, υ is a steplength.

5.2.3 Restoration model

It is found that $\bar{\phi}$ obtained using Eq. (5.40) suffers from textures distortion. Therefore, in this chapter, a smog free image (ϕ) is restored using computed t in Eq. (5.41). Finally, a restored image (ϕ) is obtained as:

$$\phi(\delta) = \frac{\alpha(\delta) - \Re}{\max(\mu(\delta), \mu_\varepsilon)} + \Re, \tag{5.43}$$

5.2.4 Hyper-parameters tuning

The proposed model requires many hyper-parameters to restore a smoggy image. Therefore, in this chapter, a Non-dominated Sorting Genetic Algorithm (NSGA) is used to tune the hyper-parameters of proposed approach. Percentage of saturated pixels, Contrast gain, Visible edges ratio, and Perceptual smog degradation density parameters are used to design a many-objective fitness function. For mathematical details of NSGA please refer [153]. The diagrammatic flow of the proposed model by considering NSGA is shown in Figure 5.3.

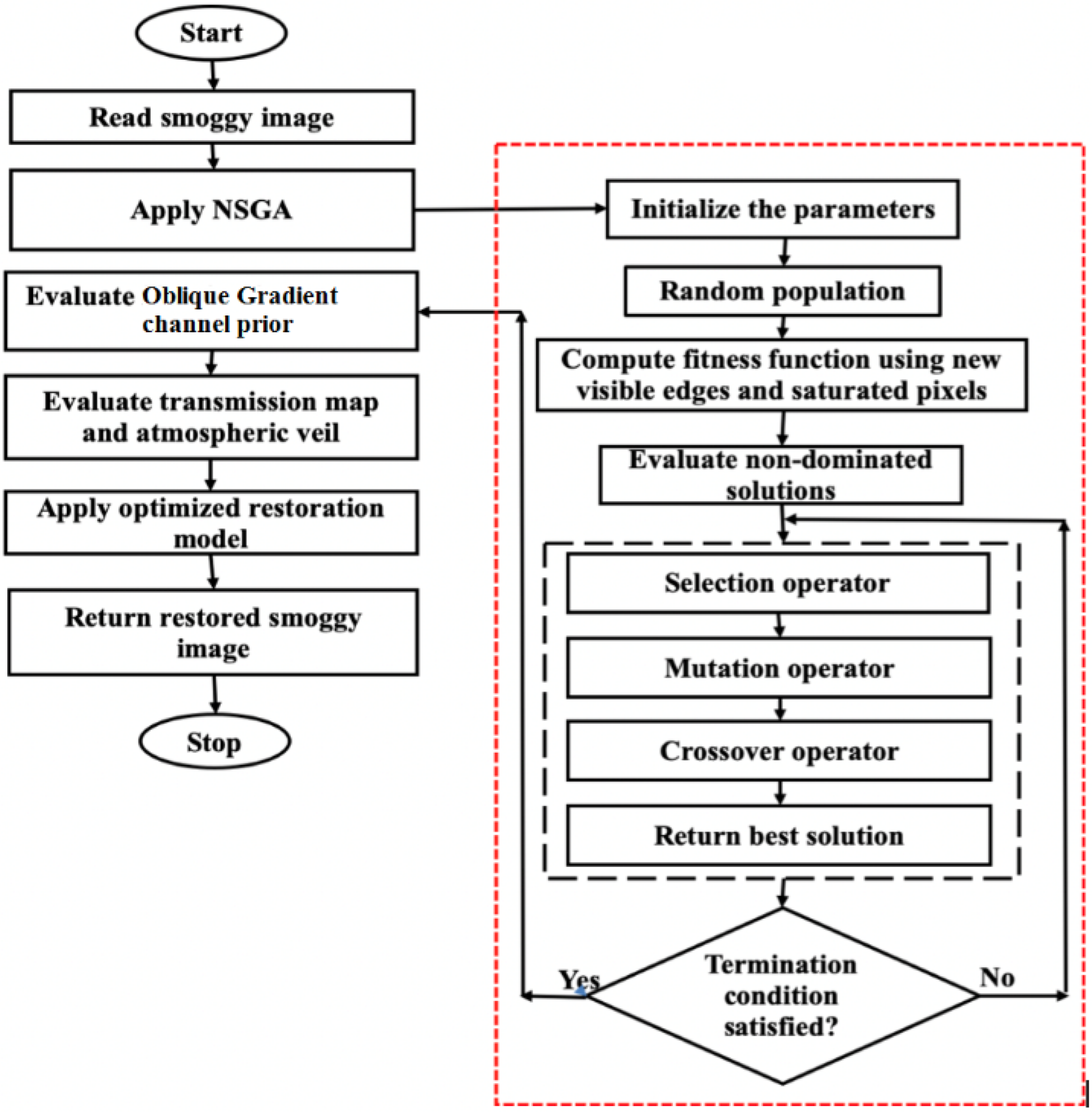

Figure 5.3: Non-dominated sorting genetic algorithm based hyper-parameters tuning of the proposed oblique gradient profile prior and variational minimization based desmogging model

5.3 Performance analyses of oblique gradient profile prior and variational minimization

The proposed desmogging model is simulated on Intel(R) Core(TM) $i5$-$4210U$ CPU @2.24 GHz and 8GB RAM on MATLAB 2013a tool. The mask size is taken as 5×5 pixels. Seven competitive desmogging approaches are considered to carry out the comparative analyses with proposed model. These approaches are DCP [6], CNN [7], CTT [8], TGV [9], WT [10], L_1 norm [11], and FVID [12]. Benchmark smoggy and real time smoggy images are taken for evaluating the effectiveness of the designed model. The size of images is considered 256×256. Subsequent sections contain various visual and quantitative results.

5.3.1 Patch size analysis of oblique gradient profile prior and variational minimization based desmogging model

In this experiment, the effect of mask size on the proposed desmogging model is considered. The considered mask sizes for evaluation are as 1×1, 5×5, and 11×11.

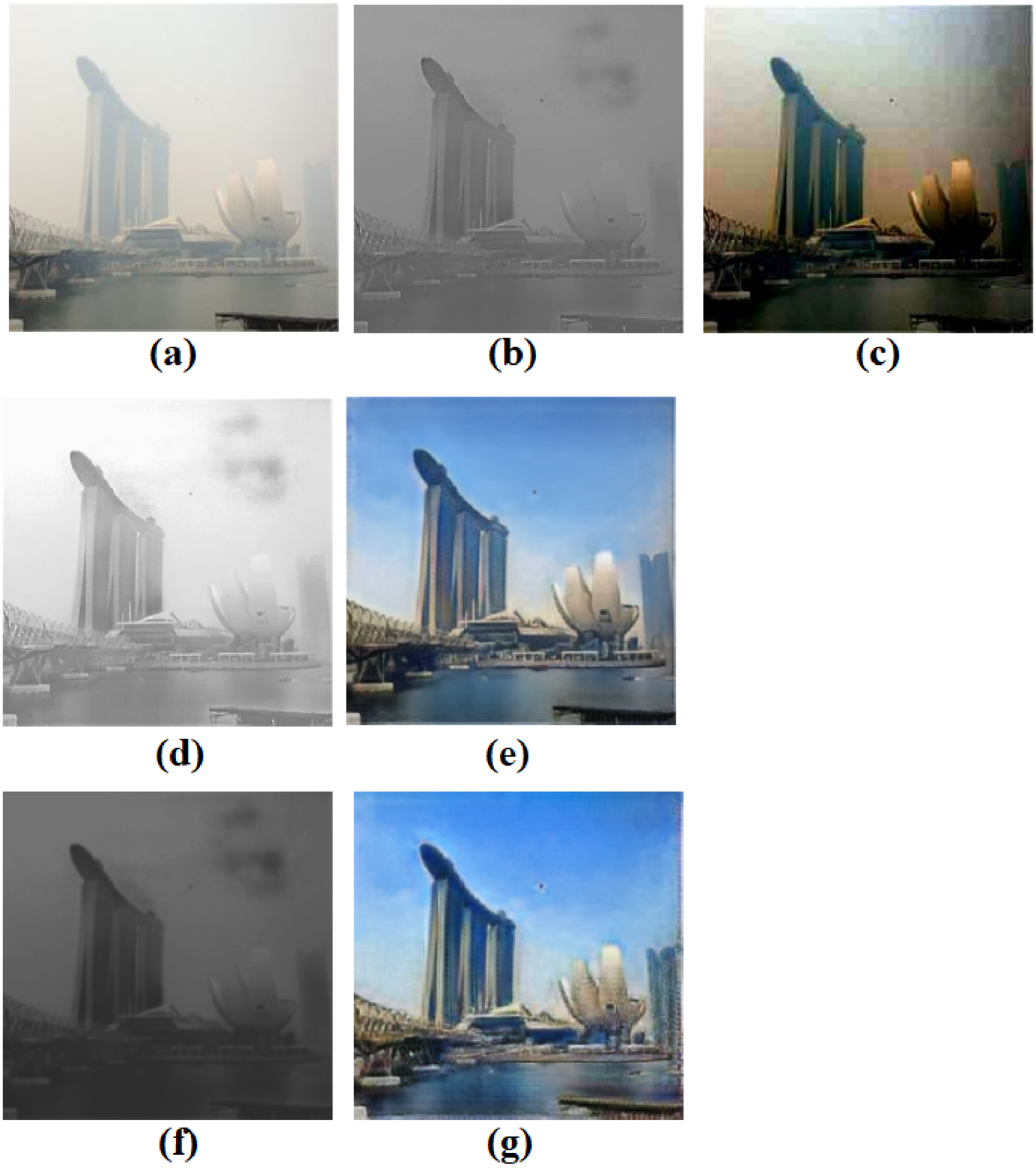

Figure 5.4: Patch size analyses (a) Input image, (b) Transmission map and (c) Restored image, with 1×1 mask size, respectively, (d) Transmission map and (e) Restored image with 5×5 mask size, respectively (f) Transmission map and (g) Restored image with 11×11 mask size, respectively.

Figure 5.4 demonstrates the effect of mask size on evaluated transmission maps and respective desmoggy images. Figures 5.4 (b) and 5.4 (c) demonstrate that the accuracy of the desmogging approach reduces with lesser mask size. Figures 5.4 (d) and 5.4 (e) demonstrate that the efficiency of the proposed desmogging approach is increased for 5×5 mask size. The restored image composes minimum saturated pixels and also the gradient reversal and halo artifacts are reduced. From Figures 5.4 (f) and 5.4 (g), it is clearly visible that the larger mask size makes the gradient and halo artifacts stronger.

5.3.2 Visual analyses of oblique gradient profile prior and variational minimization based desmogging model

The visual results of the designed desmogging approach is compared with seven existing desmogging techniques on some well-known benchmark smoggy images.

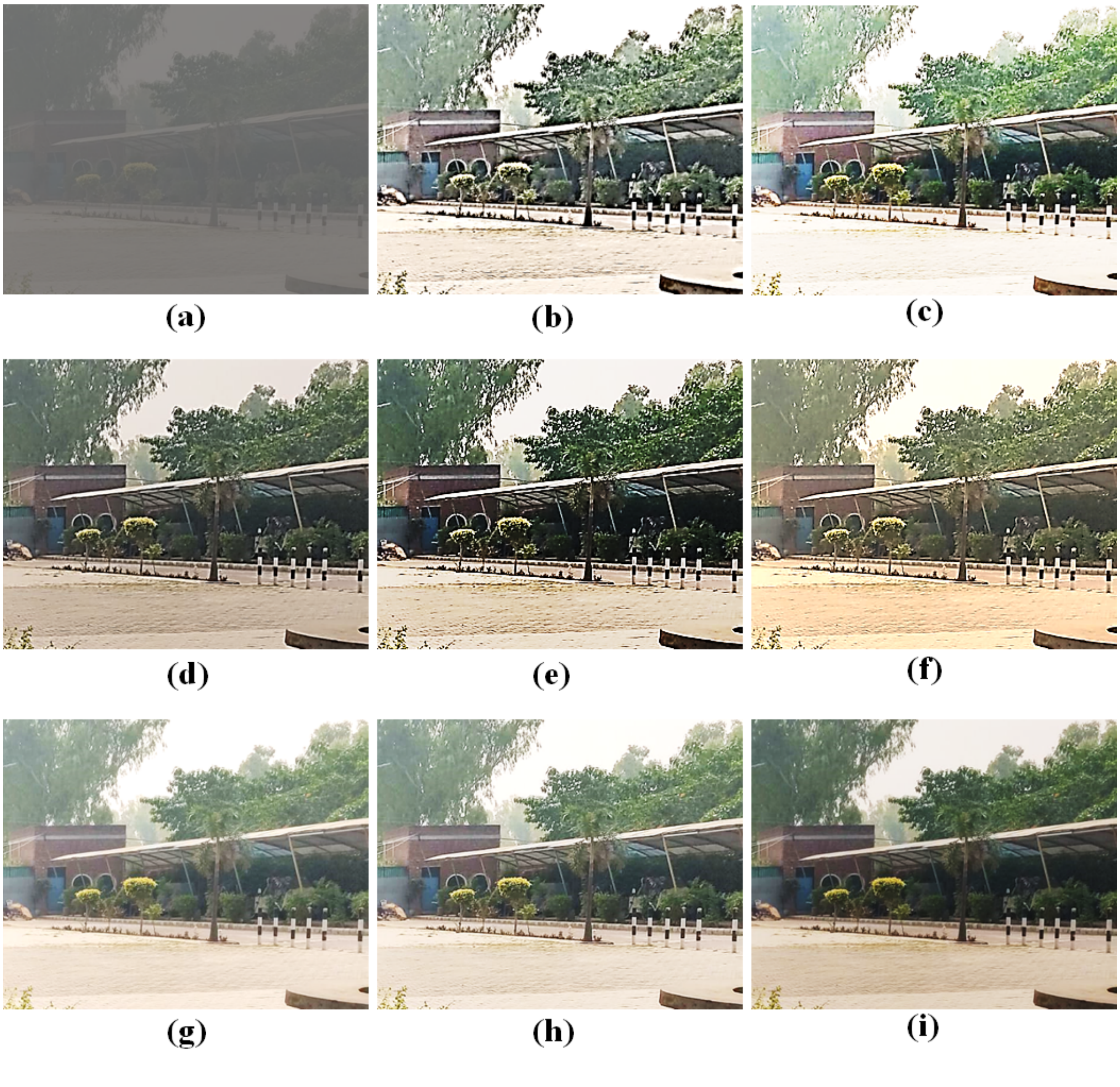

Figure 5.5: Results of desmogging models (a) Input image, (b) DCP [6], (c) CNN [7], (d) CTT [8], (e) TGV [9], (f) WT [10], (g) L_1 norm [11], (h) FVID [12] and (i) Proposed WIVC model.

Desmogging results in Figures 5.5 5.6, and 5.7 have demonstrated the benefits of the proposed desmogging model. DCP [27] and CTT [8] contain sky region and abundant textures contain headlights which are essentially different from the atmospheric light. It can be found that these approaches are not so-efficient to remove the smog for images effected from large smog gradient.

CNN [7] and TGV [9] tend to oversmooth fine image details and degrade image quality especially for images which are effected from large smog gradient. WT [10], L_1 norm [11], and FVID [12] show remarkable good results compared to the other approaches. However, these approaches are unable to preserve texture information of the restored smoggy images. The proposed approach does not suffer from edge, color and texture distortion issues.

Figure 5.6: Results of desmogging models (a) Input image, (b) DCP [6], (c) CNN [7], (d) CTT [8], (e) TGV [9], (f) WT [10], (g) L_1 norm [11], (h) FVID [12] and (i) Proposed WIVC desmogging model.

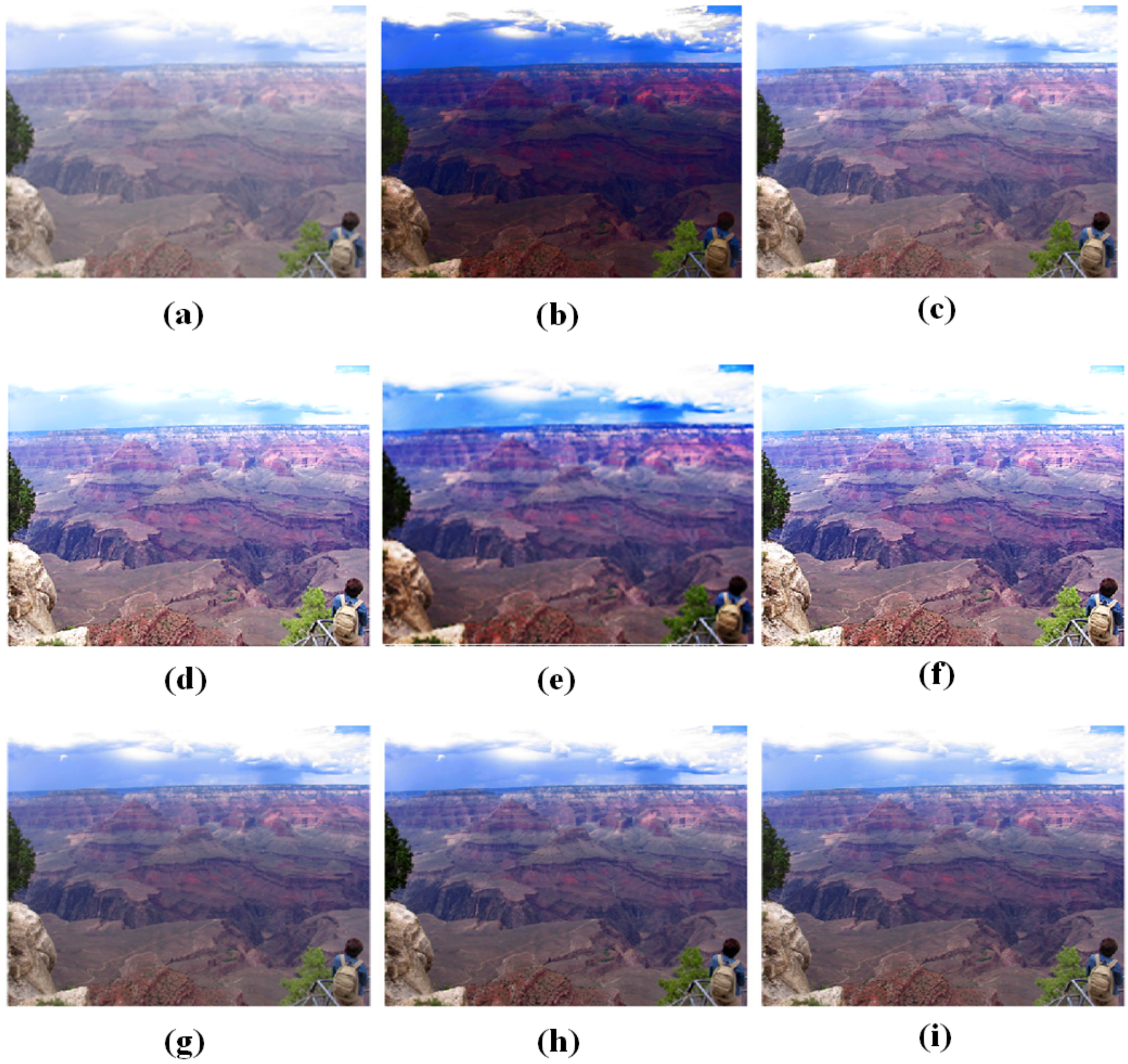

Figure 5.7: Results of desmogging models (a) Input image, (b) DCP [6], (c) CNN [7], (d) CTT [8], (e) TGV [9], (f) WT [10], (g) L_1 norm [11], (h) FVID [12] and (i) Proposed WIVC model.

5.3.3 Quantitative analyses of oblique gradient profile prior and variational minimization based desmogging model

The comparisons among the designed and the competitive desmogging model are also considered by using various performance measures such as percentage of saturated pixels (S_p), smog gradient, contrast gain (CG), visible edges, execution time (ET), peak signal to noise ratio, and structural similarity index metric.

Table 5.1 demonstrates CG analysis. It is found that the proposed WICF based desmogging model has significant CG values than competitive desmogging approaches.

Table 5.1: Contrast gain analyses of the proposed oblique gradient profile prior and variational minimization based desmogging model

Img.	DCP	CNN	CTT	TGV	WT	L_1	FVID	WIVC
IM_1	1.7865	1.7325	1.8624	1.7683	1.7843	1.8545	1.7724	1.8841
IM_2	1.7789	1.7275	1.8629	1.8801	1.8024	1.8408	1.7562	1.9018
IM_3	1.7658	1.8441	1.7732	1.7759	1.8711	1.8175	1.7639	1.8928
IM_4	1.7852	1.7293	1.7901	1.8979	1.7521	1.7491	1.7427	1.9196
IM_5	1.8198	1.8368	1.8034	1.7548	1.8411	1.8813	1.7993	1.9036
IM_6	1.8987	1.8483	1.8495	1.8361	1.7516	1.7449	1.8743	1.9204
IM_7	1.7446	1.7268	1.7317	1.7304	1.7282	1.8503	1.8729	1.8946
IM_8	1.7375	1.8669	1.8335	1.7363	1.8485	1.7921	1.8961	1.9178
IM_9	1.8358	1.8359	1.8519	1.8022	1.7559	1.8317	1.7278	1.8736
IM_{10}	1.7586	1.8699	1.8418	1.8885	1.8965	1.8591	1.8615	1.9182
IM_{11}	1.8828	1.7865	1.8227	1.8447	1.8716	1.7868	1.8227	1.9045
IM_{12}	1.8349	1.7758	1.8864	1.8786	1.7772	1.8279	1.7455	1.9081
IM_{13}	1.8304	1.8055	1.8761	1.7432	1.8314	1.7328	1.7994	1.8978
IM_{14}	1.8046	1.7973	1.7986	1.7665	1.8197	1.7471	1.8006	1.8414
IM_{15}	1.8392	1.8868	1.7717	1.7948	1.8675	1.8859	1.7784	1.9085

Table 5.2: Saturated pixels (S_p analyses of the proposed oblique gradient profile prior and variational minimization based desmogging model)

Img.	DCP	CNN	CTT	TGV	WT	L_1	FVID	WIVC
IM_1	0.0415	0.0618	0.0515	0.0217	0.0546	0.0872	0.0705	0.0198
IM_2	0.0974	0.0298	0.0899	0.0777	0.0131	0.0572	0.0166	0.0119
IM_3	0.0616	0.1315	0.2715	0.1947	0.2433	0.1383	0.1524	0.0598
IM_4	0.0418	0.1415	0.2173	0.2365	0.2889	0.2105	0.1895	0.0406
IM_5	0.0448	0.1673	0.2456	0.1575	0.2148	0.1386	0.1456	0.0436
IM_6	0.0583	0.1862	0.2541	0.2536	0.1312	0.2223	0.1547	0.0571
IM_7	0.0891	0.2604	0.2277	0.2641	0.1768	0.2492	0.1382	0.0879
IM_8	0.0368	0.2552	0.1303	0.1926	0.2804	0.2379	0.1375	0.0356
IM_9	0.0942	0.2514	0.2839	0.1296	0.1232	0.2509	0.2084	0.0937
IM_{10}	0.0619	0.1905	0.2701	0.2745	0.2668	0.2744	0.1463	0.0607
IM_{11}	0.0884	0.1335	0.1658	0.1826	0.1429	0.2778	0.1316	0.0872
IM_{12}	0.0404	0.2216	0.2371	0.1825	0.1725	0.1635	0.1393	0.0392
IM_{13}	0.0544	0.2621	0.1681	0.1797	0.1998	0.2718	0.2536	0.0532
IM_{14}	0.0675	0.1987	0.1746	0.2332	0.1527	0.1988	0.2691	0.0658
IM_{15}	0.0581	0.2398	0.1239	0.1717	0.1379	0.1301	0.2301	0.0569

Table 5.2 reveals that the proposed WICF based desmogging approach has minimum S_p values than competing restoration techniques.

Tables 5.3 and 5.4 demonstrate that the proposed WICF based desmogging approach has significantly more values of e and $\bar{r}$ than competing restoration techniques.

Table 5.3: New visible edges analyses of the proposed oblique gradient profile prior and variational minimization based desmogging model

Img.	DCP	CNN	CTT	TGV	WT	L_1	FVID	WIVC
IM_1	2.0085	2.6038	1.7613	2.1866	2.5667	1.8845	1.9566	2.8255
IM_2	2.4858	2.8253	2.6665	2.7313	2.6363	2.2137	2.2018	3.0474
IM_3	2.0289	2.2318	2.5058	2.7015	2.1873	2.2242	2.8358	3.0575
IM_4	2.8218	1.8502	2.2863	1.7278	1.9932	1.8122	2.2318	3.0435
IM_5	2.3406	2.3763	2.3727	2.0307	1.9241	2.6204	1.7577	2.8421
IM_6	2.5817	2.7486	2.6505	1.8658	2.4116	2.0606	2.2297	2.9703
IM_7	2.7396	2.6663	2.5424	1.7837	2.0324	1.8173	2.5652	2.9613
IM_8	2.1865	2.3312	2.3057	2.6453	2.7278	2.0063	2.1718	2.9495
IM_9	1.9729	1.9552	2.3085	1.9025	2.3685	2.7188	2.1116	2.9405
IM_{10}	2.2585	2.1331	2.1563	2.3794	1.9353	1.9926	2.0107	2.6011
IM_{11}	2.4076	2.3861	1.9333	2.7886	2.8948	1.8607	1.8816	3.1165
IM_{12}	2.4801	2.1814	2.4199	2.0202	2.1538	1.7952	2.1273	2.7018
IM_{13}	2.4351	1.7789	1.9363	2.4511	2.3676	2.7773	2.6807	2.8925
IM_{14}	2.2599	2.4123	2.2654	1.8608	2.4073	2.1177	2.6342	2.8559
IM_{15}	2.4249	2.6167	2.6234	2.0273	2.2283	2.8627	2.4149	3.0844

Table 5.4: Ratio of average gradient analyses of the proposed oblique gradient profile prior and variational minimization based desmogging model

Img.	DCP	CNN	CTT	TGV	WT	L_1	FVID	WIVC
IM_1	2.0953	1.9732	2.0953	2.8565	2.5004	2.8714	2.7623	3.0931
IM_2	2.0376	2.1891	2.1707	2.1713	1.8339	2.0452	2.0394	2.4108
IM_3	2.2806	2.4648	2.7992	2.5285	2.0167	2.6469	2.1003	3.0209
IM_4	2.3087	2.2267	2.8426	2.5195	2.1211	2.7781	2.1502	3.0643
IM_5	2.6393	1.7381	2.7806	1.8621	2.4382	2.6651	2.5976	3.0023
IM_6	1.8283	2.3465	2.4281	2.8799	1.893	1.7624	1.9593	3.1016
IM_7	2.7316	2.8374	2.3854	2.1537	2.3873	1.8578	2.6099	3.0591
IM_8	2.0074	2.2164	1.7598	2.4034	2.2618	1.9759	2.5646	2.7863
IM_9	2.2099	2.5789	2.0618	2.6919	2.2958	2.1343	2.6796	2.9136
IM_{10}	2.1493	2.4506	2.6265	2.0413	2.5386	2.6982	2.4366	2.9199
IM_{11}	2.4954	2.2997	2.5305	2.3752	2.1596	2.3717	2.2522	2.7522
IM_{12}	2.7722	2.8623	2.0066	1.8979	1.7632	2.0579	2.0489	3.0837
IM_{13}	2.4276	2.4808	2.1218	2.0198	2.2086	2.5852	2.8766	3.0983
IM_{14}	2.1963	1.8341	1.7941	2.6093	2.3974	2.6414	2.6728	2.8937
IM_{15}	2.4712	2.2435	2.0494	1.9886	2.0677	2.4725	2.8085	3.0302

Table 5.5: Execution time analyses of the proposed oblique gradient profile prior and variational minimization based desmogging model

Img.	DCP	CNN	CTT	TGV	WT	L_1	FVID	WIVC
IM_1	1.6827	1.2771	1.2811	1.2628	1.0487	1.1967	1.9802	1.0475
IM_2	1.2792	1.3367	1.6838	1.0611	1.2935	1.0462	1.3304	1.0453
IM_3	1.9836	1.8421	1.6814	1.3422	1.4978	1.5679	1.4975	1.3415
IM_4	1.3171	1.2331	1.4632	1.8677	1.4105	1.0968	1.3998	1.0956
IM_5	1.0651	1.4413	1.0636	1.8361	1.7124	1.3309	1.1253	1.0624
IM_6	1.2414	1.3354	1.5979	1.2797	1.1174	1.3475	1.5133	1.1162
IM_7	1.8343	1.4974	1.1123	1.5907	1.7515	1.7994	1.3676	1.1111
IM_8	1.5694	1.3206	1.1274	1.0395	1.4916	1.4242	1.9633	1.0383
IM_9	1.5474	1.4184	1.1395	1.3297	1.5988	1.6381	1.9589	1.1383
IM_{10}	1.1845	1.6931	1.5641	1.2589	1.2248	1.8203	1.4088	1.1833
IM_{11}	1.2612	1.3469	1.4852	1.5479	1.4052	1.0324	1.7127	1.0308
IM_{12}	1.2308	1.5089	1.1943	1.2796	1.2465	1.1185	1.6099	1.1173
IM_{13}	1.9084	1.7635	1.7184	1.0802	1.2637	1.6112	1.7955	1.0794
IM_{14}	1.9009	1.1256	1.3903	1.3394	1.5545	1.2375	1.0835	1.0823
IM_{15}	1.1343	1.8947	1.1634	1.6896	1.5234	1.1713	1.6207	1.1288

Table 5.5 demonstrates execution time (in seconds) analysis. It can be clearly noticed that the proposed WICF based desmogging approach is significantly faster than the competitive approaches.

Table 5.6 demonstrates smog gradient analyses. It is found that the proposed model is computationally faster than the existing approaches.

Table 5.6: Smog gradient analyses of the proposed oblique gradient profile prior and variational minimization based desmogging model

Img.	DCP	CNN	CTT	TGV	WT	L_1	FVID	Proposed
IM_1	2.0496	2.2412	2.1259	1.8333	1.7798	2.0864	2.0224	1.7786
IM_2	1.9477	1.9919	1.7394	2.2863	1.9414	1.9901	1.9109	1.7382
IM_3	1.9081	2.0821	2.2017	1.8236	1.8699	2.0223	1.7489	1.7477
IM_4	1.8541	1.9036	2.2311	1.8296	2.2209	2.0962	1.9231	1.8284
IM_5	1.9743	1.8502	1.9164	2.1104	1.8947	2.0978	1.9491	1.8494
IM_6	1.9285	2.2606	2.1083	2.0425	1.9375	2.2805	1.9785	1.9273
IM_7	2.2466	2.2695	1.7853	1.7281	1.9208	1.9918	1.9867	1.7269
IM_8	2.1197	2.1937	2.2231	2.1431	1.7752	1.9886	2.1691	1.7744
IM_9	2.2834	1.8309	1.8698	1.8264	1.8384	2.1682	2.2709	1.8252
IM_{10}	2.0828	1.8719	1.7288	1.7963	2.2443	2.0386	2.2368	1.7276
IM_{11}	1.7864	1.8741	1.7926	2.1949	2.0954	1.8999	2.2163	1.7852
IM_{12}	1.8189	2.2118	1.8735	2.1447	1.8708	1.8999	1.9918	1.8177
IM_{13}	2.1464	2.1439	2.1122	2.1986	1.9486	2.2692	2.2327	1.9474
IM_{14}	1.9264	2.0314	1.9543	1.8266	1.9892	1.8087	1.8531	1.8075
IM_{15}	2.2915	1.9563	1.7242	2.0586	2.1525	2.2626	1.8594	1.7238

Table 5.7 shows *PSNR* analysis of the designed and the competitive desmogging techniques. It is observed that the designed WICF based desmogging model has significant *PSNR* values than the existing desmogging approaches.

Table 5.7: Peak signal to noise ratio ($PSNR$) analyses of the proposed oblique gradient profile prior and variational minimization based desmogging model

Img.	DCP	CNN	CTT	TGV	WT	L_1	FVID	WIVC
IM_1	21.4352	21.3526	17.4847	25.2233	19.7988	25.9443	18.2123	27.1617
IM_2	19.3116	17.0435	20.2494	20.6626	23.4879	25.8382	17.2867	27.0597
IM_3	18.8484	25.6161	23.9796	23.4317	23.2487	18.2346	22.2156	26.8378
IM_4	18.2339	27.5254	26.7262	20.0566	24.6671	21.1583	16.8985	28.7417
IM_5	19.5562	22.7405	27.0682	26.7358	16.9676	17.7742	17.4003	28.2899
IM_6	24.6329	24.1535	24.2207	25.0819	18.6774	22.1306	19.8634	26.3036
IM_7	19.8772	25.4108	25.7341	19.6746	24.0464	22.7067	21.4376	26.9558
IM_8	23.7912	27.6807	21.8149	27.5865	21.3945	20.0567	25.7018	28.9024
IM_9	27.7838	26.8985	17.2131	21.0298	20.6644	20.2541	27.3327	29.0055
IM_{10}	19.3601	24.0618	27.6223	25.4101	21.8054	24.1566	26.9122	28.8449
IM_{11}	19.1564	24.7815	19.8693	23.0911	18.9015	21.2278	24.9664	26.1881
IM_{12}	25.6242	20.3746	22.8543	21.1459	21.6141	24.0739	19.1215	26.8459
IM_{13}	21.5967	18.4221	17.6245	27.7589	19.6873	24.5459	18.4737	28.9806
IM_{14}	25.2212	23.8978	21.1918	25.1502	23.8473	18.0318	17.5223	26.4429
IM_{15}	26.5971	27.3211	27.0028	24.3435	18.3536	21.7065	20.2388	28.5428

Table 5.8: Structural similarity index metric ($SSIM$) analyses of the proposed oblique gradient profile prior and variational minimization based desmogging model

Img.	DCP	CNN	CTT	TGV	WT	L_1	FVID	WIVC
IM_1	0.7502	0.7621	0.8674	0.7793	0.7619	0.8121	0.8067	0.8691
IM_2	0.8522	0.7959	0.8665	0.7255	0.8844	0.7894	0.8506	0.8861
IM_3	0.8162	0.8257	0.7331	0.8518	0.7529	0.7478	0.8314	0.8535
IM_4	0.8715	0.7578	0.7952	0.7856	0.7384	0.8636	0.8344	0.8727
IM_5	0.8096	0.8764	0.8039	0.7401	0.8591	0.7449	0.7541	0.8781
IM_6	0.7609	0.8439	0.8329	0.8803	0.7946	0.7783	0.8394	0.8826
IM_7	0.8386	0.7307	0.8905	0.8617	0.7783	0.8983	0.7417	0.9545
IM_8	0.8365	0.8015	0.7511	0.8364	0.8228	0.8279	0.8141	0.8382
IM_9	0.7311	0.7582	0.7299	0.7662	0.7614	0.7832	0.8893	0.8917
IM_{10}	0.7383	0.7258	0.7557	0.7393	0.7712	0.8029	0.7764	0.8046
IM_{11}	0.8988	0.7244	0.7391	0.8895	0.7345	0.8714	0.7234	0.9005
IM_{12}	0.7908	0.8567	0.8973	0.8488	0.8235	0.7834	0.8265	0.8993
IM_{13}	0.7582	0.7423	0.8575	0.7468	0.8319	0.7338	0.8559	0.8592
IM_{14}	0.7274	0.8645	0.8914	0.7522	0.7959	0.8781	0.8916	0.8933
IM_{15}	0.7277	0.8823	0.8005	0.8784	0.7616	0.7813	0.8444	0.8844

Table 5.8 shows *SSIM* analyses of the designed and the existing desmogging approaches. It is found that the designed WICF based desmogging approach has significant *SSIM* values than the existing desmogging approaches.

From Tables 5.1 to 5.8, it has been found that the NICP outperforms the competitive desmogging models in terms of contrast gain, new visible edges, average gradient, peak signal to noise ratio, and structural similarity index metric by 1.2883%, 1.5392%, 0.8271%, 0.8928% and 1.2813%, respectively. Compared to the existing approaches, NICP also minimizes the smog gradient, saturated pixels, and execution time by 0.8282%, 0.7291% and 1.1428%, respectively.

5.4 Summary

An efficient desmogging model has been designed and implemented in this chapter. Initially, the proposed WICF based desmogging model integrates transmission maps computed from oblique gradient prior and luminance-based transmission map are integrated. Thereafter, the integrated transmission map is refined by using a novel variational regularized model with hybrid constraints. A Non-dominated sorting genetic algorithm (NSGA) has been utilized to tune the hyper-parameters of the designed approach. Extensive experimental results reveal that the designed WICF based desmogging model has an ability to preserve color, edges and texture information of restored images. Therefore, performance analysis indicate that the designed desmogging model can be applied for real-time applications.

Chapter 6

Conclusions and future work

Outline

The thesis is hereby concluded in this chapter, emphasizing the contributions made towards the proposed research domain and presenting future directions in the research area.

6.1 Conclusions

Images obtained in smoggy environment are degraded by the scattering of atmospheric particles. Therefore, the captured images have poor visibility and low contrast. It directly affects the performance of various computer vision applications. The degradation in obtained images is represented by the transmission map, which is one of the most significant step in the desmogging model. However, the estimation of transmission map is an under-constraint issue.

Dark channel prior (DCP) is one of the commonly used model to estimate the transmission map. DCP stated that most of the non-sky regions have at least one color channel (*i.e.,* red, green, or blue) containing low-intensity pixels. Extensive analyses demonstrated that most of the images satisfy same observation of DCP. It has achieved remarkable results when combined with the soft matting. But, soft matting greatly affects the computational speed. With this, DCP may become invalid when the objects in an image are essentially similar to the airlight. It is also not capable to restore the gray regions of weather degraded images.

From the comprehensive study on desmogging models, it has been observed that the development of efficient desmogging model is still an extensive area of research. Smog degradation is generally produced by the suspension of invisible water droplets in the atmosphere. Whenever light met with these invisible water droplets then it scatters and results in loss of visibility of the actual scene radiance. The smog degradation model can be mathematically defined as an optical imaging model.

The optical smog imaging model shows that the obtained smoggy images depend upon actual scene radiance, transmission map and atmospheric veil. Thus, inversion of this optical model may help in obtaining the restored image. However, single smoggy images do not provide the details like transmission map and atmospheric veil . Therefore, it is desirable to predict these transmission map and atmospheric veil to restore smoggy images. However, an efficient estimation of transmission map and atmospheric veil is still an extensive field of research.

Channel priors was found to be best suitable method for estimation of transmission map and atmospheric veil from smoggy images. However, the obtained transmission map and atmospheric veil suffer from noise and degradation issue especially when images contain sky regions or images contain significant smog gradient. Therefore, image filters were considered to refine the estimated transmission map to obtain more significant results. However, the existing desmogging models are affected by the color, texture, and edge distortion issues. These models also provide halo and gradient reversal artifacts.

To overcome afore-mentioned issues, in this thesis three different desmogging models were proposed and implemented i.e., NICP, NGCP, and WIVC.

To overcome these issues, various desmogging models are proposed in this research work. Initially, a novel illumination channel prior (NICP) is designed to restore smoggy images in a significant way. A gradient magnitude based filter is also proposed for refining the transmission map. Finally, the smog-free images are achieved by employing the computed depth information of smoggy images and smog restoration model.

The subjective and quantitative analyses were drawn to estimate the effectiveness of the designed NICP based desmogging model. It has been found that the proposed NICP based desmogging approach outperforms competitive models in terms of some well-known performance metrics. It has been found that the NICP outperforms the competitive desmogging models in terms of contrast gain, new visible edges, average gradient, peak signal to noise ratio, and structural similarity index metric by 1.2883%, 1.5392%, 0.8271%, 0.8928% and 1.2813%, respectively. Compared to the competing techniques, NICP also minimizes the smog gradient, saturated pixels, and execution time by 0.8282%, 0.7291% and 1.1428%, respectively.

Although, NICP outperforms the existing desmogging approaches in case of smoggy images, but, for images with complex background and having large smog gradient, it may not be so-effective. Therefore, a novel gradient channel prior and information gain based filter (NGCP) desmogging approach has been designed. Initially, gradient channel prior has been used to estimate the optical information of smoggy images. Thereafter, a information gain based filter has been designed to improve the transmission map. The smog-free image has been then computed using an improved restoration model. Finally, the effectiveness of the designed NGCP based desmogging approach is compared with seven existing restoration techniques on some well-known benchmark and real-life desmogging images. From, comparative analyses, it has been found that the proposed model outperforms the competitive models in terms of contrast gain, new visible edges, average gradient, peak signal to noise ratio, and structural similarity index metric by 1.8373%, 1.9379%, 1.9838%, 1.9382% and 1.8272%, respectively. Compared to the competing techniques, NGCP also minimizes the smog gradient, saturated pixels, and execution time by 1.2279%, 1.8273% and 0.9823%, respectively.

Although, NICP and NGCP provide promising desmogging results when compared to the competitive desmogging approaches. However, it suffers from sky-regions and color distortion, especially in the case of images effected from large smog gradients. Also, the effect of hyper-parameters tuning issue was also ignored. Therefore, a weighted integrated transmission maps and integrated variational regularized model with hybrid constraints (WIVC) based desmogging model was implemented. The transmission map estimation was computed from the weighted integrated transmission maps by considering foreground and sky regions. The computed transmission map was refined using an integrated variational regularized model with hybrid constraints. The obtained results revealed that WIVC outperforms the competitive desmogging models in terms of contrast gain, new visible edges, average gradient, peak signal to noise ratio, and structural similarity index metric by 1.9379%, 1.3820%, 1.3289%, 1.9389% and 1.7392%, respectively. Compared to the competing techniques, WIVC also minimizes the smog gradient, saturated pixels, and execution time by 1.8382%, 1.2372% and 0.8272%, respectively.

However, the designed WIVC approach suffers from the hyper-parameters tuning issue. Therefore, in this chapter, a Non-dominated sorting genetic algorithm (NSGA) is also used to tune the hyper-parameters of the proposed WIVC approach. Extensive comparative results reveal that the WIVC performs effectively across a wide range of smog degradation levels without causing any visible artifacts. It is found that the designed approach outperforms seven competitive desmogging approaches in terms of various performance metrics on benchmark and real-life smoggy images. The main benefits of WIVC over the competitive desmogging models are as: (i) WIVC can efficiently overcome the sky region issue. Also, WIVC can preserve texture details of the restored smoggy images more efficiently.

Thorough extensive comparative analyses, it is found that the proposed models i.e., NICP, NGCP, and WIVC can significantly suppress visual artifacts for smoggy images and obtain significantly better restored images as compared to the existing desmogging models both quantitatively and qualitatively. Moreover, the proposed models take significantly lesser time, therefore, the proposed models will facilitate various real-life imaging systems.

Therefore, the proposed desmogging models have efficiently reduce the distortion of edge, color and texture details of smoggy images. The visual analyses have shown that the proposed modes i.e., NICP, NGCP, and WIVC can efficiently restore the smoggy images. These models provide smog-free images with the vivid color, good visibility, significant spatial and spectral, and texture details. These proposed models also provide real color sky, without introducing much gradient reversal and halo artifacts in the restored smog-free images. Additionally, the proposed models provide smog-fee images at good computational speed as compared to the competitive desmogging approaches. Therefore, the developed models can be used as a preprocessing tool in real-life imaging systems.

6.2 Future work

Following are some of the future directions of this thesis.

i In this thesis, not much work is done to propose fusion based desmogging models to enhance the restored images. Therefore, in near future one may use fusion models to obtain more accurate restored smoggy images.

ii In this thesis, only non-dominated sorting genetic algorithm was used to tune the hyper-parameters of the proposed model. Thus, in future, some recently proposed meta-heuristic models may be considered to tune the parameters of the proposed models.

iii The proposed models may be used to other kinds of images such as satellite images, underwater images, *etc.*

iv The transform domain based desmogging models can also be used to obtain smog-free images.

List of publications

1. Jeevan Bala and Kamlesh Lakhwani. "Single image desmogging using oblique gradient profile prior and variational minimization", **Accepted** in Multidimensional Systems and Signal Processing, Springer. **[SCI Indexed, Impact Factor 1.810]**

2. Jeevan Bala and Kamlesh Lakhwani. "Performance evaluation of various desmogging techniques for single smoggy images", **Accepted** in Modern Physics Letters B, World Scientific Publishing Company. **[SCI Indexed, Impact Factor 0.73]**

3. Jeevan Bala and Kamlesh Lakhwani. "Desmogging of Smog Affected Images Using Illumination Channel Prior", **Accepted** in International Conference on Innovative Computing and Communications, Springer.

4. Jeevan Bala and Kamlesh Lakhwani. "Single image desmogging using Gradient channel prior and Information gain based bilateral", **Accepted** in 3rd International Conference on Emerging Technologies in Computer Engineering: Machine Learning and Internet of Things (ICETCE), IEEE.

Bibliography

[1] Q. Zhu, J. Mai, and L. Shao, "A fast single image haze removal algorithm using color attenuation prior," *IEEE Transactions on Image Processing*, vol. 24, no. 11, pp. 3522–3533, 2015.

[2] D. Singh and V. Kumar, "Dehazing of remote sensing images using improved restoration model based dark channel prior," *The Imaging Science Journal*, vol. 65, no. 5, pp. 1–11, 2017.

[3] B.-H. Chen, S.-C. Huang, and J. H. Ye, "Hazy image restoration by bi-histogram modification," *ACM Transactions on Intelligent Systems and Technology (TIST)*, vol. 6, no. 4, p. 50, 2015.

[4] W. Sun, H. Wang, C. Sun, B. Guo, W. Jia, and M. Sun, "Fast single image haze removal via local atmospheric light veil estimation," *Computers & Electrical Engineering*, vol. 46, pp. 371–383, 2015.

[5] B. H. Chen, S. C. Huang, and F. C. Cheng, "A high-efficiency and high-speed gain intervention refinement filter for haze removal," *Journal of Display Technology*, vol. 12, no. 7, pp. 753–759, 2016.

[6] A. Golts, D. Freedman, and M. Elad, "Unsupervised single image dehazing using dark channel prior loss," *IEEE Transactions on Image Processing*, vol. 29, pp. 2692–2701, 2020.

[7] L. Li, Y. Dong, W. Ren, J. Pan, C. Gao, N. Sang, and M. Yang, "Semi-supervised image dehazing," *IEEE Transactions on Image Processing*, vol. 29, pp. 2766–2779, 2020.

[8] C. O. Ancuti, C. Ancuti, C. De Vleeschouwer, and M. Sbetr, "Color channel transfer for image dehazing," *IEEE Signal Processing Letters*, vol. 26, pp. 1413–1417, Sep. 2019.

[9] Y. Gu, X. Yang, and Y. Gao, "A novel total generalized variation model for image dehazing," *Journal of Mathematical Imaging and Vision*, vol. 61, no. 9, pp. 1329–1341, 2019.

[10] H. Khan, M. Sharif, N. Bibi, M. Usman, S. A. Haider, S. Zainab, J. H. Shah, Y. Bashir, and N. Muhammad, "Localization of radiance transformation for image dehazing in wavelet domain," *Neurocomputing*, vol. 381, pp. 141 – 151, 2020.

[11] T. Cui, J. Tian, E. Wang, and Y. Tang, "Single image dehazing by latent region-segmentation based transmission estimation and weighted l1-norm regularisation," *IET Image Processing*, vol. 11, no. 2, pp. 145–154, 2017.

[12] A. Galdran, J. Vazquez-Corral, D. Pardo, and M. BertalmÃo, "Fusion-based variational image dehazing," *IEEE Signal Processing Letters*, vol. 24, no. 2, pp. 151–155, 2017.

[13] Y. Xu, J. Wen, L. Fei, and Z. Zhang, "Review of video and image defogging algorithms and related studies on image restoration and enhancement," *IEEE Access*, vol. 4, pp. 165–188, 2016.

[14] H.-Y. Yang, P.-Y. Chen, C.-C. Huang, Y.-Z. Zhuang, and Y.-H. Shiau, "Low complexity underwater image enhancement based on dark channel prior," in *Innovations in Bio-inspired Computing and Applications (IBICA), 2011 Second International Conference on*, pp. 17–20, IEEE, 2011.

[15] J. M. Crebolder and R. B. Sloan, "Determining the effects of eyewear fogging on visual task performance," *Applied ergonomics*, vol. 35, no. 4, pp. 371–381, 2004.

[16] N.-E. Rikli and M. Alabdulkarim, "Cross-layer-based adaptive video transport over low bit-rate multihop wsns," *Canadian Journal of Electrical and Computer Engineering*, vol. 37, no. 4, pp. 182–191, 2014.

[17] M. Singh, M. C. Govil, and E. S. Pilli, "Chact: Convex hull enabled active contour technique for salient object detection," *IEEE Access*, vol. 6, pp. 22441–22451, 2018.

[18] L. Guan, "Model-based neural evaluation and iterative gradient optimization in image restoration and statistical filtering," *Journal of Electronic Imaging*, vol. 4, no. 4, pp. 407–413, 1995.

[19] X. Lian, Y. Pang, and A. Yang, "Learning intensity and detail mapping parameters for dehazing," *Multimedia Tools and Applications*, pp. 1–26, 2017.

[20] Y. Yang, X. Sun, H. Yang, and C.-T. Li, "Removable visible image watermarking algorithm in the discrete cosine transform domain," *Journal of Electronic Imaging*, vol. 17, no. 3, pp. 033008–033008, 2008.

[21] H. Tan, X. He, Z. Wang, and G. Liu, "Parallel implementation and optimization of high definition video real-time dehazing," *Multimedia Tools and Applications*, pp. 1–22, 2016.

[22] K. B. Gibson and T. Q. Nguyen, “An analysis of single image defogging methods using a color ellipsoid framework,” *EURASIP Journal on Image and Video Processing*, vol. 2013, no. 1, p. 37, 2013.

[23] V. Paidi, H. Fleyeh, J. Hakansson, and R. G. Nyberg, “Smart parking sensors, technologies and applications for open parking lots: a review,” *IET Intelligent Transport Systems*, vol. 12, no. 8, pp. 735–741, 2018.

[24] R. T. Tan, “Visibility in bad weather from a single image,” in *2008 IEEE Conference on Computer Vision and Pattern Recognition*, pp. 1–8, June 2008.

[25] R. Srivastava and S. Srivastava, “Restoration of poisson noise corrupted digital images with nonlinear pde based filters along with the choice of regularization parameter estimation,” *Pattern Recognition Letters*, vol. 34, no. 10, pp. 1175–1185, 2013.

[26] R. Kawakami, H. Zhao, R. T. Tan, and K. Ikeuchi, “Camera spectral sensitivity and white balance estimation from sky images,” *International Journal of Computer Vision*, vol. 105, no. 3, pp. 187–204, 2013.

[27] K. He, J. Sun, and X. Tang, “Single image haze removal using dark channel prior,” *IEEE Transactions on Pattern Analysis and Machine Intelligence*, vol. 33, no. 12, pp. 2341–2353, 2011.

[28] R. Fattal, “Single image dehazing,” *ACM transactions on graphics (TOG)*, vol. 27, no. 3, p. 72, 2008.

[29] X. Fu, J. Wang, D. Zeng, Y. Huang, and X. Ding, “Remote sensing image enhancement using regularized-histogram equalization and dct,” *IEEE Geoscience and Remote Sensing Letters*, vol. 12, no. 11, pp. 2301–2305, 2015.

[30] W. Zhang and X. Hou, “Estimation algorithm of atmospheric light based on ant colony optimization,” in *Proceedings of the 2017 International Conference on Intelligent Systems, Metaheuristics & Swarm Intelligence*, pp. 20–25, ACM, 2017.

[31] L. Wang, W. Xie, and J. Pei, “Patch-based dark channel prior dehazing for rs multi-spectral image,” *Chinese Journal of Electronics*, vol. 24, no. 3, pp. 573–578, 2015.

[32] W. Zhang, J. Liang, H. Ju, L. Ren, E. Qu, and Z. Wu, “Study of visibility enhancement of hazy images based on dark channel prior in polarimetric imaging,” *Optik International Journal for Light and Electron Optics*, vol. 130, pp. 123 – 130, 2017.

[33] S. Liu, M. A. Rahman, S. C. Liu, C. Y. Wong, C.-F. Lin, H. Wu, and N. Kwok, “Image de-hazing from the perspective of noise filtering,” *Computers and Electrical Engineering*, 2016.

[34] B. Xie, F. Guo, and Z. Cai, "Improved single image dehazing using dark channel prior and multi-scale retinex," in *Intelligent System Design and Engineering Application (ISDEA), 2010 International Conference on*, vol. 1, pp. 848–851, IEEE, 2010.

[35] W. Sun, "A new single-image fog removal algorithm based on physical model," *Optik - International Journal for Light and Electron Optics*, vol. 124, no. 21, pp. 4770 – 4775, 2013.

[36] H. Xu, J. Guo, Q. Liu, and L. Ye, "Fast image dehazing using improved dark channel prior," in *2012 IEEE International Conference on Information Science and Technology*, pp. 663–667, IEEE, 2012.

[37] Z. Ma, J. Wen, C. Zhang, Q. Liu, and D. Yan, "An effective fusion defogging approach for single sea fog image," *Neurocomputing*, vol. 173, pp. 1257 – 1267, 2016.

[38] I. Riaz, T. Yu, Y. Rehman, and H. Shin, "Single image dehazing via reliability guided fusion," *Journal of Visual Communication and Image Representation*, vol. 40, pp. 85 – 97, 2016.

[39] R. Fattal, "Dehazing using color-lines," *ACM Transactions on Graphics (TOG)*, vol. 34, no. 1, p. 13, 2014.

[40] J.-B. Wang, N. He, L.-L. Zhang, and K. Lu, "Single image dehazing with a physical model and dark channel prior," *Neurocomputing*, vol. 149, pp. 718–728, 2015.

[41] H. Song, Y. Gao, and Y. Chen, "Fast image dehazing using fuzzy system and hybrid evolutionary algorithm," in *Foundations and Practical Applications of Cognitive Systems and Information Processing*, pp. 275–283, Springer, 2014.

[42] C. Chen, M. N. Do, and J. Wang, "Robust image and video dehazing with visual artifact suppression via gradient residual minimization," in *European Conference on Computer Vision*, pp. 576–591, Springer, 2016.

[43] D. Singh and V. Kumar, "Modified gain intervention filter based dehazing technique," *Journal of Modern Optics*, vol. 64, no. 20, pp. 1–14, 2017.

[44] S. Lee, S. Yun, J.-H. Nam, C. S. Won, and S.-W. Jung, "A review on dark channel prior based image dehazing algorithms," *EURASIP Journal on Image and Video Processing*, vol. 2016, no. 1, p. 4, 2016.

[45] B. Cai, X. Xu, K. Jia, C. Qing, and D. Tao, "Dehazenet: An end-to-end system for single image haze removal," *IEEE Transactions on Image Processing*, vol. 25, pp. 5187–5198, Nov 2016.

[46] C.-H. Xie, W.-W. Qiao, Z. Liu, and W.-H. Ying, "Single image dehazing using kernel regression model and dark channel prior," *Signal, Image and Video Processing*, pp. 1–8, 2016.

[47] J.-H. Kim, W.-D. Jang, J.-Y. Sim, and C.-S. Kim, "Optimized contrast enhancement for real-time image and video dehazing," *Journal of Visual Communication and Image Representation*, vol. 24, no. 3, pp. 410 – 425, 2013.

[48] L. Wang, L. Xiao, and Z. Wei, "Image dehazing using two-dimensional canonical correlation analysis," *IET Computer Vision*, vol. 9, no. 6, pp. 903–913, 2015.

[49] Z. Ma, J. Wen, C. Zhang, Q. Liu, and D. Yan, "An effective fusion defogging approach for single sea fog image," *Neurocomputing*, vol. 173, pp. 1257–1267, 2016.

[50] S. Sharma and S. Bhalla, "Improved haze removal of underwater images using particle swarm optimization," *International Journal of Computer Applications*, vol. 122, no. 4, 2015.

[51] A. Chatterjee and P. Siarry, "Advances in evolutionary optimization based image processing," *Engineering Applications of Artificial Intelligence*, no. 31, pp. 1–2, 2014.

[52] H. Kuang, X. Zhang, Y.-J. Li, L. L. H. Chan, and H. Yan, "Nighttime vehicle detection based on bio-inspired image enhancement and weighted score-level feature fusion," *IEEE Transactions on Intelligent Transportation Systems*, vol. 18, no. 4, pp. 927–936, 2017.

[53] P. Shanmugavadivu and K. Balasubramanian, "Particle swarm optimized multi-objective histogram equalization for image enhancement," *Optics & Laser Technology*, vol. 57, pp. 243–251, 2014.

[54] A. Draa and A. Bouaziz, "An artificial bee colony algorithm for image contrast enhancement," *Swarm and Evolutionary computation*, vol. 16, pp. 69–84, 2014.

[55] Z. Ye, M. Wang, Z. Hu, and W. Liu, "An adaptive image enhancement technique by combining cuckoo search and particle swarm optimization algorithm," *Computational intelligence and neuroscience*, vol. 2015, p. 13, 2015.

[56] S. Liu, M. A. Rahman, C. Y. Wong, C.-F. Lin, H. Wu, N. Kwok, *et al.*, "Image de-hazing from the perspective of noise filtering," *Computers & Electrical Engineering*, vol. 62, pp. 345–359, 2017.

[57] A. Galdran, J. Vazquez-Corral, D. Pardo, and M. Bertalmío, "Fusion-based variational image dehazing," *IEEE Signal Processing Letters*, vol. 24, no. 2, pp. 151–155, 2017.

[58] L. Xiong, H. Li, and L. Xu, “An enhancement method for color retinal images based on image formation model,” *Computer Methods and Programs in Biomedicine*, vol. 143, pp. 137 – 150, 2017.

[59] X. Tang and L. Jiao, “Fusion similarity-based reranking for sar image retrieval,” *IEEE Geoscience and Remote Sensing Letters*, vol. 14, no. 2, pp. 242–246, 2017.

[60] A. Ansari, H. Danyali, and M. S. Helfroush, “Hs remote sensing image restoration using fusion with ms images by em algorithm,” *IET Signal Processing*, vol. 11, no. 1, pp. 95–103, 2017.

[61] Q. Wei, J. Bioucas-Dias, N. Dobigeon, J. Y. Tourneret, M. Chen, and S. Godsill, “Multiband image fusion based on spectral unmixing,” *IEEE Transactions on Geoscience and Remote Sensing*, vol. 54, no. 12, pp. 7236–7249, 2016.

[62] M. A. Qureshi, A. Beghdadi, and M. Deriche, “Towards the design of a consistent image contrast enhancement evaluation measure,” *Signal Processing: Image Communication*, vol. 58, pp. 212 – 227, 2017.

[63] M. Ju, Z. Gu, and D. Zhang, “Single image haze removal based on the improved atmospheric scattering model,” *Neurocomputing*, vol. 260, pp. 180 – 191, 2017.

[64] C. Qing, F. Yu, X. Xu, W. Huang, and J. Jin, “Underwater video dehazing based on spatial–temporal information fusion,” *Multidimensional Systems and Signal Processing*, vol. 27, no. 4, pp. 909–924, 2016.

[65] R. Kumar, B. K. Kaushik, and R. Balasubramanian, “Fpga implementation of image dehazing algorithm for real time applications,” in *Applications of Digital Image Processing XL*, vol. 10396, p. 1039633, International Society for Optics and Photonics, 2017.

[66] L. Zheng, H. Shi, and M. Gu, “Infrared traffic image enhancement algorithm based on dark channel prior and gamma correction,” *Modern Physics Letters B*, vol. 31, no. 19-21, p. 1740044, 2017.

[67] S.-C. Huang, B.-H. Chen, and Y.-J. Cheng, “An efficient visibility enhancement algorithm for road scenes captured by intelligent transportation systems,” *IEEE Transactions on Intelligent Transportation Systems*, vol. 15, no. 5, pp. 2321–2332, 2014.

[68] A. Conca, C. Ridella, and E. Sapori, “A risk assessment for road transportation of dangerous goods: a routing solution,” *Transportation Research Procedia*, vol. 14, pp. 2890–2899, 2016.

[69] K. Fang, G. Y. Ke, and M. Verma, "A routing and scheduling approach to rail transportation of hazardous materials with demand due dates," *European Journal of Operational Research*, vol. 261, no. 1, pp. 154–168, 2017.

[70] J. P. Kennedy and J. M. Wilson, "Liabilities and responsibilities: ocean transportation intermediaries (otis) and the distribution of counterfeit goods," *Maritime Economics & Logistics*, vol. 19, no. 1, pp. 182–187, 2017.

[71] A. Beck, J. Henneberger, S. Schöpfer, J. Fugal, and U. Lohmann, "Hologondel: in situ cloud observations on a cable car in the swiss alps using a holographic imager," *Atmospheric Measurement Techniques*, vol. 10, no. 2, pp. 459–476, 2017.

[72] A. S. A. Ghani and N. A. M. Isa, "Automatic system for improving underwater image contrast and color through recursive adaptive histogram modification," *Computers and Electronics in Agriculture*, vol. 141, pp. 181 – 195, 2017.

[73] U. A. Nnolim, "Improved partial differential equation-based enhancement for underwater images using local–global contrast operators and fuzzy homomorphic processes," *IET Image Processing*, vol. 11, no. 11, pp. 1059–1067, 2017.

[74] M. Amintoosi, M. Fathy, and N. Mozayani, "Video enhancement through image registration based on structural similarity," *The Imaging Science Journal*, vol. 59, no. 4, pp. 238–250, 2011.

[75] A. K. Tripathi and S. Mukhopadhyay, "Removal of fog from images: A review," *IETE Technical Review*, vol. 29, no. 2, pp. 148–156, 2012.

[76] A. Tripathi and S. Mukhopadhyay, "Single image fog removal using anisotropic diffusion," *IET Image processing*, vol. 6, no. 7, pp. 966–975, 2012.

[77] N. Hautiere, J.-P. Tarel, D. Aubert, and E. Dumont, "Blind contrast enhancement assessment by gradient ratioing at visible edges," *Image Analysis & Stereology*, vol. 27, no. 2, pp. 87–95, 2011.

[78] L. K. Choi, J. You, and A. C. Bovik, "Referenceless prediction of perceptual fog density and perceptual image defogging," *IEEE Transactions on Image Processing*, vol. 24, no. 11, pp. 3888–3901, 2015.

[79] N. Vuković and Z. Miljković, "A growing and pruning sequential learning algorithm of hyper basis function neural network for function approximation," *Neural Networks*, vol. 46, pp. 210–226, 2013.

[80] R. O. Duda, P. E. Hart, and D. G. Stork, *Pattern classification*. John Wiley & Sons, 2012.

[81] J. Xiao, L. Zhu, Y. Zhang, E. Liu, and J. Lei, “Scene-aware image dehazing based on sky-segmented dark channel prior,” *IET Image Processing*, vol. 11, no. 12, pp. 1163–1171, 2017.

[82] M. Zhu, B. He, and Q. Wu, “Single image dehazing based on dark channel prior and energy minimization,” *IEEE Signal Processing Letters*, vol. 25, no. 2, pp. 174–178, 2018.

[83] R. Wang, R. Li, and H. Sun, “Haze removal based on multiple scattering model with superpixel algorithm,” *Signal Processing*, vol. 127, pp. 24–36, 2016.

[84] H. Zhao, C. Xiao, J. Yu, and X. Xu, “Single image fog removal based on local extrema,” *IEEE/CAA Journal of Automatica Sinica*, vol. 2, no. 2, pp. 158–165, 2015.

[85] G. Ge, Z. Wei, and J. Zhao, “Fast single-image dehazing using linear transformation,” *Optik-International Journal for Light and Electron Optics*, vol. 126, no. 21, pp. 3245–3252, 2015.

[86] A. Kumari and S. K. Sahoo, “Fast single image and video deweathering using look-up-table approach,” *AEU-International Journal of Electronics and Communications*, vol. 69, no. 12, pp. 1773–1782, 2015.

[87] M. Ding and L. Wei, “Single-image haze removal using the mean vector l2-norm of rgb image sample window,” *Optik-International Journal for Light and Electron Optics*, vol. 126, no. 23, pp. 3522–3528, 2015.

[88] Z. Li, J. Zheng, Z. Zhu, W. Yao, and S. Wu, “Weighted guided image filtering.,” *IEEE Transactions on Image processing*, vol. 24, no. 1, pp. 120–129, 2015.

[89] J. Li, H. Zhang, D. Yuan, and M. Sun, “Single image dehazing using the change of detail prior,” *Neurocomputing*, vol. 156, pp. 1–11, 2015.

[90] Z. Li and J. Zheng, “Edge-preserving decomposition-based single image haze removal,” *IEEE Transactions on Image Processing*, vol. 24, no. 12, pp. 5432–5441, 2015.

[91] F. Guo, H. Peng, and J. Tang, “Genetic algorithm-based parameter selection approach to single image defogging,” *Information Processing Letters*, vol. 116, no. 10, pp. 595 – 602, 2016.

[92] Y. Liu, J. Shang, L. Pan, A. Wang, and M. Wang, “A unified variational model for single image dehazing,” *IEEE Access*, vol. 7, pp. 15722–15736, 2019.

[93] C. Hodges, M. Bennamoun, and H. Rahmani, “Single image dehazing using deep neural networks,” *Pattern Recognition Letters*, vol. 128, pp. 70 – 77, 2019.

[94] M. Ju, C. Ding, Y. J. Guo, and D. Zhang, "Idgcp: Image dehazing based on gamma correction prior," *IEEE Transactions on Image Processing*, vol. 29, pp. 3104–3118, 2020.

[95] H. Zhu, Y. Cheng, X. Peng, J. T. Zhou, Z. Kang, S. Lu, Z. Fang, L. Li, and J. Lim, "Single-image dehazing via compositional adversarial network," *IEEE Transactions on Cybernetics*, pp. 1–10, 2019.

[96] W. Ren, J. Pan, H. Zhang, X. Cao, and M.-H. Yang, "Single image dehazing via multi-scale convolutional neural networks with holistic edges," *International Journal of Computer Vision*, pp. 1–20, 2019.

[97] S. Serikawa and H. Lu, "Underwater image dehazing using joint trilateral filter," *Computers & Electrical Engineering*, vol. 40, no. 1, pp. 41–50, 2014.

[98] X. Pan, F. Xie, Z. Jiang, and J. Yin, "Haze removal for a single remote sensing image based on deformed haze imaging model," *IEEE Signal Processing Letters*, vol. 22, no. 10, pp. 1806–1810, 2015.

[99] F.-C. Cheng, C.-C. Cheng, P.-H. Lin, and S.-C. Huang, "A hierarchical airlight estimation method for image fog removal," *Engineering Applications of Artificial Intelligence*, vol. 43, pp. 27–34, 2015.

[100] J. M. Guo, J. y. Syue, V. R. Radzicki, and H. Lee, "An efficient fusion-based defogging," *IEEE Transactions on Image Processing*, vol. 26, no. 9, pp. 4217–4228, 2017.

[101] Y. Jiang, C. Sun, Y. Zhao, and L. Yang, "Fog density estimation and image defogging based on surrogate modeling for optical depth," *IEEE Transactions on Image Processing*, vol. 26, no. 7, pp. 3397–3409, 2017.

[102] D. Singh and V. Kumar, "Dehazing of outdoor images using notch based integral guided filter," *Multimedia Tools and Applications*, vol. 77, no. 20, pp. 27363–27386, 2018.

[103] A. Alajarmeh and A. Zaidan, "A real-time framework for video dehazing using bounded transmission and controlled gaussian filter," *Multimedia Tools and Applications*, vol. 77, no. 20, pp. 26315–26350, 2018.

[104] A. Alajarmeh, R. Salam, K. Abdulrahim, M. Marhusin, A. Zaidan, and B. Zaidan, "Real-time framework for image dehazing based on linear transmission and constant-time airlight estimation," *Information Sciences*, vol. 436-437, pp. 108 – 130, 2018.

[105] S. Emberton, L. Chittka, and A. Cavallaro, "Underwater image and video dehazing with pure haze region segmentation," *Computer Vision and Image Understanding*, vol. 168, pp. 145 – 156, 2018. Special Issue on Vision and Computational Photography and Graphics.

[106] J. Zhang, X. Wang, C. Yang, J. Zhang, D. He, and H. Song, "Image dehazing based on dark channel prior and brightness enhancement for agricultural remote sensing images from consumer-grade cameras," *Computers and Electronics in Agriculture*, vol. 151, pp. 196 – 206, 2018.

[107] Y. Gao, Q. Li, and J. Li, "Single image dehazing via a dual-fusion method," *Image and Vision Computing*, vol. 94, p. 103868, 2020.

[108] F. Guo, X. Zhao, J. Tang, H. Peng, L. Liu, and B. Zou, "Single image dehazing based on fusion strategy," *Neurocomputing*, 2019.

[109] Q. Shu, C. Wu, Q. Zhong, and R. W. Liu, "Alternating minimization algorithm for hybrid regularized variational image dehazing," *Optik*, vol. 185, pp. 943 – 956, 2019.

[110] Y. Wu, Y. Qin, Z. Wang, X. Ma, and Z. Cao, "Densely pyramidal residual network for uav-based railway images dehazing," *Neurocomputing*, vol. 371, pp. 124 – 136, 2020.

[111] J.-P. Tarel, N. Hautiere, A. Cord, D. Gruyer, and H. Halmaoui, "Improved visibility of road scene images under heterogeneous fog," in *Intelligent Vehicles Symposium (IV), 2010 IEEE*, pp. 478–485, Citeseer, 2010.

[112] B. Li, W. Ren, D. Fu, D. Tao, D. Feng, W. Zeng, and Z. Wang, "Reside: A benchmark for single image dehazing," *arXiv preprint arXiv:1712.04143*, 2017.

[113] W. L. Kede Ma and Z. Wang, "Perceptual evaluation of single image dehazing algorithms," in *in: Image Processing, Proc. IEEE*, pp. 3600–3604, Citeseer, 2015.

[114] C. D. V. Cosmin Ancuti, Codruta O. Ancuti, "D-hazy: A dataset to evaluate quantitatively dehazing algorithms," in *IEEE International Conference on Image Processing (ICIP)*, ICIP'16, pp. 2226–2230, 2016.

[115] J.-P. Tarel, N. Hautiere, L. Caraffa, A. Cord, H. Halmaoui, and D. Gruyer, "Vision enhancement in homogeneous and heterogeneous fog," *IEEE Intelligent Transportation Systems Magazine*, vol. 4, no. 2, pp. 6–20, 2012.

[116] X. Fan, Y. Wang, X. Tang, R. Gao, and Z. Luo, "Two-layer gaussian process regression with example selection for image dehazing," *IEEE Transactions on Circuits and Systems for Video Technology*, vol. PP, no. 99, pp. 1–1, 2016.

[117] W. Zhang and X. Hou, "Light source point cluster selection-based atmospheric light estimation," *Multimedia Tools and Applications*, pp. 1–12, 2017.

[118] J. El Khoury, S. Le Moan, J.-B. Thomas, and A. Mansouri, "Color and sharpness assessment of single image dehazing," *Multimedia Tools and Applications*, pp. 1–22, 2017.

[119] B. Jiang, H. Meng, J. Zhao, X. Ma, S. Jiang, L. Wang, Y. Zhou, Y. Ru, and C. Ru, "Single image fog and haze removal based on self-adaptive guided image filter and color channel information of sky region," *Multimedia Tools and Applications*, pp. 1–18, 2017.

[120] T. Soumya and S. M. Thampi, "Recolorizing dark regions to enhance night surveillance video," *Multimedia Tools and Applications*, pp. 1–17, 2016.

[121] R. Xiang and F. Wu, "Single image haze removal with approximate radiance darkness prior," *Modern Physics Letters B*, p. 1840086, 2018.

[122] X. Lian, Y. Pang, and A. Yang, "Learning intensity and detail mapping parameters for dehazing," *Multimedia Tools and Applications*, pp. 1–26, 2017.

[123] W. Wang, X. Yuan, X. Wu, and Y. Liu, "Fast image dehazing method based on linear transformation," *IEEE Transactions on Multimedia*, vol. PP, no. 99, pp. 1–1, 2017.

[124] QUICKBIRD, "Global land cover facility," *http://glcf.umd.edu/*, Dec 2016.

[125] J. Bala and K. Lakhwani, "Performance evaluation of various desmogging techniques for single smoggy images," *Modern Physics Letters B*, vol. 33, no. 05, p. 1950056, 2019.

[126] R. Xiang and F. Wu, "Single image haze removal with approximate radiance darkness prior," *Modern Physics Letters B*, vol. 32, no. 34n36, p. 1840086, 2018.

[127] H. Singh and B. S. Khehra, "Visibility enhancement of color images using type-ii fuzzy membership function," *Modern Physics Letters B*, vol. 32, no. 11, p. 1850130, 2018.

[128] Q. Chen and Y. Wang, "A blind image deblurring algorithm based on relative gradient and sparse representation," *Modern Physics Letters B*, vol. 32, no. 34n36, p. 1840087, 2018.

[129] S. Khare and P. Kaushik, "Gradient nuclear norm minimization-based image filter," *Modern Physics Letters B*, p. 1950214, 2019.

[130] D. Singh and V. Kumar, "Single image haze removal using integrated dark and bright channel prior," *Modern Physics Letters B*, p. 1850051, 2018.

[131] G. Papari, N. Idowu, and T. Varslot, "Fast bilateral filtering for denoising large 3d images," *IEEE Transactions on Image Processing*, vol. 26, no. 1, pp. 251–261, 2016.

[132] S. He, Q. Yang, R. W. Lau, and M.-H. Yang, "Fast weighted histograms for bilateral filtering and nearest neighbor searching," *IEEE Transactions on Circuits and Systems for Video Technology*, vol. 26, no. 5, pp. 891–902, 2016.

[133] K. N. Chaudhury, D. Sage, and M. Unser, "Fast bilateral filtering using trigonometric range kernels," *IEEE Transactions on Image Processing*, vol. 20, no. 12, pp. 3376–3382, 2011.

[134] Y. Pathak, K. Arya, and S. Tiwari, "Low-dose ct image reconstruction using gain intervention-based dictionary learning," *Modern Physics Letters B*, vol. 32, no. 14, p. 1850148, 2018.

[135] R. Ma and S. Zhang, "An improved color image defogging algorithm using dark channel model and enhancing saturation," *Optik*, vol. 180, pp. 997–1000, 2019.

[136] D. Singh and V. Kumar, "A novel dehazing model for remote sensing images," *Computers & Electrical Engineering*, vol. 69, pp. 14–27, 2018.

[137] K. Chang, X. Zhang, P. L. K. Ding, and B. Li, "Data-adaptive low-rank modeling and external gradient prior for single image super-resolution," *Signal Processing*, vol. 161, pp. 36–49, 2019.

[138] V. P. Singh, R. Srivastava, Y. Pathak, S. Tiwari, and K. Kaur, "Content-based image retrieval based on supervised learning and statistical-based moments," *Modern Physics Letters B*, p. 1950213, 2019.

[139] X. Zhu, R. Xiang, F. Wu, and X. Jiang, "Single image haze removal based on fusion darkness channel prior," *Modern Physics Letters B*, vol. 31, no. 19-21, p. 1740037, 2017.

[140] C. Jiang and X. He, "An improved polsar image speckle reduction algorithm based on lmmse and rica," *Modern Physics Letters B*, vol. 31, no. 19-21, p. 1740033, 2017.

[141] D. Singh and V. Kumar, "A comprehensive review of computational dehazing techniques," *Archives of Computational Methods in Engineering*, pp. 1–19, 2018.

[142] X. Liu, H. Zhang, Y. Y. Tang, and J. X. Du, "Scene-adaptive single image dehazing via opening dark channel model," *IET Image Processing*, vol. 10, no. 11, pp. 877–884, 2016.

[143] I. Riaz, X. Fan, and H. Shin, "Single image dehazing with bright object handling," *IET Computer Vision*, vol. 10, no. 8, pp. 817–827, 2016.

[144] S. G. Narasimhan and S. K. Nayar, "Contrast restoration of weather degraded images," *IEEE transactions on pattern analysis and machine intelligence*, vol. 25, no. 6, pp. 713–724, 2003.

[145] S. K. Nayar and S. G. Narasimhan, "Vision in bad weather," in *Computer Vision, 1999. The Proceedings of the Seventh IEEE International Conference on*, vol. 2, pp. 820–827, IEEE, 1999.

[146] B. Li, S. Wang, J. Zheng, and L. Zheng, "Single image haze removal using content-adaptive dark channel and post enhancement," *IET Computer Vision*, vol. 8, no. 2, pp. 131–140, 2014.

[147] D. Wang and J. Zhu, "Fast smoothing technique with edge preservation for single image dehazing," *IET Computer Vision*, vol. 9, no. 6, pp. 950–959, 2015.

[148] J.-M. Guo, J.-Y. Syue, V. Radzicki, and H. Lee, "An efficient fusion-based defogging," *IEEE Transactions on Image Processing*, 2017.

[149] S. M. Yoon, "Visibility enhancement of fog-degraded image using adaptive total variation minimisation," *The Imaging Science Journal*, vol. 64, no. 2, pp. 82–86, 2016.

[150] K. Nishino, L. Kratz, and S. Lombardi, "Bayesian defogging," *International journal of computer vision*, vol. 98, no. 3, pp. 263–278, 2012.

[151] D. Singh and V. Kumar, "Image dehazing using moore neighborhood-based gradient profile prior," *Signal Processing: Image Communication*, vol. 70, pp. 131–144, 2019.

[152] H. Lu, Q. Liu, M. Zhang, Y. Wang, and X. Deng, "Gradient-based low rank method and its application in image inpainting," *Multimedia Tools and Applications*, vol. 77, no. 5, pp. 5969–5993, 2018.

[153] K. Deb, A. Pratap, S. Agarwal, and T. Meyarivan, "A fast and elitist multiobjective genetic algorithm: Nsga-ii," *IEEE transactions on evolutionary computation*, vol. 6, no. 2, pp. 182–197, 2002.

Appendix-A

The designed NSGA based desmogging model is compared to the well-known existing techniques while considering various performance measures like percentage of saturated pixels (S_p), smog gradient, contrast gain (CG), visible edges, execution time (ET), structural similarity index metric, and peak signal to noise ratio . This section describes the results produced by NSGA based desmogging technique (discussed in chapter 5 of the thesis) through the graphs.

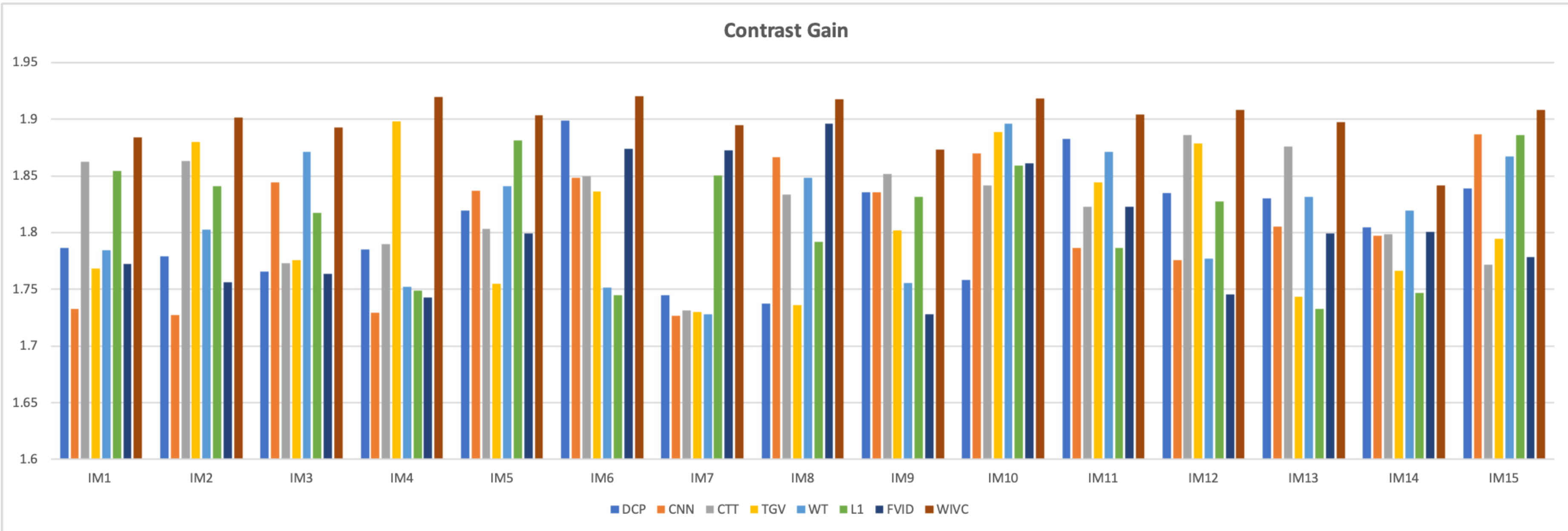

Figure 6.1: Contrast analyses of Proposed WIVC model and the competitive desmogging techniques

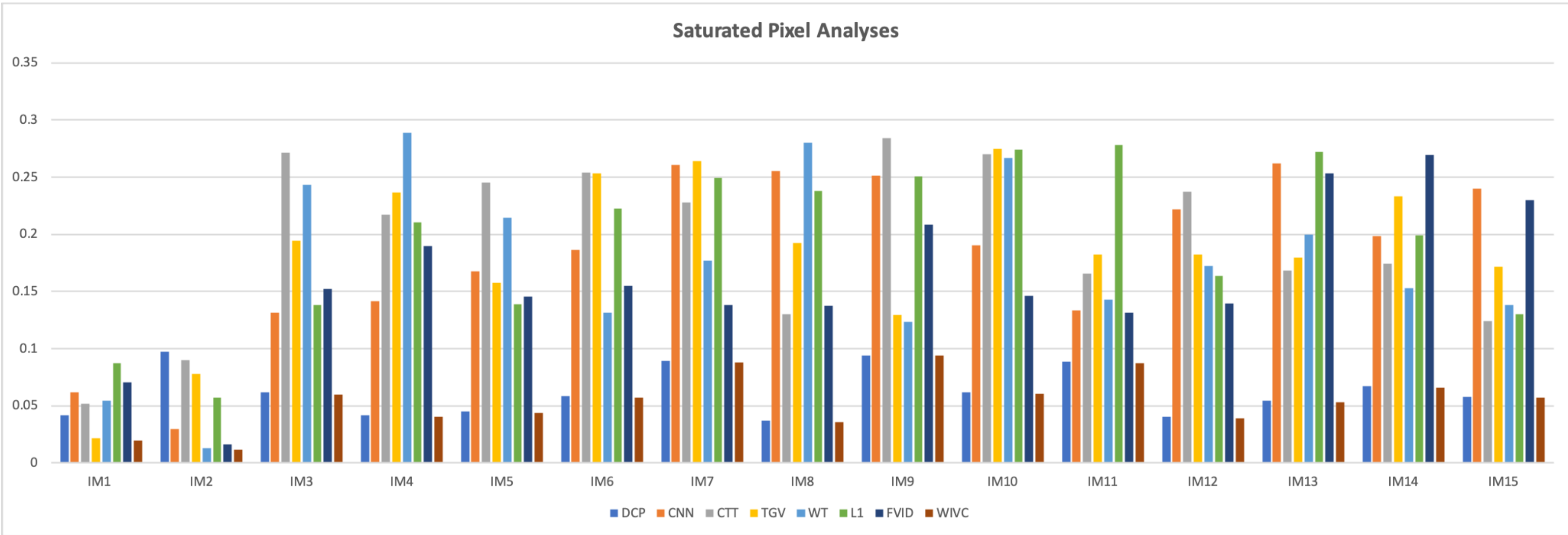

Figure 6.2: Saturated Pixel analyses of Proposed WIVC model and the competitive desmogging techniques

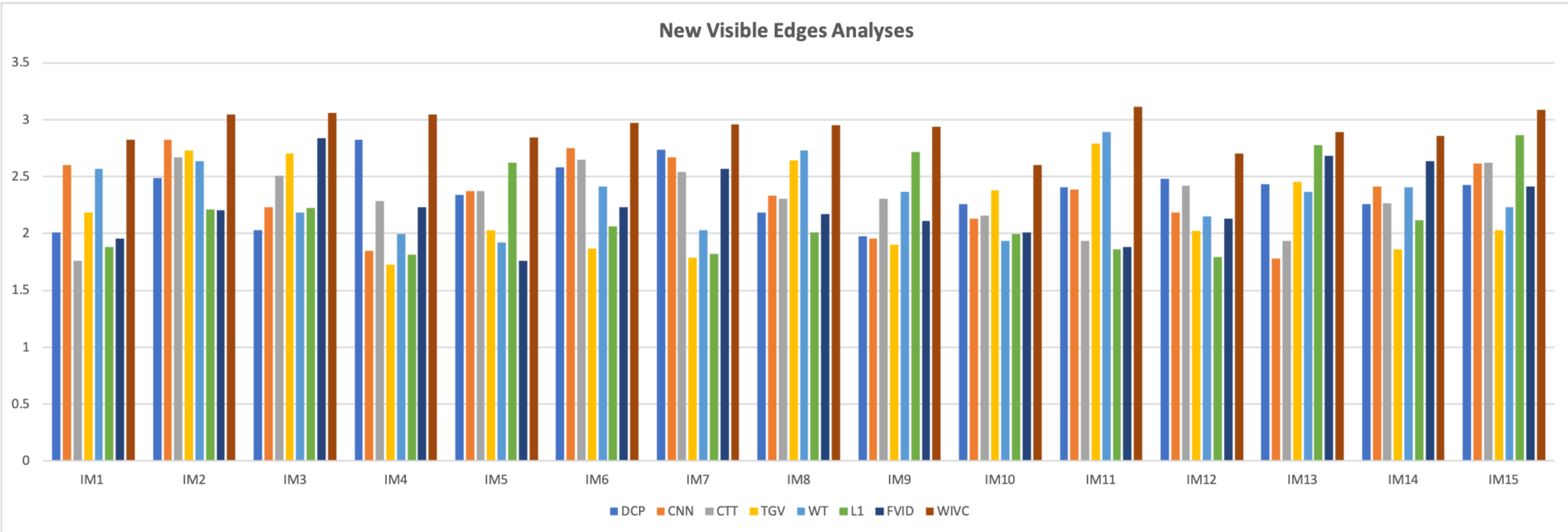

Figure 6.3: New Visible edges analyses of Proposed WIVC model and the competitive desmogging techniques

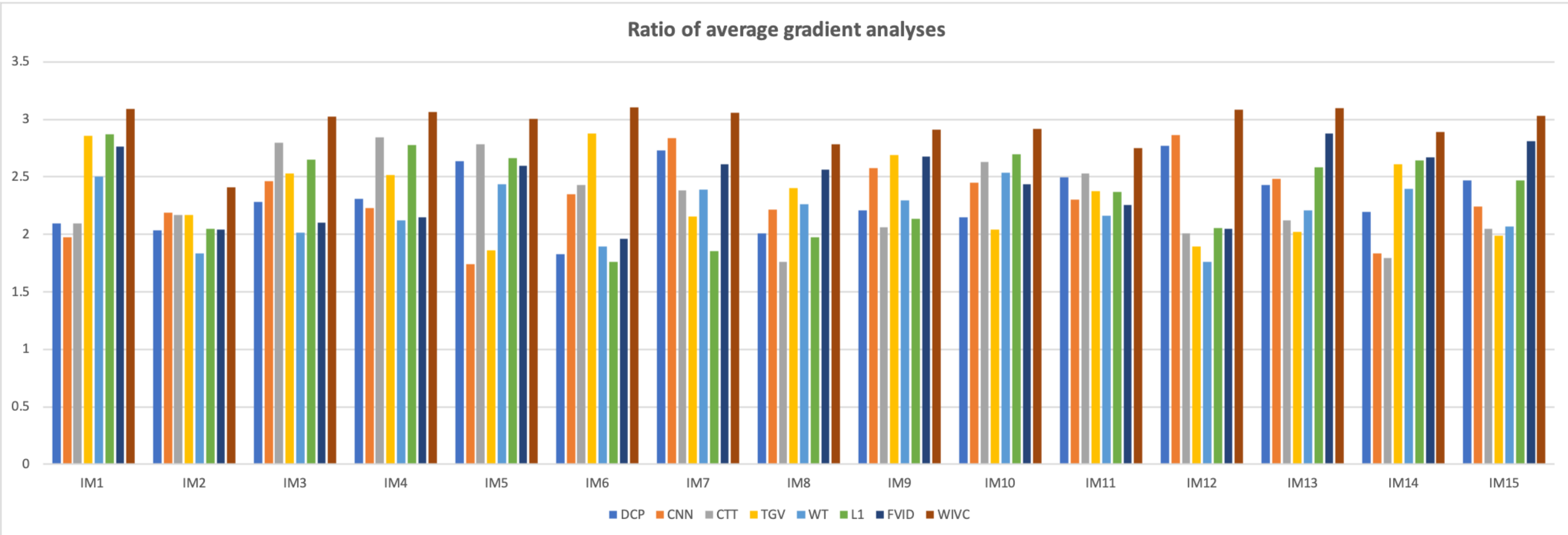

Figure 6.4: Average gradient analyses of Proposed WIVC model and the competitive desmogging techniques

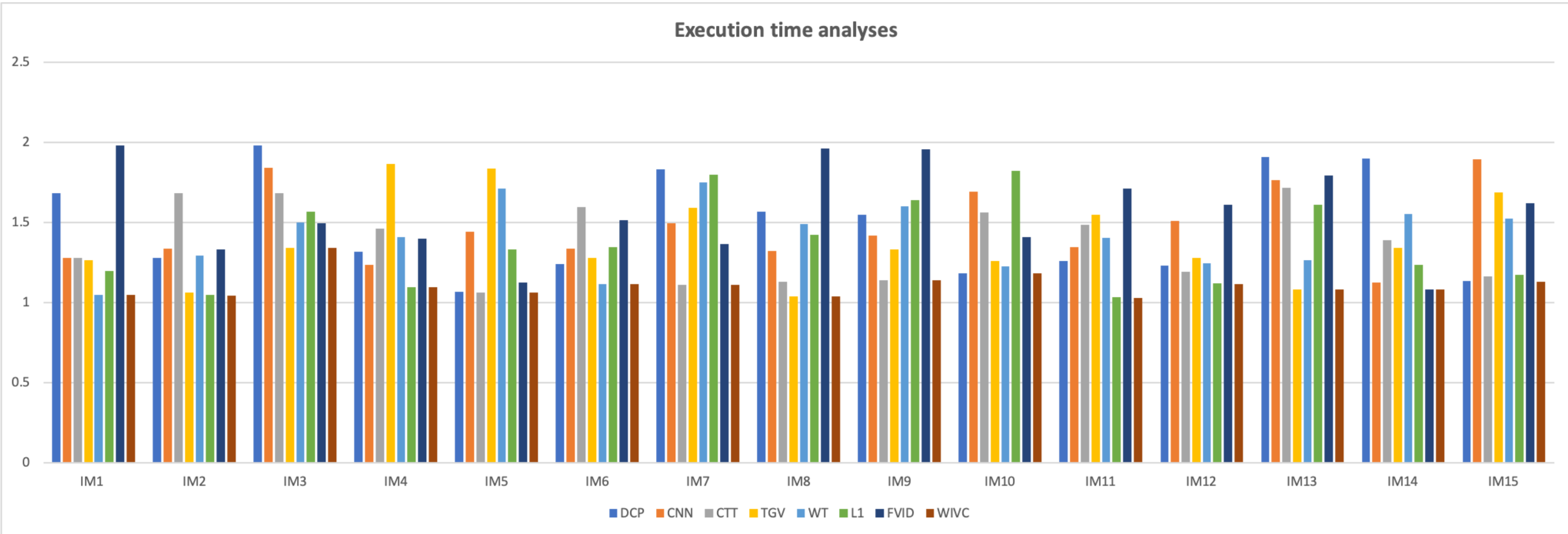

Figure 6.5: Execution Time analyses of Proposed WIVC model and the competitive desmogging techniques

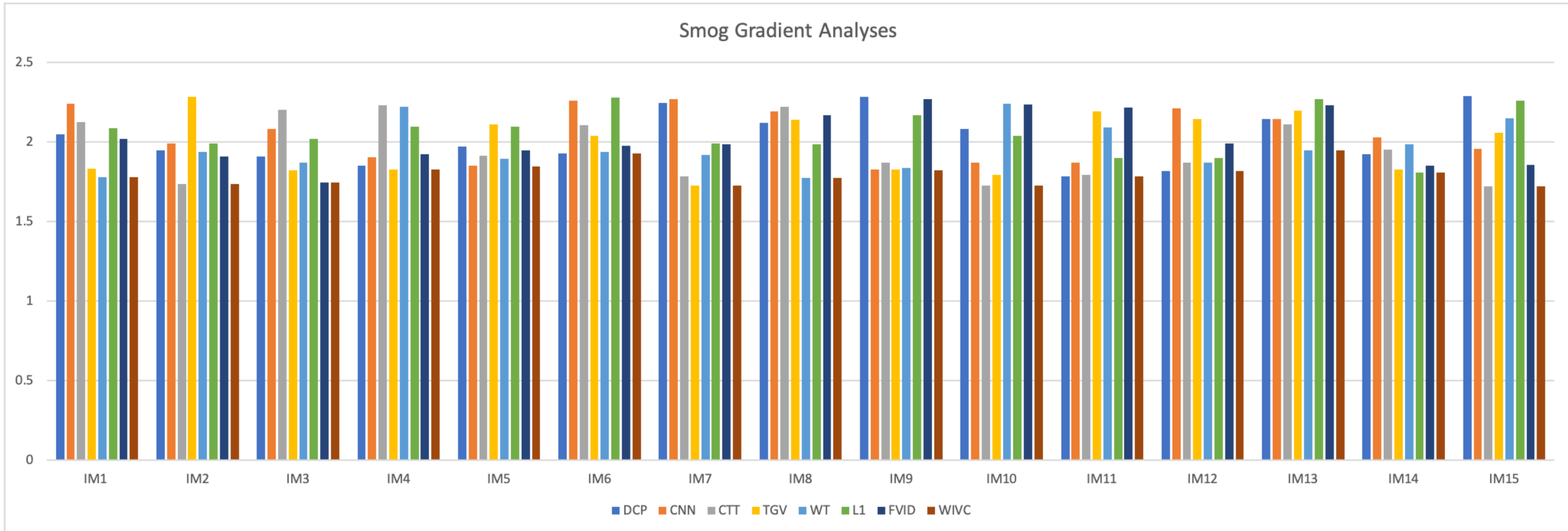

Figure 6.6: Smog gradient analyses of Proposed WIVC model and the competitive desmogging techniques

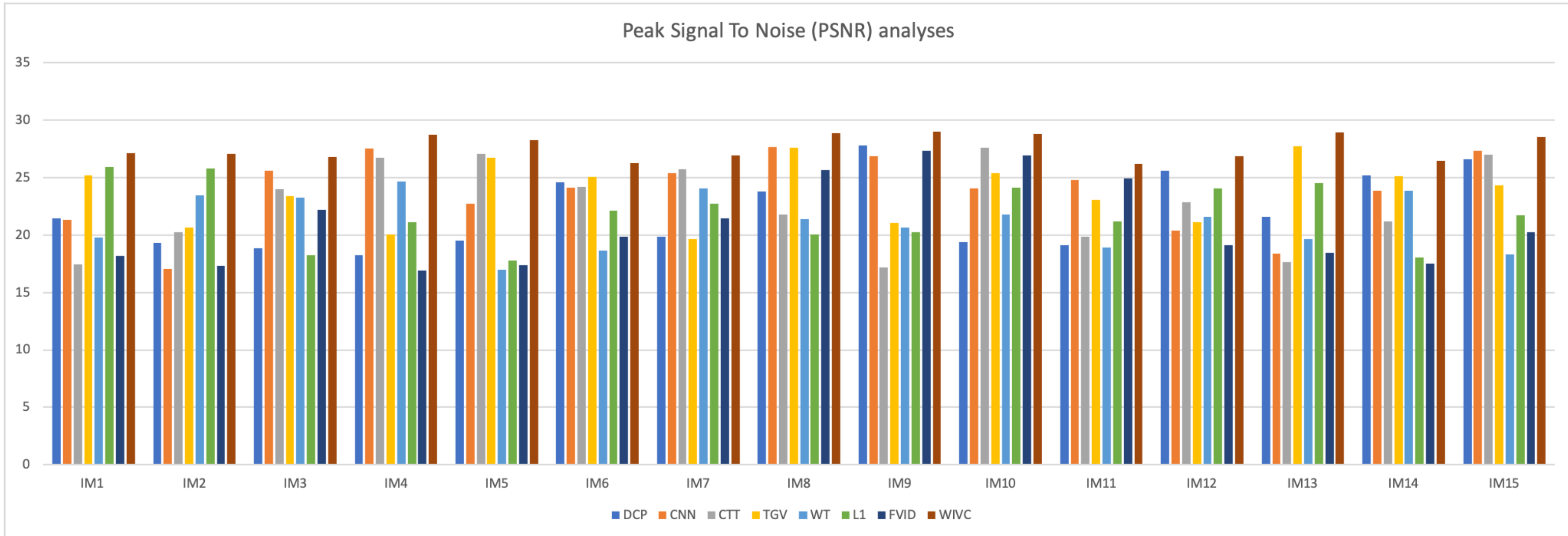

Figure 6.7: Peak Signal To Noise Ratio (PSNR) analyses of Proposed WIVC model and the competitive desmogging techniques

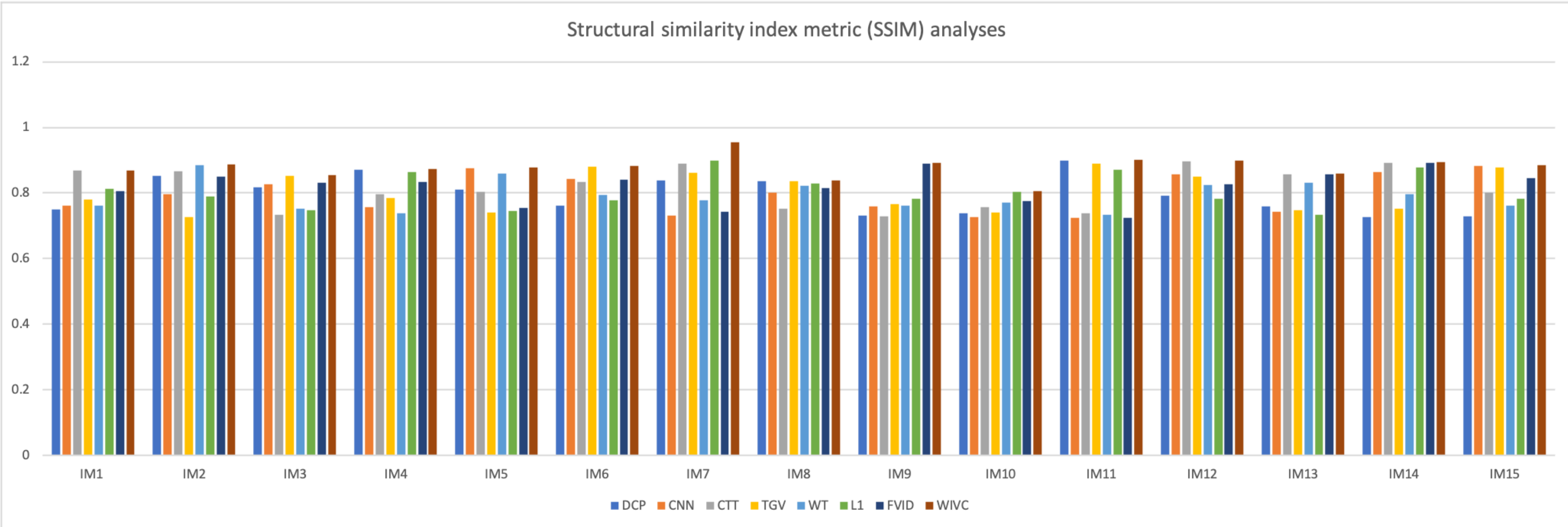

Figure 6.8: Structural Similarity Index Metric (SSIM) analyses of Proposed WIVC model and the competitive desmogging techniques